Development of DEM models for analysis of multi-type single lap joints: a microscale approach

Submitted by:

Kai Pang

This dissertation is submitted for the degree of Doctor of Philosophy

2025

Lancaster University

School of Engineering

Abstract

Currently, the concept of lightweighting is a prominent area of research to decrease the energy consumption and emissions. One of the most effective strategies for achieving lightweighting is to utilize advanced lightweight materials in place of traditional materials. Meanwhile, there are no fabrication processes capable of producing the entire structure as a monolithic unit without joints. The majority of structures are constructed by assembling different types of structural elements. Some traditional joining methods, such as bolting and riveting, can introduce high stress concentrations around the joint area and may cause cracks during the drilling process. In contrast, adhesive bonding offers notable advantages for joining multi-material structures, including reduced life-cycle maintenance costs and weight, more uniform stress distribution, and enhanced design flexibility.

Microstructures such as microstructural surface roughness and internal defects of constituents are crucial factors in determining the performance and fracture mechanism of adhesive joints. However, the research dedicated to the examination of the failure mechanisms for adhesive joints influenced by microstructures at microscale is limited. This work conducts systematic experimental and numerical investigations into the effect of microstructural roughness and defects on the performance and fracture mechanism of multi-type adhesive SLJs. The adherend materials used in this study are Al and PPA, bonded with an epoxy adhesive (Loctite EA 9497).

Firstly, the mechanical properties of the Al adherend, PPA adherend, epoxy adhesive, and multi-type SLJs (Al-Al SLJ, PPA-PPA SLJ, and hybrid SLJ) with three roughness grades are obtained through experimental studies. The mechanical properties of adherends and adhesive are used to determine the microparameters of the contact model of adherends and adhesive particles in the DEM model. The calibrated

microparameters are validated by several experimental data, especially the interlaminar-like properties of the thin adhesive layer in joints. Then, the microstructural roughness and microstructural defect in SLJs are experimentally investigated through SEM and microCT scanning. The measured microstructural roughness and microstructural defect are realistically introduced into the DEM models for further calibration, including DEM Al-Al SLJ models, PPA-PPA SLJ models, and hybrid SLJ models. Compared to the experimental results, the developed DEM SLJ models can predict the performance and capture the microstructural fracture mechanisms of multi-type SLJs. Finally, the effects of microstructural roughness and microstructural defects on the performance of multi-type SLJs are investigated, including the failure load and stiffness. The effects of microstructural roughness and microstructural defects on the microscale fracture mechanisms of multi-type SLJs are also explored and discussed, including the crack initiation, coalescence, and propagation within the adhesive and interface.

Keywords: Adhesive; Single lap joint; Discrete element method; Performance; Fracture mechanism; Microstructure; Surface roughness; Defect.

Declaration

I declare that this thesis is my own original work and has not been submitted, in whole or in part, for the award of a degree or other qualification at this or any other university. It is the result of my work, except where explicitly stated otherwise. Many of the ideas presented in this thesis were developed through discussions with my supervisors, Dr. Xiaonan Hou and Prof. Jianqiao Ye.

Kai Pang

May, 2025

Acknowledgements

I would like to express my sincere gratitude to my supervisors, Dr. Xiaonan Hou and Prof. Jianqiao Ye, for their invaluable guidance, continuous support, and encouragement throughout my PhD studies.

I am also grateful to Dr. Xinger Wang and Dr. Zewen Gu, whose insightful feedback and suggestions greatly improve the quality of my work.

Special thanks go to my colleagues and friends for their support and stimulating discussions during the research process.

Finally, I would like to thank my parents, Caiying Hong and Bingxue Pang, for their patience, understanding, and unwavering support throughout the course of my studies.

Publications

- Pang, K., Wang, X. E., Ye, J., Carnegie, C., & Hou, X. (2024). Effect of microstructural roughness on the performance and fracture mechanism of multi-type single lap joints. *Composites Part B: Engineering*, *286*, 111763.
- Pang, K., Gu, Z., Ye, J., & Hou, X. (2025). Analysis of the effect of microstructural defects on the performance and fracture mechanism of adhesive single lap joints. *Composites Science and Technology*, *266*, 111166.
- Wang, X. E., Pang, K., Huang, X., Yang, J., Ye, J., & Hou, X. (2023). Insights into the micromechanical response of adhesive joint with stochastic surface micro-roughness. Engineering Fracture Mechanics, 277, 108954.
- Ge, Z., Hu, Q., Pang, K., Zhu, Y., & Hou, X. (2025). Significantly improves the mechanical strength of aluminum alloy adhesive joint through electrochemical pretreatment in environmentally friendly medium. *Journal of Manufacturing Processes*, *133*, 592-606.
- Wang, X. E., Kanani, A. Y., Pang, K., Yang, J., Ye, J., & Hou, X. (2022). A novel genetic expression programming assisted calibration strategy for discrete element models of composite joints with ductile adhesives. *Thin-Walled Structures*, *180*, 109985.
- Wang, Y., Wang, X. E., Yang, J., Xie, D., Pang, K., & Pan, Z. (2024). Experimental investigation into the expansion behaviour of thermally tempered laminated glass plates at asymmetric fracture. *Construction and Building Materials*, *442*, 137586.

List of Tables

List of Figures

`

Contents

Chapter 1

1 Introduction

1.1 Background

The majority of greenhouse gas emissions from industrial activities are directly tied to energy consumption. Improving energy efficiency offers a pathway to significantly reduce energy demand, lower associated emissions, and decrease energy costs. As a result, prioritizing energy efficiency should be the initial strategy for manufacturers aiming to decarbonize their operations [1]. Transportation sources currently account for approximately 15% of global greenhouse gas emissions, though in many regions, it represents a more significant share of emissions [2]. The newly enacted EU legislation establishes a roadmap to achieve zero CO2 emissions for new passenger cars and light commercial vehicles by 2035. As part of this transition, intermediate targets have been set for 2030, aiming for a 55% reduction in emissions for cars and a 50% reduction for vans [3]. The International Civil Aviation Organization aims to achieve a 50% reduction in aviation emissions by 2050 [4]. The International Maritime Organization has established targets to reduce greenhouse gas emissions from ships by at least 20% by 2030 and at least 70% by 2040, compared to 2008 levels [5].

Currently, the concept of lightweighting is a prominent area of research to decrease the energy consumption and emissions. One of the most effective strategies for achieving lightweighting is to utilize advanced lightweight materials (e.g., aluminium, magnesium, or composites) in place of traditional materials (e.g., steel, iron) [6]. Meanwhile, there are no fabrication processes capable of producing the entire structure as a monolithic unit without joints. The majority of structures are constructed

by assembling different types of structural elements [7]. In practice, these necessarily result in the use and fabrication of multi-material structures for which proper joining techniques are critical for the high performance of the overall structures in numerous industrial sectors, including the automobile, aeronautical, and naval industries [8].

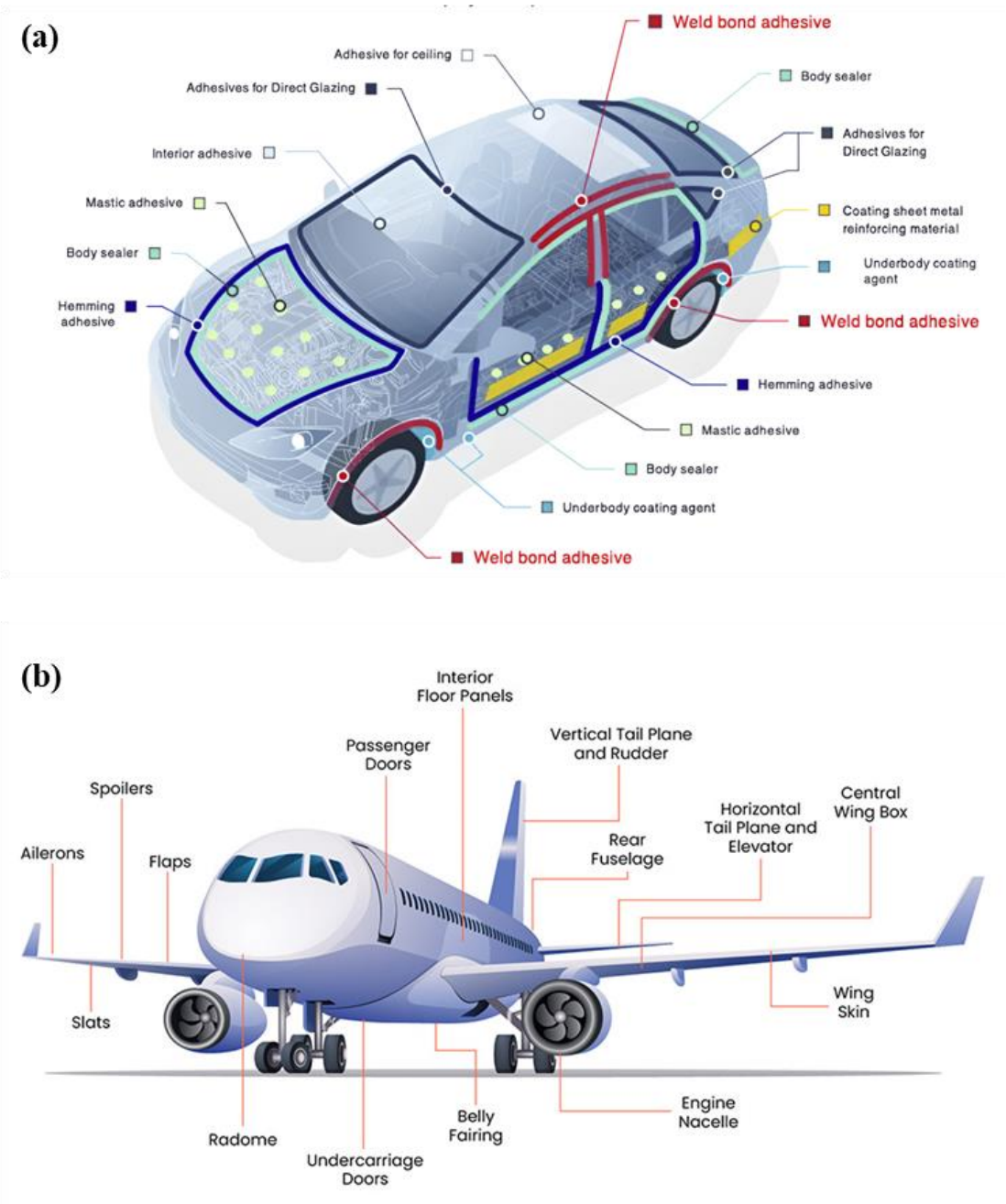

Figure 1-1 Some of the bonding areas in (a) A vehicle [9]. (b) An airplane [10].

Some traditional joining techniques, such as bolting and riveting, can induce high stress concentrations around the joining point and cracks during the drilling process [11, 12]. In contrast, adhesive joining provides significant advantages for bonding multi-material structures, including reduced life-cycle maintenance costs and weight, more uniform stress distribution, and increased design flexibility [13, 14]. The global automotive adhesives market is projected to reach an estimated USD 23.9 billion by 2030, with a compound annual growth rate of 11.4% from 2024 to 2030 [15]. Similarly, the global aerospace adhesives market, valued at around USD 881 million in 2022, is expected to grow at a compound annual growth rate of approximately 5%, reaching USD 1.73 billion by 2035 [16]. Some of the bonding areas using adhesives and sealants in the vehicle and aircraft are presented in Figure 1-1.

1.2 Aim and objective

Over the past decades, although significant progress has been made in adhesive-based multi-material joining, several barriers continue to limit the practical implementation of this technique. This is due to the lack of a well-received agreement for summarizing the influencing mechanisms of the factors affecting the performance and fracture mechanisms of the adhesive joints bonded by composite materials, especially at microscale. Furthermore, variations in joint configurations, particularly those with the dissimilar adherends, can induce erratic stress distributions and failure modes. There is also no widely accepted theory to accurately describe their failure mechanisms at microscale.

Understanding the effect of the factors on the performance and fracture mechanisms of adhesive joints can enable the industry to design and fabricate more reliable adhesive joints, thereby improving the product performance and quality. In light

of this, this study aims to experimentally and numerically investigate the effect of the microstructural features of adhesive joints on their performances and fracture mechanisms. To achieve this aim, the main objectives of this project are as follows:

- To experimentally investigate the mechanical properties of the adherends, adhesive, and multi-type single lap joints (SLJ), as well as the microstructural features including surface roughness of adherends and internal defects within SLJs at microscale.
- To calibrate the microparameters of the Discrete Element Method (DEM) models for the adherends, adhesive, and SLJs based on the experimental results.
- To develop the DEM models by realistically incorporating different roughness grades, which can describe the performance and capture the microscale fracture mechanisms of multi-type SLJs. Based on the developed models, the influence of microstructural roughness on the performance and fracture behavior of multi-type SLJs will be analysed and summarised.
- To develop the DEM models by realistically incorporating different types and densities of microstructural defects, which can describe the performance and capture the microscale fracture mechanisms of multi-type SLJs. Based on the developed models, the influence of microstructural defects on the performance and fracture behavior of multi-type SLJs will be analysed and summarised.

1.3 Thesis outline

Chapter 1 presents the background of the study on adhesive joints and outlines the challenges and limitations of current research. This chapter also defines the objectives and methodologies proposed to address these issues.

Chapter 2 provides a comprehensive review of existing literature on the characterisation of adhesive joints, the factors influencing their performance, and various methods used for their analysis. This chapter also highlights a significant research gap concerning the effect of microstructural features on the performance and fracture mechanisms of adhesive joints.

Chapter 3 outlines the experimental procedures used to determine the mechanical properties of the adherends, adhesive, and multi-type SLJs with different surface roughness grades, in accordance with relevant standards. In addition, the microstructural surface roughness and internal defects within the SLJs are also investigated experimentally.

Chapter 4 details the numerical procedures used for calibrating the microparameters of the contact models for the adherends and adhesive materials using DEM. The calibrated models are validated by experimental results, such as double cantilever beam (DCB), end notched flexure (ENF), and SLJ tests.

Chapter 5 presents a systematic numerical investigation into the performances and microscale fracture mechanisms of multi-type SLJs affected by different surface roughness grades, with a microscale focusing on analyzing the characteristics and properties of the adhesion interfaces resulting from the different adherend materials and surface profiles.

Chapter 6 explores the effects of microstructural defects within multi-type SLJs with different interfacial adhesion. Specifically, this chapter examines how different densities and types of microstructural defects affect the joint performance, crack initiation, coalescence, and propagation at the microscale.

Chapter 7 presents the conclusions and recommendations for future work. It summarises the key novel contributions of the works presented in the thesis. An overall

discussion of the experimental and numerical findings is provided, highlighting the efficiency and accuracy of the developed DEM model in predicting the performance and fracture mechanisms of multi-type SLJs. This chapter also summarises the influencing mechanisms of microstructural surface roughness of adherends and internal defects of the joints on the performances and fracture mechanisms of multi-type SLJs at microscale. Finally, this chapter concludes with an overall reflection on the thesis and outlines potential directions for future works.

Chapter 2

2 Literature review

2.1 Introduction

Over the years, manufacturers have focused on reducing weight to create lighter and more damage-tolerant structures. The growing use of lightweight and dissimilar materials (such as metal and composite combinations) in structural components has drawn increased attention in this field. Adhesive joining provides significant advantages for bonding composite structures, including reduced life-cycle maintenance costs and weight, more uniform stress distribution, and increased design flexibility. Despite these advantages, challenges remain in the application of adhesive joining techniques, due to the lack of an accepted theory that accurately describes the failure mechanisms of adhesive joints bonded by composite/dissimilar materials and that summarizes the factors influencing the joint performance, especially at microscale.

This chapter begins by reviewing the existing literature on the characterization of adhesive joints, covering aspects, such as joint configurations, hybrid joining, and failure mode. Then, the factors influencing the performance and fracture mechanisms of adhesive joints are investigated, including joint geometry, material properties, interface, and environmental conditions. Finally, the chapter examines the analysis methods for adhesive joints, focusing on both analytical approaches and numerical techniques, such as Finite Element Method (FEM) and DEM.

2.2 Characterisation of adhesive joints

2.2.1. Conventional configurations

Nowadays, various configurations of adhesive bonded joints have been developed. Figure 2-1 provides an overview of several conventional joint configurations. These joint configurations can be broadly categorized into two groups: disturbed and undisturbed shapes. In this study, disturbed topologies, illustrated in Figure 2-1a to Figure 2-1d, refer to joint designs where one or more offsets exist between the adherends. In contrast, undisturbed topologies, shown in Figure 2-1e to Figure 2-1h, are characterized by fully aligned adherends without offsets.

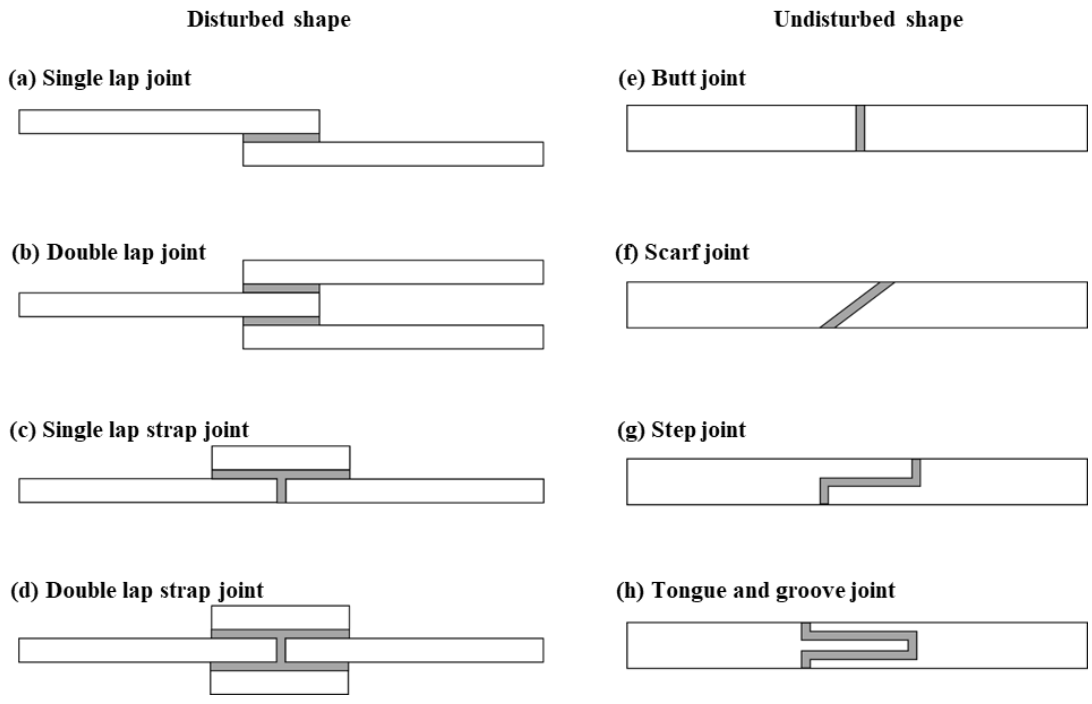

Figure 2-1. Basic joint configurations.

The SLJ (Figure 2-1a) is the most commonly used joint configuration and widely studied due to its simplicity in design, ease of manufacturing, and low cost [17]. Under tensile loading, the bonding overlap of the SLJ experiences shear stress. Additionally, due to the secondary bending moment caused by the offset between the

adherends in the SLJ, the bonding area also experiences high peel stress at the ends of the overlap [18, 19]. In a symmetric double lap adhesive joint (DLJ) (Figure 2-1b), this design provides a more balanced structure, reducing compliance and minimizing bending moments under tensile loading [20]. The central adherend is unaffected by bending moments, while the outer adherends experience them, leading to peel and compressive stress at the two ends of the overlap [21]. Another common disturbed type is the lap strap joint. The single lap strap joint (Figure 2-1c), which uses an additional butt strap, results in a reduction of peel stress at the ends of the overlap [22]. The double lap strap joint (Figure 2-1d) eliminates the issue of peel stress and offers superior strength properties [20]. However, the use of butt straps leads to greater manufacturing complexity, increased structural weight, and diminished aerodynamic performance, which are critical limitations in aerospace engineering.

The butt joint (Figure 2-1e) is the simplest and easiest type to manufacture when the adherends have sufficient thickness. However, aligning the two adherends can be challenging. This joint performs well under bending loading, which can result in cleavage stresses for the adhesive layer [23]. The scarf joint (Figure 2-1f), formed by chamfering the adherends at an angle, performs well mainly because it eliminates joint eccentricity. Under tensile loading, there is an optimal scarf angle at which stress singularities are avoided, resulting in a uniform stress distribution near the edges of the bond [24]. The step joint (Figure 2-1g) is essentially a single overlap, where portions of the adherends are reduced to half of their original thickness to form the overlap area. This design can reduce peel stress. To achieve a smoother stress distribution, multiple steps can be incorporated [25]. Under quasi-static loading, the stepped lap joint exhibits greater damage tolerance than the scarf joint [26]. The tongue and groove joint (Figure 2-1h) is a unique type of multi-stepped lap joint, offering a promising alternative for

enhancing the joint strength. This is due to its more gradual load transfer to the adherends, which results in lower peel stress compared to the SLJ [27]. However, milling operations are required for the adherends in both the scarf and step joints, making these joints more complex and costly to fabricate [28].

2.2.2. Hybrid joining

Although there is a growing demand for composites for lightweight structures, the low through-thickness strength and poor heat resistance of composites make the use of fully composite structures impractical in many large-scale applications. As a result, there has been an increased focus on hybrid joining techniques that combine dissimilar materials, such as metals and composites, as shown in Figure 2-2. However, hybrid adhesive joints with dissimilar adherends present several critical challenges, as the mismatch in material properties between dissimilar adherends leads to asymmetric stress distributions and more complex failure mechanisms compared to the joints bonded with identical materials, thereby elevating the overall design risk [29].

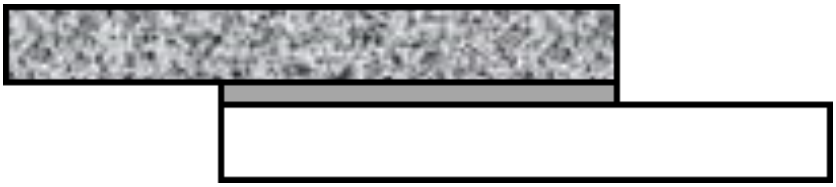

Figure 2-2. Hybrid joining with dissimilar adherends.

Stuparu investigated the behaviour and strength of hybrid SLJ bonded with Al and carbon fibre reinforced polymer (CFRP) using a combination of Cohesive Zone Model (CZM) and eXtended Finite Element Method (XFEM). This study finds that the overall strength of hybrid joints is decreased compared to Al-Al SLJ due to carbon fibre delamination and pull-out [30]. Hazimeh conducted a three-dimensional numerical

analysis of adhesive DLJ with dissimilar adherends under in-plane impact loading. The results indicate that the joints bonded with dissimilar adherends exhibit higher maximum shear stress, primarily due to the loss of homogeneity caused by stiffness mismatch and the edge effects resulting from adherend discontinuities [31].

Sun developed an experimental study on adhesive joints bonded with identical and dissimilar materials using the Digital Image Correlation (DIC) technique. For the joints with identical adherends, the fracture process is found to be symmetric, with cracks initiating at the ends of the overlap region and propagating toward the centre. In contrast, the joints with dissimilar adherends exhibit asymmetric fracture behaviour [32]. Liao conducted both experimental and numerical studies on the fracture behaviour of hybrid SLJs. The findings reveal that, under impact tensile loading, damage initiates at the interface of the adherend with the higher Young's modulus. This behaviour contrasts with that observed under static loading, where damage typically initiates near the interface edge of the adherend with the lower Young's modulus [33]. Zhang experimentally and numerically investigated the fatigue behaviour and failure mechanisms of adhesive joints with identical and dissimilar adherends. The results indicate that the damage in CFRP–Al joints propagates from the CFRP side toward the Al side, eventually leading to fracture near the Al end. In contrast, the damage in CFRP–CFRP and Al–Al joints is symmetrically distributed along the central axis of the overlap region [34].

In some applications, a simple adhesive joint may not offer sufficient strength [35, 36]. To enhance the performance of adhesive joints, several hybrid joining methods that combine adhesive bonding with other joining techniques have been developed. As illustrated in Figure 2-3, four common types of hybrid joining techniques include hybrid

bolted–bonded (HBB) joints, hybrid riveted–bonded (HRB) joints, hybrid pinned–bonded (HPB) joints, and hybrid welded–bonded (HWB) joints.

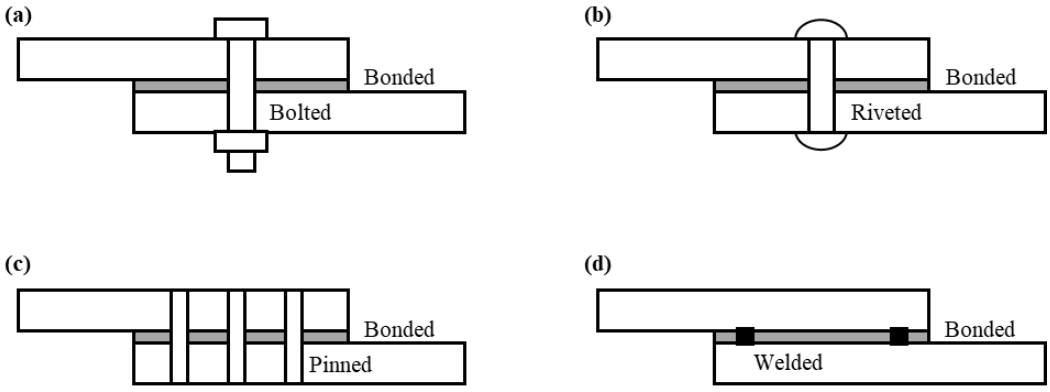

Figure 2-3. Hybrid joining technique. (a) Bolted-bonded joint. (b) Riveted-bonded joint. (c) Pinned-bonded joint. (d) Welded-bonded joint.

A HBB joint integrates bolting and adhesive bonding to connect two components, which is the most widely used hybrid joining techniques. The HBB joints offer structural reliability by ensuring functionality even if the adhesive layer fails [37]. By combining the safety and robustness of bolts with the efficient load transfer capabilities of adhesive bonding, HBB joints achieve higher load capacities than either bolted or bonded joints alone. The bolts mitigate peel stress, while the adhesive reduces stress concentrations around the bolts, resulting in enhanced joint strength [38, 39]. Lopez-Cruz investigated how adherend thickness, adhesive modulus, clamping area, and bolt-hole clearance affect the strength of the HBB joints. The findings indicate that the adherend thickness has positive effects on the joint strength, while the adhesive modulus, clamping area, and the bolt-hole clearance have negative effects. The adherend thickness and adhesive modulus show the greatest effect on the results [40].

A HRB joint combines the use of riveting with adhesive bonding, which is another hybrid joining technique. However, unlike bolts, rivets are permanent fasteners. Chen investigated the performance and failure mechanism of solely bonded, riveted,

and HRB joints using CFRP and Al materials. The results indicate that the HRB joint can effectively prevent catastrophic failure while exhibiting significantly higher energy absorption [41]. Sadowski reported similar findings by modelling the damage and failure mechanisms of HRB joints using FEM, with the results further validated through experiments [42].

A HPB joint is designed to overcome the shortcomings of both the bonded and the bolted joints. The HPB joints can enhance delamination resistance and improve damage tolerance compared to the solely bonded joints [43]. Additionally, HPB joints can eliminate the need for drilling holes in the composite adherend, thereby avoiding fibre damage in the laminate and the added weight associated with fastening systems [44]. The pin types that can be used in the HPB joints are illustrated in Figure 2-4. Li combined experimental and numerical methods to investigate the failure load and failure modes of adhesively bonded and HPB SLJs. The investigation finds that reinforcing the SLJ with a CFRP pin achieves a 19.1% increase in the ultimate failure load under static tension. This improvement in strength is attributed to the load sharing between the pin and adhesive, as well as the increased out-of-plane bending stiffness, which reduces peel stresses in the bonding overlap [45].

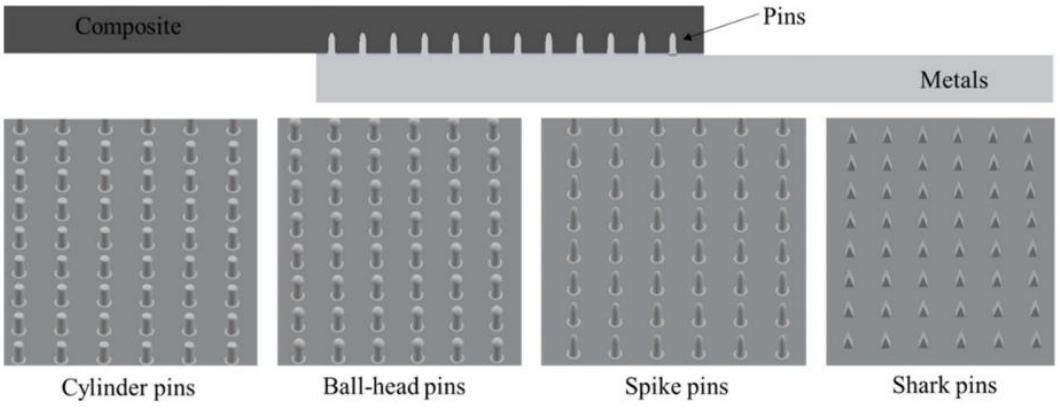

Figure 2-4. Pin types in HPB joints [46].

A HWB joint combines spot welding with adhesive bonding in the overlapping areas. Compared to other hybrid joining methods using mechanical fasteners, weld-bonding offers several advantages, including higher static strength, enhanced fatigue resistance, improved corrosion protection, lower manufacturing costs with compatibility for mechanization, and superior acoustic performance [47]. Marques evaluated the performance of adhesives with varying ductility in HWB joints and purely bonded joints, aiming to identify the most suitable adhesive. The experimental and numerical results show that more ductile adhesives perform better in bonded joints and HWB joints, due to their ability to approach global yielding conditions, particularly in cases with short overlaps [48].

2.2.3. Failure mode

The initial cracks in adhesive joints are critical, as they can initiate further damage and significantly influence the mechanical behaviour of adhesive joints under applied loading. Crack initiation in adhesive joints commonly occurs at locations with high stress concentrations, such as the edges of the bonding overlap or points of sudden geometric change [49]. In particular, the significant mismatch in stiffness between the adherends and the adhesive intensifies stress concentrations at the joint edges, causing cracks to initiate once the critical load is reached [50]. Crack propagation in adhesive joints is a complex phenomenon influenced by several factors. In general, an increase in adhesive thickness results in reduced constraint and consequently larger plastic deformation, which leads to lower crack growth rates for adhesive joints [51]. Adhesive joints with notched adherends can delay the crack propagation compared to conventional joints. This is mainly because a larger portion of the applied energy is

dissipated through the elastic and plastic deformation of the adherends, rather than being used for the fracture of the adhesive layer [52].

Crack propagation in adhesive joints leads to different failure modes of adhesive joints, including adhesive (interfacial) failure, cohesive failure, fibre-tear failure, light fibre-tear failure, stock-break failure, or mixed failure (a combination of two or more failure modes). Among these, failure modes only occur within the adherend material, such as fibre-tear failure, light fibre-tear failure, and stock-break failure, which can be categorized as adherend failure. Accordingly, this subsection focuses on explaining three of the most common failure modes: adhesive failure, adherend failure, and cohesive failure, as illustrated in Figure 2-5.

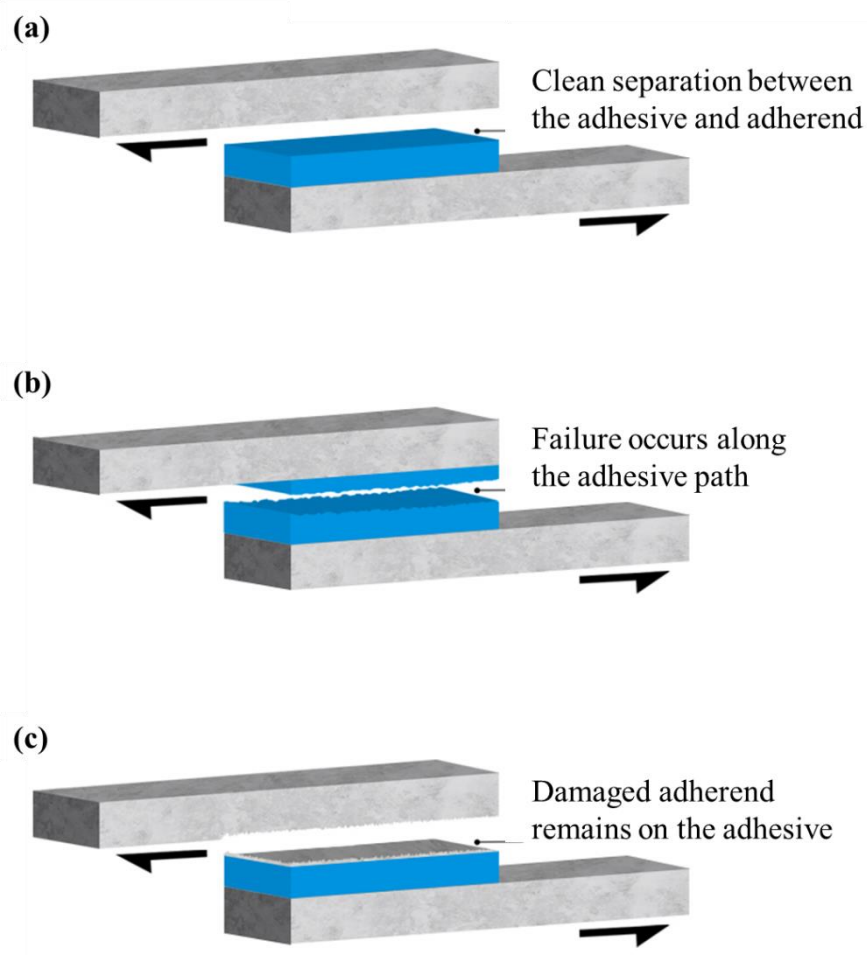

Figure 2-5. The main failure mode in adhesive joints [53]. (a) Adhesive failure. (b) Cohesive failure. (c) Adherend failure.

Adhesive failure occurs at the adhesion interface between the adhesive and the adherends if the applied stress exceeds the bonding strength, as shown in Figure 2-5a. This type of failure is caused by poor surface quality of the adherends and degradation of the chemical bonds between the adhesive and the adherends. Contamination on the adherend surface can affect the formation of a chemical bond between the adherend and adhesive, which may result in adhesive failure [54]. In addition to the effect of the manufacturing process, other factors can also induce adhesive failure in adhesive joints. These factors include fatigue, adhesive creep, and peel stresses [55].

Cohesive failure occurs when the adhesive layer breaks along its own thickness, as shown in Figure 2-5b. To be classified as cohesive failure, there must be a distinct adhesive layer on both surfaces of the adherends. This type of failure can result from shear, peel, or a combination of both shear and peel stresses acting on the adhesive layer. Cohesive failure can be caused by design flaws, such as insufficient overlap length and defects in the adhesive layer [56]. However, cohesive failure in adhesive joints is regarded as the ideal failure mode because it indicates that the joint has achieved the maximum strength of the materials involved.

Adherend failure occurs within the adherend when the mechanical strength of the adherends is lower than the bonding strength of the adhesive, as shown in Figure 2-5c. This type of failure is commonly observed in adhesive joints using thin and brittle adherends. Although it indicates strong bond performance of the joints, the adherend is not suitable for the selected adhesive type. Additionally, adherend failure frequently takes place in the hybrid joints using dissimilar adherends, especially when the metal adherend is weakened by corrosion. In composite adherend, the failure load direction depends on the stacking angle of the contact ply [57].

Although many previous studies have focused on the crack initiation, crack propagation, and failure mode of adhesive joints, there is still a lack of detailed investigations specifically into the fracture mechanisms at microscale.

2.3 Influencing factor on joint performance

Adhesive joints have a significant advantage over traditional mechanical joints by providing a more uniform stress distribution in the bonding overlap [13]. However, the effectiveness and mechanical behaviour of adhesive joints depend on a range of influencing factors. This section provides a detailed discussion on how these primary factors influence the performance and reliability of adhesive joints.

2.3.1. Joint geometry

The geometry of adhesive joints plays a crucial role in determining their strength and the stress distribution within the adhesive layer. In general, the overall strength of adhesive joints is primarily governed by the peak stresses experienced in both the adhesive and the adherends [58].

2.3.1.1. Geometry of adherend and adhesive

The bonding overlap length can have a significant effect on the performance of adhesive joints. The studies reveal that the overlap length affects joint strength differently depending on the type of adhesive. In joints bonded with ductile adhesive, the strength increases almost linearly with longer overlap lengths, whereas joints bonded with brittle adhesive show only limited enhancement of the strength [59, 60]. Some research finds that the joint strength increases initially with a longer length of the

overlap. However, beyond a certain threshold recognized as the effective value, further increasing the overlap length does not improve the bond strength [61].

The length and thickness of the adherend and adhesive are also the crucial factors that affect the joint performance. For low-strength adherends, a greater thickness enhances their robustness, which can reduce the likelihood of plastic deformation and improve the joint strength. In contrast, for high-strength adherends, a greater thickness can lead to increased bending moments at the bonding overlap due to loading eccentricity, which may reduce the overall joint strength [62]. In the study using carbon composite and steel as the adherends, Song discovered that the joints with a thicker adherend exhibits a higher failure strength [63].

Many studies indicate that the optimal adhesive thickness for the maximum strength of adhesive joints typically falls within the range of 0.1 mm to 0.5 mm [64-66]. However, this optimal range can vary depending on the type of the adhesive. Campilho examined the performance of polyurethane adhesive joints with thicknesses ranging from 0.1 mm to 2 mm and found that the joints with thicker adhesive layers exhibit improved strength properties [67].

2.3.1.2. Geometrical discontinuities

To reduce the high stresses at the edges of the bonding overlap of adhesive joints, many methods have been proposed by incorporating geometric discontinuities in the adherend and adhesive, such as tapers, holes, fillets, round corners, and notches. Figure 2-6 illustrates some geometric discontinuities in adhesive joints, including adherend tapering and rounding, along with their combinations with adhesive fillets.

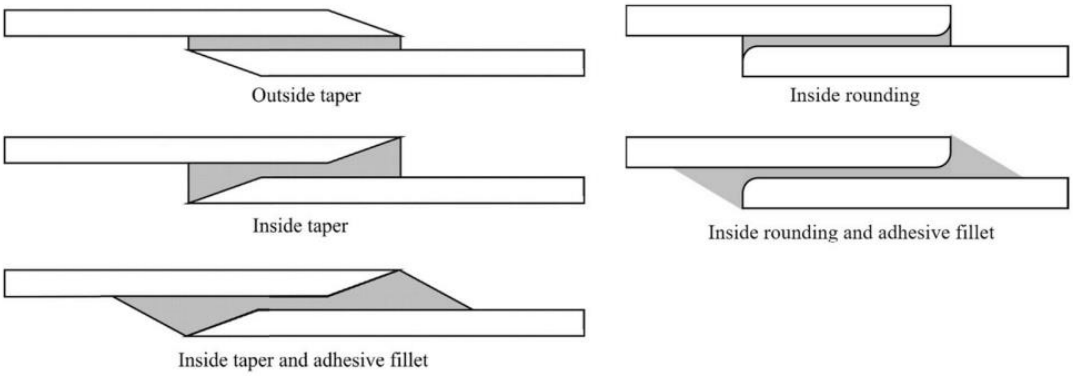

Figure 2-6. Different geometrical discontinuities in adherend and adhesive [68].

It is found that both inside and outside tapering of adherends are effective methods for reducing the loading eccentricity and stress concentration at the ends of the bonding overlap. This reduction in eccentricity decreases the peak peel stresses at the overlap ends, thereby enhancing the overall joint strength [69, 70].

Furthermore, Haghani revealed that the effect of tapering on stress distribution is significantly determined by the stiffness of the adherends and the adhesive used in the joint. The study demonstrates that tapering is more effective in joints with softer adherends and stiffer adhesives. Additionally, the inside tapering is found to be more effective in reducing stresses compared to that of the outside tapering [71]. It is also found that rounding the corners of the adherend can significantly reduce the stresses [72]. Zhao investigated the stress singularity at the adherend corners of the ends of the overlap using brittle and ductile adhesives. The strength of SLJs with a large radius of the adherend corners increases by approximately 40% compared to that of the standard joints using a brittle adhesive. For joints with a ductile adhesive, rounding the adherend corners has no significant effect of the joint strength. This different effect is due to the different failure mechanisms of joints bonded with brittle and ductile adhesives [73, 74].

Abrupt or sharp changes in the profile of the adhesive at the overlap ends can significantly affect the mechanical strength of joints, particularly in SLJs where loading

eccentricity plays a critical role. Fillets are formed through excess adhesive that is squeezed out during manufacturing process. Unlike normal joints, where stress concentrations are highest at the ends of the bonding overlap, fillets can create a smoother load transfer path and a greater load transfer region, thereby improving the joint performance [75]. Dorn observed that the spew fillets in the plastic-metal SLJs reduce the peak peel and shear stresses compared to the joints without fillets, along with a reduction in stress and strain concentrations at critical regions of the adherends [76].

2.3.2. Constituent materials and interface

An adhesive bonded joint is comprised of three fundamental regions: the adherend, adhesive, and interface connecting the adherend with adhesive. While numerous studies investigate how the geometry of both the adherend and the adhesive affects the joint performance, other research focuses on the influence of mechanical properties of materials on the overall behaviour of the joint.

2.3.2.1. Adherend material

According to the existing studies on the adhesive joints with identical and dissimilar adherends, it is found that the stiffness of the adherend has a significant effect on the overall joint performance. An increase in adherend stiffness can decrease the peak peel and shear stresses at the ends of the overlap, thereby enhancing joint strength [29, 77].

With the growing use of composites as the adherends, many researches have been conducted on adhesive joints bonded with composite materials. For the application of composite adherend in SLJs, there are several methods to improve the joint

performance. Ganesh numerically demonstrated the effectiveness of using the graded adherends to enhance the bonding of composites. Due to more uniform stress distribution of the SLJs bonded with the graded adherends, the joint strength increases by 20% [78]. Guin observed that the peak peel stress within the adhesive decreases by 27%, through incorporating a stiffer layer into the composite adherend adjacent to the adhesive compared to that obtained with a softer layer [79]. To address the premature failure of the joints caused by the delamination of the composite adherends, enhancing the transverse toughness of the adherends can effectively reduce their susceptibility to delamination [58].

2.3.2.2. Adhesive material

In adhesive joints, ductile adhesives exhibit higher toughness and are capable of withstanding greater deformation prior to failure, whereas brittle adhesives are more prone to fracture and possess limited energy dissipation capacity. These contrasting behaviours have important implications for the strength and durability of the joints. To optimize the stress distribution and joint performance, the graded adhesive is a technique that alters stress distribution by adjusting the arrangement or properties of the adhesive, resulting in a more uniform distribution of stress in both the adhesive and adherends. There are two common approaches to achieve graded adhesive in adhesive joints. One approach involves using a mixed adhesive (as illustrated in Figure 2-7), while the other involves local reinforcement with rubber particles or other toughening particles, such as carbon nanotubes (CNT), clays, and various oxides [68].

The stress at the bonding overlap can be reduced by using low modulus adhesive (ductile adhesive) at the ends of the bonding overlap. By applying ductile adhesives at the ends of the overlap and a brittle adhesive in the middle region, the mixed adhesive

joint achieves a more uniform stress distribution [80]. The experimental results demonstrate that the strength of the mixed adhesive joints is 40% greater than that of joints bonded with single adhesive [81].

Ejaz observed similar results by introducing CNTs into the adhesive, which enhanced the plastic response of the modified adhesive and further improved the fracture toughness of the joint. However, excessively dense CNTs can reduce joint strength, because they serve as points of stress concentration that accelerate the crack propagation [82].

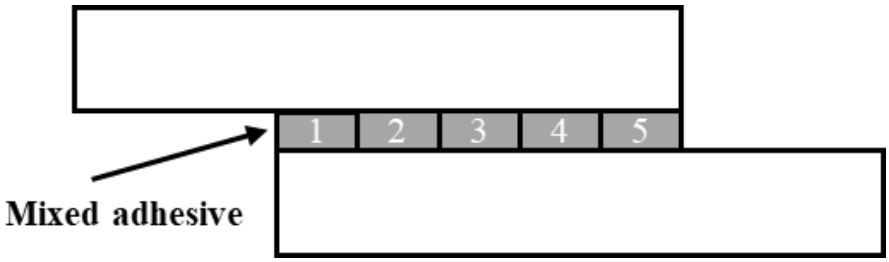

Figure 2-7. Example of adhesive joints with mixed adhesive.

As illustrated in Figure 2-8, defects that may occur in the adhesive, such as voids, porosity, and disbonds, can negatively affect joint performance. Generally, porosity refers to clusters of micro-voids within adhesive bonds, whereas voids are larger regions entirely devoid of adhesive. The emergence of these defects is attributed to the entrapment of air or gases during the application of adhesive, insufficient application of the adhesive, and the presence of contaminants on the adherend surface, such as grease [83, 84]. Porosity and voids tend to accumulate more in the middle of the joints, with fewer occurring near the edges where air bubbles can escape more easily. Meanwhile, there is not a well-received agreement regarding the influencing mechanisms of defects, which inevitably occur within adhesive joints even under rigorous manufacturing controls [85].

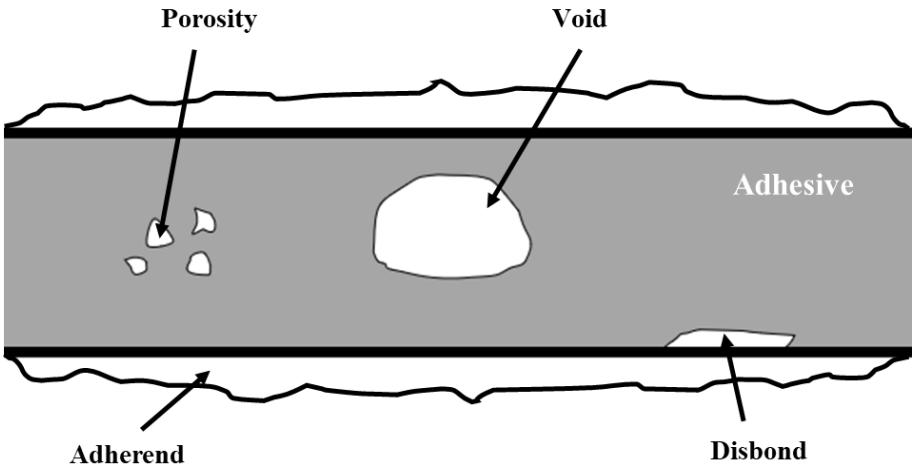

Figure 2-8. Defects in adhesive joints.

The results demonstrate that the strength of an adhesive steel joint is generally insensitive to the presence of defects within the adhesive layer [86]. Another investigation also finds that the presence of a void of a reasonable size at a specific location exerts minimal influence on the load-carrying capacity of the joint [87]. Other researchers argue that the effect of defects within the adhesive layer on the performance of adhesive joints depends on several factors. A defect within the adhesive layer situated near the lap ends of a joint can induce a significant reduction in fracture strength due to the high stress concentration at the lap ends. When the defect is positioned in the middle region of the overlap, the decrease in fracture strength is relatively minor [88].

Furthermore, the defects within the adhesive layer can significantly degrade the mechanical integrity of the adhesive with a strong interfacial strength. In contrast, their influence on the failure response of the adhesive with an insufficient interfacial strength is negligible [89]. Another study demonstrates that the effect of the defect within the adhesive layer significantly depends on the adhesive type. It has a greater impact on the performance of the joints bonded with ductile adhesive in comparison to those bonded with brittle adhesive [90]. Richard numerically found that the incorporation of local

defects in some cases could result in joint strengths exceeding those predicted by the simulation without defects. This outcome is attributed to the promotion of more progressive failure throughout the entire joint structure [91]. Consistent with other numerical studies, defects are modelled as a two-dimensional feature spanning the entire adhesive thickness, which oversimplifies actual conditions. Moreover, the lack of established acceptance criteria for porosity tolerance constrains the practical applicability of the findings.

Through X-ray microtomography, Dumont found that tensile loading could induce the nucleation of new defects and the coalescence of existing ones, which in turn may lead to premature failure. Moreover, the most pronounced geometric transformations of the pores are observed in the middle region of the adhesive layer thickness [92]. Ahmed examined the interaction between defects and cracks in adhesive joints. The study reveals that defects have a negligible effect on Mode I crack propagation but exert a significant influence on Mode II crack growth, particularly when located near the crack tip. Flatter and more elliptical defects are shown to be particularly detrimental due to alterations in the crack deflection angles [93]. Although many previous studies have focused on the performance of adhesive joints with defects, there is still a lack of detailed investigations specifically into the failure mechanisms at microscale.

2.3.2.3. Interface

The enhancement of the adhesion of the interface between adherend and adhesive is crucial to improve the overall joint performance, usually achieved by proper surface treatments [94]. Thus, substantial investigations have been dedicated to studying different treatments for adherend surface, encompassing surface cleaning [95],

laser treatments [96, 97], mechanical treatments [98-100], and acid chemical etching [101, 102]. Furthermore, the adhesion criterion requires that the adhesive have a lower surface tension than the substrate for good wetting. As a result, the epoxy adhesive exhibits weaker adhesion to the polymeric substrate compared to the metal substrate [103].

As one of the results of surface treatments, surface roughness is recognized as a critical evaluative parameter for surface characteristics, exerting significant effects on the performance of adhesive joints. It has been investigated that the correlation between the tensile strength of an adhesive joint and the surface roughness of the adherend is not merely proportional or inversely, exhibiting an optimum value [104]. To determine the optimal surface roughness for specific adhesive joints, researchers conducted several experiments to investigate the performance of joints [105, 106]. The literature highlights the pivotal role of surface roughness in establishing a reliable bond, as it effectively enlarges the contact area and provides strong mechanical interlocking between the adhesive and adherend [107].

Some researches have found that appropriate surface roughness can increase the contact area and facilitate more bonds between the bonded materials, thereby improving joint strength [108, 109]. Other studies have shown that the improving performance of adhesive joints with rougher adherend surface is attributed to the mechanical interlocking [110, 111]. Figure 2-9 presents the mechanical interlocking between the adhesive and the adherend. Furthermore, Kewon found that the suitable surface roughness could contribute to the optimal mechanical interlocking [112]. However, Yang claimed that the trend of tensile strength for adhesive joints could not be solely elucidated by increasing roughness characteristics associated with mechanical

interlocking. It was also associated with the surface energy, correlated to the effect of adsorption [104].

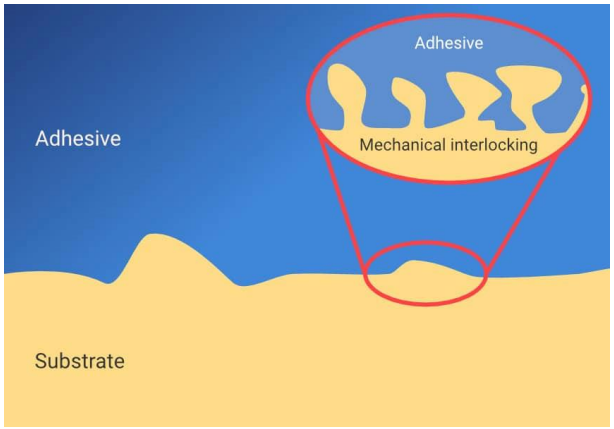

Figure 2-9. Mechanical interlocking in adhesive joints [113].

Moreover, Marinosci investigated the effect of surface roughness on the fracture toughness of titanium–thermoplastic composite joints. Their results show that increasing surface roughness significantly enhances the fracture toughness of the hybrid interface, until it reaches a threshold value of approximately 2.5 μm [114]. Shokrian conducted several surface treatments on Al adherends and found that chemical treatments, such as acid etching, could significantly increase the surface roughness, leading to higher joint strength and promoting cohesive failure, whereas mechanical treatments that produce lower roughness result in weaker joints with a higher likelihood of adhesive failure [115]. Andrea explored the effects of surface roughness, induced by sandblasting, on the Mode-I behavior of flax/epoxy adhesive joints. The study shows that increasing adherend surface roughness can influence Mode-I joint performance, with an optimal roughness maximizing bonding strength, while further increases in roughness reduce fracture energy [116]. Although many previous studies have dedicated on the joint performance in consideration of surface roughness, there are no sufficient investigations specifically addressing the failure mechanisms of joints at microscale to clarify the effects of roughness on joint performance.

Additionally, the defect on the interface has the potential to significantly undermine the strength of adhesive joints [89]. This kind of defects can cause significant loss of adhesion in adhesive joints [117]. It is found that the presence of the interfacial defects within the bonding region can elevate stress concentrations, especially at the edges of the bonding region, and further lead to premature failure and debonding of the joints [118]. Furthermore, premature failure at the edges of the joint decreases the peel strength of the joints [119]. With the increased size of interfacial defects, the joint strength decreases [120]. A comprehensive numerical study conducted by Cheikh focusing on adhesively bonded pultruded GFRP lap joints containing bondline defects of varying location, size, and number confirmed these effects. The results show that the number and position of bondline defects have the most significant impact on out-of-plane displacement and stress concentrations, particularly near the overlap ends, while the size of bondline defects has a smaller influence [121].

2.3.3. Environmental factors

As illustrated in Figure 2-10, several environmental factors can affect the strength and durability of the adhesive joints, including temperature, moisture, and ultraviolet radiation. In general, temperature and moisture absorption are the primary environmental factors influencing the strength and durability of adhesive joints.

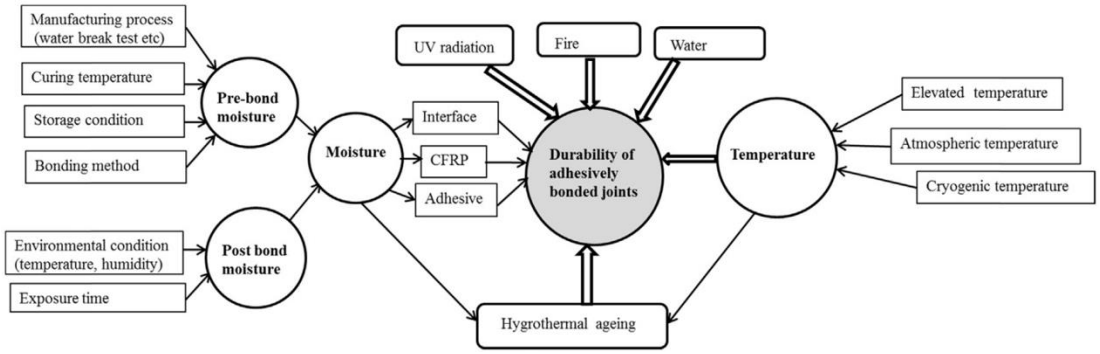

Figure 2-10. Environmental factors affecting the durability of adhesive joints [122].

In adhesive joints, adhesives and resin matrices are significantly affected by moisture. Moisture typically influences the properties of adhesives by increasing their ductility while decreasing their elastic modulus and strength [123]. The study of pre-bond moisture examines the effect of the moisture content in the adherend before bonding on the performance of the adhesive joints. The pre-bond moisture issue is particularly crucial for the joints bonded with polymeric-composite adherends. The study finds that the presence of moisture in the composite leads to a reduction in joint strength [124]. Additionally, the presence of pre-bond moisture in the adherend significantly changes the failure mode of adhesive joints, shifting from cohesive failure to interface failure, and additionally, multiple crack failures can occur when pre-bond moisture is present [125].

With the increasing demand for the adhesive joints to withstand high temperatures in the automotive and aerospace industries, some researches have been conducted to study the effects of temperature on joint performance and ways to ensure the structural integrity of the joints in such environments. The key factors influencing the performance of the adhesive joints across a broad temperature range are cure shrinkage, thermal expansion coefficients, and the variation in mechanical properties of adhesive [126]. The experimental studies on the adhesive joints bonded with structural adhesives (particularly epoxies) demonstrate a reduction in the joint strength with the

increase or decrease of temperature. At higher temperatures, it is attributed to the decreased strength of the adhesive, while at lower temperatures, it is due to the high thermal stresses and the brittleness of the adhesive [127, 128].

2.4 Analysis method of adhesive joints

Adhesive bonded joints can be analysed using analytical methods and numerical methods. Analytical methods are fast and easy to analyse the adhesive joints. However, analytical methods rely on certain assumptions for the complex joints, which can affect the accuracy of the results. In contrast, numerical methods, such as FEM, can handle complex geometries and material behaviours without assumptions. Although analytical methods still play a role as an initial indicator of joint performance, they have been largely replaced by numerical methods [122, 129].

2.4.1. Analytical method

Over the years, several analytical methods have been developed to predict the performance of the adhesive joints, significantly reducing the need for costly testing and analysis time. The simplest linear elastic analysis focuses on the most common single lap joint. This analysis assumes that the adhesive deforms exclusively in shear, with the adherends treated as rigid [130].

Volkersen proposed a shear lag model for adhesively bonded lap joints and introduced the concept of differential shear. It assumes the adherends are under tension, and the adhesive experiences only shear stress. Both stresses are constant across the thickness. Meanwhile, the model assumes the adhesive is stiff and does not bend under load [131]. Therefore, for cases that adhesive joints experience plastic deformation or

significant peeling, a more advanced model is required. Goland extended this study by considering the bending effect of adherend, which results in peel stress in the adhesive layer [132].

With the growing use of composites in adhesive joints, many studies have focused on developing analytical methods for joints that use composite materials. To investigate the effects of adhesive thickness and loading conditions on stress distributions within the adhesive layer, Yousefsani proposed an analytical solution for SLJs bonded with composites using the full layerwise theory [133]. Wah firstly analysed the laminated composite adherends that are symmetrical about their midsurface. In this analytical model, shear stress within adhesive is assumed to be constant across the thickness, while peel stress can vary [134]. Additionally, Yang investigated the asymmetric composite adherends in both balanced and unbalanced joints, taking into account the coupled effects of the external tensile loading and bending moments caused by the asymmetry of the composite laminates [135].

Mortensen proposed a unified approach for adhesive joints with composite adherend. In this approach, the adherend is modelled as a beam or wide plate under cylindrical bending and is considered as an orthotropic laminate using classical laminate theory. The adhesive is assumed to be a linear elastic material, or, alternatively, the inelastic behaviours of many adhesives is considered [136]. Based on the unified approach, Zhang developed a method for analysing multi-axial stresses in composite joints, incorporating transverse in-plane strain and hygrothermal effects, and enabling the computation of both in-plane and interlaminar stresses in the adherends [137].

The stress distributions of the adhesion interface in adhesive joints are significantly influenced by the loading and boundary conditions. However, there are no practical experimental techniques available to directly determine these stress

distributions [122]. Yousefsani developed new analytical solutions for SLJs bonded with composites under different boundary and loading conditions, based on the energy method and Timoshenko's beam theory. These loading and boundary conditions can have a significant effect on the interfacial stress distributions within the adhesive layer [138]. Wu established a novel self-consistent stress-function variational method for analysing the stress in adhesive bonded joints. The entire stress field of the joint can be consistently represented by four functions of the interfacial stress on the two interfaces, within the framework of Euler-Bernoulli beam theory and linear elasticity. This method offers the advantage of generality and ensures that the stress-field solution satisfies all the multiple traction boundary conditions at both the adherend ends and across the interfaces [139]. Wang proposed a novel three-parameter elastic foundation model to analyse the interfacial stresses in adhesively bonded joints. In this model, the adhesive layer is designed as two normal spring layers interconnected by a shear spring layer. The new model satisfies all boundary conditions and accurately predicts which interface experiences the highest stress concentration [140].

2.4.2. Numerical method

As the design of the adhesive joints becomes increasingly complex, analytical methods are difficult to provide accurate predictions. This is because the mechanical behaviours of the joints are influenced not only by their geometry but also by material properties and varying boundary conditions. The combination of increasingly complex geometries and three-dimensional nature of the joints makes it challenging to formulate a comprehensive system of governing equations for predicting the mechanical properties of the joints [122, 129]. Therefore, numerical methods are the preferred choice for predicting the mechanical behaviours of adhesive joints. Among the different

numerical methods for adhesive joints, FEM is the most commonly applied and DEM is increasingly used.

2.4.2.1. FEM

FEM is based on continuum mechanics and discretizes the analysis domain into finite elements connected at nodes. The general governing equation for static analysis can be expressed as:

$$[K]\{u\} = \{F\} \tag{2-1}$$

where $[K]$ is the global stiffness matrix, $\{u\}$ is the vector of nodal displacements, and $\{F\}$ is the vector of applied nodal forces.

FEM enables the analysis of stress and strain distributions in adhesive joints, facilitates the prediction of their failure mechanisms, and supports the optimization of joint designs. This is accomplished by developing a detailed numerical model of the joint, which allows for the simulation of different loading conditions, geometries, and material characteristics. Several approaches can be utilized to evaluate the failure of adhesive joints.

Some strain-based failure criteria have been developed to predict the failure behaviour of adhesive joints. Ayatollahi proposed the Critical Longitudinal Strain (CLS) criterion, a strain-based approach that relies on two key parameters: the critical longitudinal strain, which is the experimentally determined strain at which failure initiates in the adhesive layer, and the critical distance, defined as the location along the adhesive mid-plane where this strain is reached. According to this criterion, failure in a SLJ occurs when the longitudinal strain along the adhesive mid-plane reaches the critical longitudinal strain at the defined critical distance [141]. Razavi introduced a new criterion called the critical normal strain criterion for predicting the failure load in

adhesively bonded double strap joints, based on the normal strain along the adhesive mid-plane. This criterion determines the joint strength by using a critical normal strain at a specific critical distance, similar to that of the CLS criterion, but with normal strain instead of longitudinal strain. Furthermore, This criterion is mesh-independent and provides accurate predictions for the joint strength [142].

The Continuum Damage Model (CDM) uses a damage parameter to model the stiffness degradation of adhesive elements, allowing it to predict both crack initiation and growth. García employed the CDM to predict the initiation and propagation of cracks in a joint bonded with a ductile and tough adhesive. The model uses the Drucker-Prager exponential criterion to describe the elasto-plastic behaviour of the adhesive, with a linear softening. The results accurately predict the crack path (Figure 2-11) and joint strength, compared to those of experimental results [143]. Zhang applied the CDM with linear softening to study the strength of a joint bonded with dissimilar adherends, and the numerical results are consistent with the experimental findings. Based on this model, the effect of different metals and composite stacking sequences on joint strength is investigated [144].

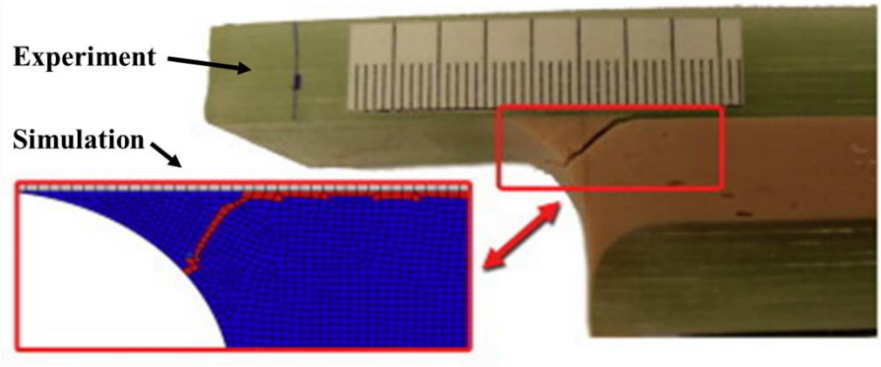

Figure 2-11. Experimental and numerical cacks in the adhesive joint [143].

The CZM combines a strength-based failure criterion to predict the damage initiation with a fracture mechanics-based criterion to determine the crack propagation.

This approach employs specially paired nodes that follow a defined cohesive law, such as the traction-separation law [145]. There are two primary approaches for the CZM: the local approach and the continuum approach, as illustrated in Figure 2-12. In the local approach, cohesive elements are used to connect superimposed nodes of elements, representing a zero-thickness interface in adhesive joints. In contrast, the continuum approach uses cohesive elements to model the entire adhesive bond, with a finite thickness connecting the two adherends [129].

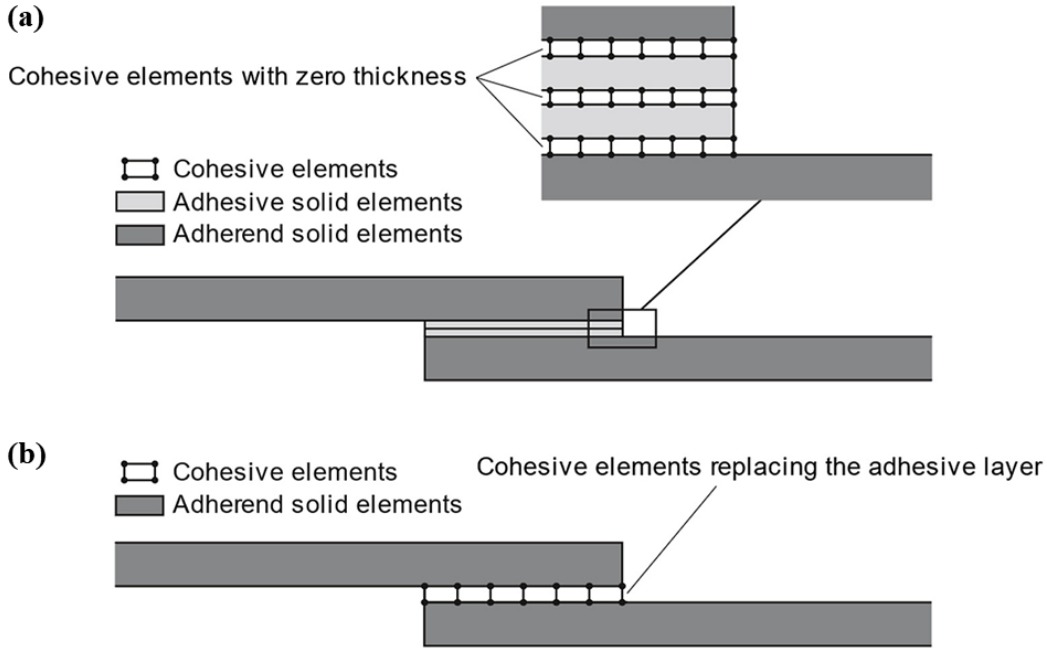

Figure 2-12. Cohesive element in SLJ [129]. (a) Local approach. (b) Continuum approach.

O'Mahoney conducted a Taguchi analysis for SLJ bonded with composites. A CZM is employed to represent the interface, while a CDM is used for the adhesive bondline. The study numerically examines the effects of the interfacial adhesion and adhesive strength on the performance of the bonded composite SLJ [146]. Campilho evaluated the strength predictions of the SLJs with varying overlap lengths using different cohesive law shapes. The study finds that the triangular laws are better suited

for the brittle adhesives, whereas trapezoidal laws are more appropriate for the ductile adhesives [147]. Nunes analysed the strength of the SLJ and DLJ with three different adhesives using the CZM. The study reveals that the DLJ exhibits approximately twice the strength of the SLJ when the same adhesive is used. The strength prediction from the CZM closely matches the experimental results [148]. Moya-Sanz investigated the effect of geometric modifications on the strength of the SLJs using a ductile adhesive. According to the result from the CZM, it shows that recessing the adherends can enhance the joint strength, while chamfering both the adhesives and adherends lead to a greater increase in the joint strength [149].

XFEM can predict the fracture in a material without requiring prior knowledge of the crack path within the finite element mesh. Compared to the CZM, the crack can propagate freely within the elements, independent of element boundaries, eliminating the need to define a specific crack path or an initial crack in the structure. Santos employed XFEM to model damage mechanisms in adhesive joints reinforced with inorganic fillers. Compared to the experimental results, the XFEM effectively predicts the failure modes of the bonded joints [150]. Additionally, based on the numerical results for the DLJs with three different adhesives using XFEM, the research finds that the stress-based criteria provide the most accurate results, showing minimal errors for all adhesives [151]. Mubashar combined XFEM with CZM to study the SLJs with fillets, utilizing a triangular CZM at the adhesion interfaces and XFEM for the remaining adhesive, including the fillet. This method provides accurate predictions for the joint strength and fracture. The numerical cracks initially occur in the fillet region near the bottom adherend and then propagate towards the top adherend and along the interface [152].

2.4.2.2. DEM

DEM was proposed by Cundall to study rock mechanics in 1971, which was used to reflect the discrete characterization of system [153]. In a two-dimensional DEM model, as illustrated in Figure 2-13, the material domain is discretized using particles A and B, each possessing mass. These particles, typically assumed to be rigid and circular, are bonded at a contact. They interact through the contact and will separate once the bond strength or fracture energy threshold is exceeded.

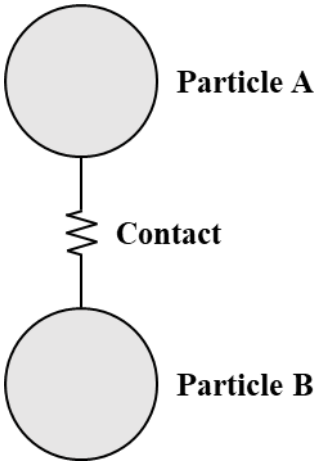

Figure 2-13. Particle and contact in DEM.

The system is considered to be in dynamic equilibrium when the internal forces among particles are balanced. Under the external loads, the motion of the particle is governed by Newton's second law:

$$F_i = m(\ddot{x}_{d\_i} - g_i) \tag{2-2}$$

$$M_3 = I\dot{\omega}_3 \tag{2-3}$$

where $i\ (=1,2)$ denotes the x and y coordinate directions, respectively, F_i is the resultant force or the sum of all externally applied forces acting on the particle, m

represents the mass of the particle, $\ddot{x}_{d\_i}$ is the acceleration of the particle, g_i is the body force acceleration vector (e.g., gravitational loading), M_3 is the out-of-balance moment in z coordinate directions, $\dot{\omega}_3$ is the angular acceleration in z coordinate directions, I is the rotational inertia of the particle.

The computation in DEM follows a cyclical process between the application of Newton's second law of motion on each particle and a force-displacement law for contacts between balls, as shown in Figure 2-14. Several force-displacement laws are employed for contact modelling, including the linear contact bond, linear parallel bond, smooth joint, and flat joint models. These models utilize the concept of bonding, where shear and/or tensile forces may develop as a result of relative motion between particles. Additionally, the Hertz and hysteretic contact models are widely used to simulate impact interactions. The Hertz contact model is composed of a nonlinear formulation based on an approximation of the Mindlin and Deresiewicz theory. The hysteretic contact model combines the elastic component of the Hertz model with an additional dashpot group that includes a nonlinear viscoelastic element acting in the normal direction.

Contact forces are computed by tracking the particles within a designated measurement circle. The displacements of the particles are determined by applying a constant velocity and monitoring their trajectories. At the start of each computational cycle, the initial positions of the particles are known. Subsequently, a force-displacement law is applied to each contact bond to calculate the corresponding contact forces. These contact forces are then incorporated into the equations of motion, which allow for the calculation and updating of particle positions using the central finite difference method.

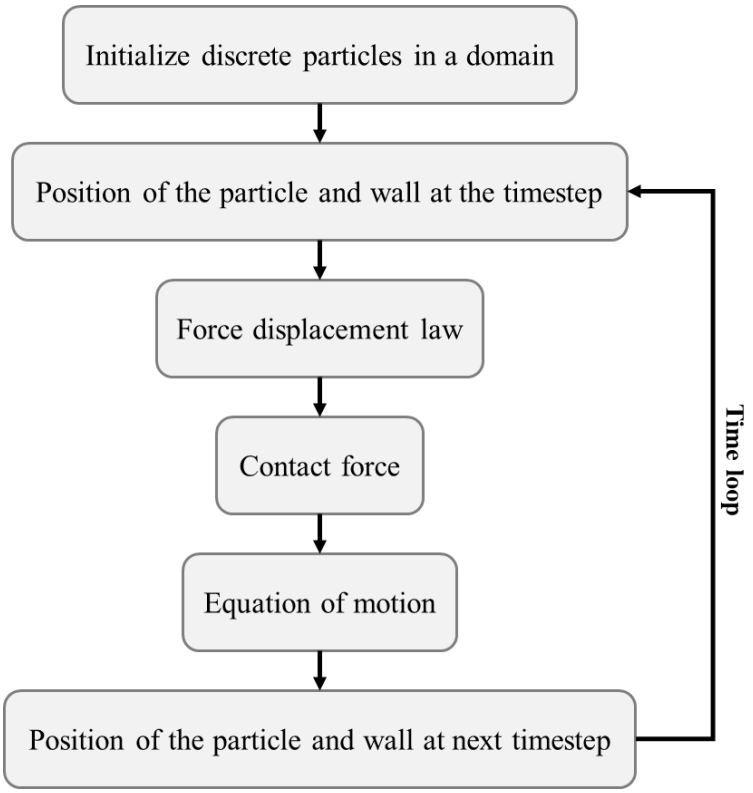

Figure 2-14. Calculation cycle of the DEM model.

DEM is highly effective for simulating granular materials and discontinuous systems by modelling the behaviour of individual particles. It offers valuable insights into complex phenomena such as flow, breakage, and deformation that are often difficult to simulate by traditional continuum approaches. Therefore, DEM has been increasingly utilized to study the failure mechanisms across various engineering research fields, including metal, composite, and joining. Mohebkhah presented a two-dimensional numerical model based on the specialized DEM for the nonlinear static analysis of masonry-infilled steel frames with openings under in-plane monotonic loading. The model effectively predicts the collapse load, joint cracking patterns, and potential failure modes of masonry-infilled steel frames, considering the location and relative size of the openings [154]. Maheo introduced a three-dimensional numerical model employing the DEM to simulate damage in unidirectional composite materials. The model effectively captures local degradation mechanisms, including matrix micro-

fissuring, fibre/matrix debonding, and fibre fracture. Simulations of tensile and shear loading exhibit strong agreement with existing literature, demonstrating the capability of DEM to accurately predict crack propagation paths in composite [155]. Yu developed a three-dimensional DEM model to simulate the strength and damage propagation of carbon fibre reinforced polymer (GFRP) plates and bolted lap joints under axial tension. As illustrated in Figure 2-15, the model calibrated with experimental data, accurately predicts the failure loads and modes, showcasing the advantages of DEM in capturing microscale crack propagation over traditional FEM [156].

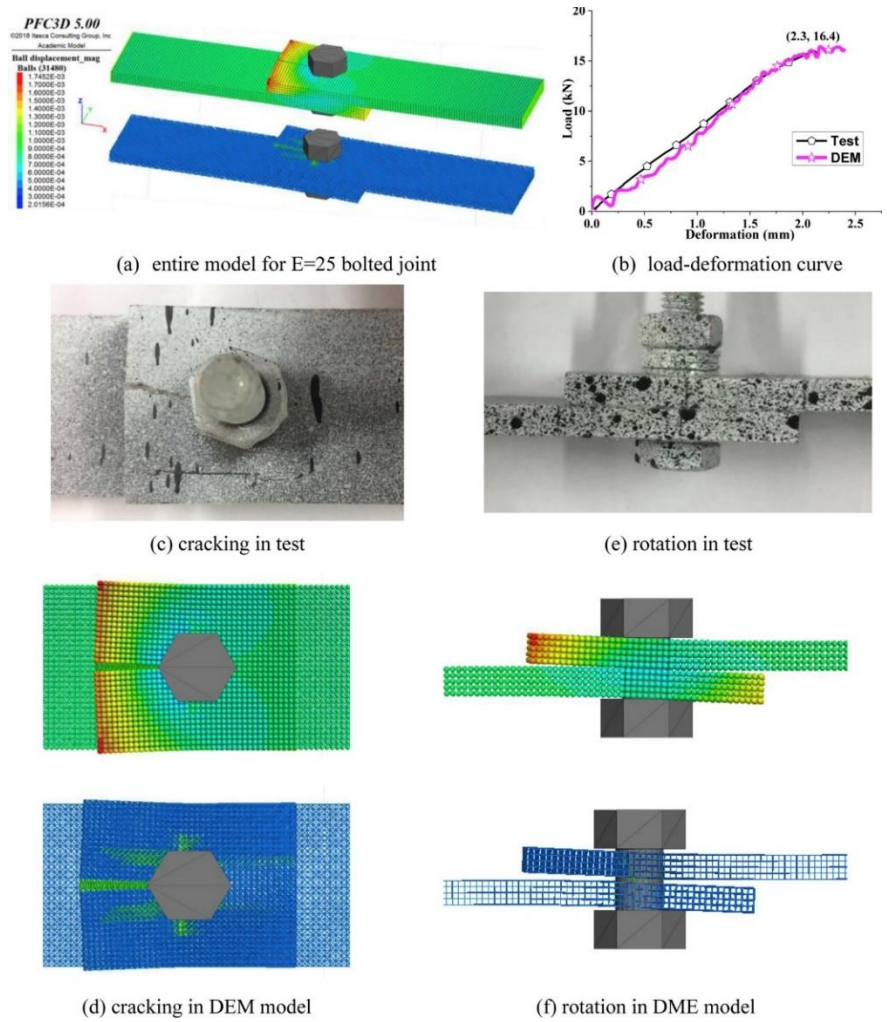

Figure 2-15. Comparison between the numerical and experimental results of bolted lap joints [156].

There are two main approaches for the calibration of the input parameters in DEM [157]. The first approach for the calibration of the parameters in DEM models is called the bulk calibration approach, which aims to numerically reproduce the original experimental setup and procedures as closely as possible. In this calibration approach, DEM parameters are iteratively modified until the simulated bulk behaviour aligns with the experimentally results. A potential drawback of this method is that there can be more than one set of parameters reproducing the similar simulated bulk behaviour. The second approach is called the direct measuring approach, which determines the parameter by directly measuring the properties at the particle or contact level. This approach can only obtain reliable results if the particle shape and size are reasonably well represented, and if the contact model adequately reflects the actual physical contact behaviour [158].

Although the calibration of DEM parameters is a time-consuming process, a machine learning (ML) based approach can be developed to significantly improve the efficiency. Gu proposed a novel three-dimensional DEM for simulating anisotropic composite materials by fully capturing particle-level interactions. To address the challenge of calibrating the microscale bond parameters, this study integrates a ML approach with a genetic algorithm, enabling efficient and accurate identification of bond properties [159]. Shentu developed an end-to-end ML framework to efficiently calibrate complex DEM models. The framework is composed of two stages: the first stage predicts the strength of a single-phase geomaterial, while the second stage focuses on estimating the overall strength of a multi-phase geomaterial sample [160].

DEM is a discontinuous method capable of simulating particle interactions and discrete fracture processes. Therefore, an increasing number of studies have employed the DEM to investigate the failure mechanisms of joints, due to its flexibility and

robustness in accurately simulating the microstructure and capturing mixed failure modes at both the macroscopic and microscopic scales.

Wang used the bulk calibration approach combined with the genetic expression programming modelling and symbolic regression model to determine the microparameters for the soft bonds of the brittle and ductile adhesive in DEM, as illustrated in Figure 2-16a and Figure 2-16b. Through the validation of experiments such as DCB, ENF, and SLJ shear tests, the developed models can effectively predict the micromechanical behaviours of the adhesives under different loading conditions, including the mixed-mode failure [161, 162]. Furthermore, the micromechanical response and failure mechanism of the Al-Al, PPA-PPA and hybrid SLJs are analysed using the developed DEM models, as illustrated in Figure 2-16c. The study reveals that the rotation angle of the joints affects the normal stress at the interfaces, which subsequently influences the mixed-mode behaviour and joint strength when using adherends with varying stiffness [163].

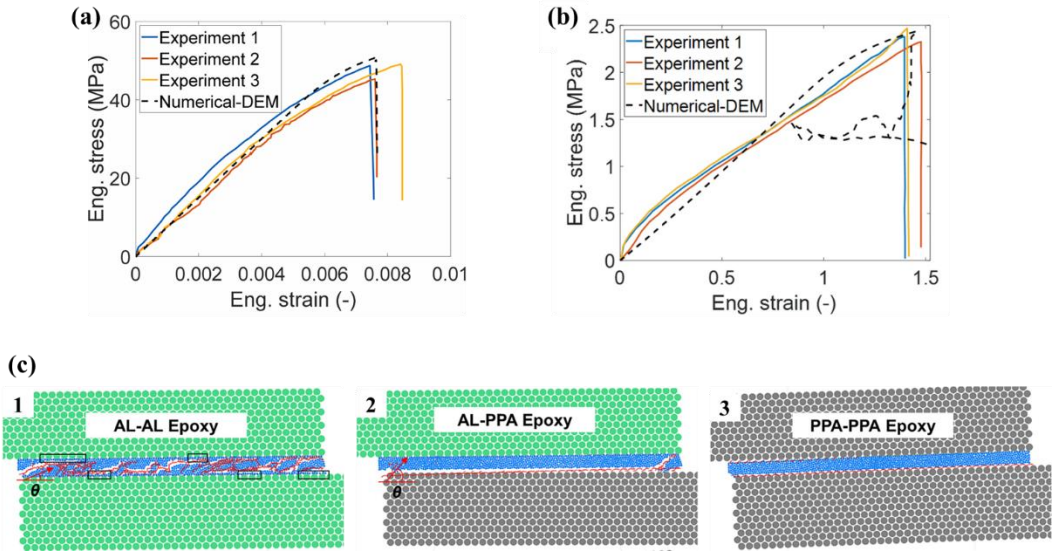

Figure 2-16. Comparison between the numerical and experimental results of SLJs [161-163]. (a) Brittle adhesive. (b) Ductile adhesive. (c) Failure modes.

Xue conducted both experimental and numerical investigations on bolted GFRP joints under uniaxial tension and various thermal conditions (−20°C, 20°C, and 60°C). The developed DEM models are capable of predicting not only the properties of the joints but also the failure modes, including detailed meso/micro-level damage, which are consistent with the experimental observations [164]. Due to the advantages of DEM in modelling the initiation and propagation of microcracks, Kanani developed DEM models to estimate the failure load and crack path in the adhesive bond line of joints. The failure load and crack path predicted by the DEM model shows close agreement with both experimental and FEM results [165].

2.4.2.3. Comparison of FEM and DEM

For the numerical analysis of adhesive joints, FEM treats the adhesive layer and adherends as continuum media, allowing accurate representation of stress and strain distributions, cohesive failure, and material nonlinearity. However, FEM faces challenges in accurately replicating microstructures and micromechanical behaviors [166, 167]. For example, the sinusoidal functions to represent the non-flat interface is utilized and the spatial heterogeneity of adhesion is used instead of considering the microroughness [168]. Defects are typically introduced in the models by selectively removing elements from the adhesive layer at macroscale [154, 169].

CDM, CZM and XFEM are widely used in FEM to study the fracture analysis of adhesive joints. However, each method has limitations. CZM can only simulate damage along a predefined crack path using macroscopic parameters, which cannot capture the real fracture initiation and propagation at microscale [170]. XFEM is also directly based on macroscopic parameters and cannot search for failure points along the interface [171]. CDM cannot properly capture discrete matrix cracks, shows strong

mesh-dependence in crack path prediction, and lacks direct control over crack propagation along material features [172]. Therefore, these methods are not particularly suitable to describe mixed model failure for adhesive joints.

In contrast to FEM, which is constrained by significant element distortion and frequent re-meshing [173], DEM does not encounter these limitations. Due to its discontinuous nature, DEM has the potential to overcome the challenges typically encountered in FEM when modelling microstructure replication and fracture simulation of mixed-mode failure at the microscale. Nevertheless, the calibration of DEM parameters can be a time-consuming process. Additionally, DEM has the potential to induce localized stress concentrations or uneven stress distributions, as stress and strain calculations are based on local contacts and particle interactions.

Considering the flexibility and robustness of DEM in reproducing the microstructure feature and capturing the mixed mode failure, this study utilizes DEM to explore the effect of microstructural features on the performance and microscale fracture mechanisms of SLJs.

2.5 Conclusion

This chapter presents a review of the current state of research on adhesive joints. The review begins with an investigation into the configuration, hybrid joining techniques, and failure modes of adhesive joints. Subsequently, the effects of joint geometry, material properties, adhesion interface, and environmental factors on the performance and failure mechanisms of adhesive joints are reviewed. However, there is not a well-received agreement regarding the effect of microstructural features such as microstructural surface roughness and microstructural defect. Investigating these effects at the microscale can offer a more detailed understanding of localized behaviours,

such as crack initiation and propagation, which are crucial for accurately predicting the overall performance and failure modes of adhesive joints. Finally, the analysis methods for adhesive joints are discussed, covering both analytical and numerical approaches. As adhesive joint designs become more complex, analytical methods are difficult to provide accurate predictions. In contrast, numerical methods can effectively model complex geometries and material behaviours without relying on simplifying assumptions. While FEM can be limited in simulating the fracture process of adhesive joints, particularly under mixed failure modes, DEM demonstrates an ability to model complex fracture behaviour, especially in tracking crack initiation, coalescence, and propagation.

Chapter 3

3 Experiment work

3.1 Introduction

This chapter presents the experimental study for determining the mechanical properties of adherends, adhesive, and multi-type SLJs used in this research, as well as for analyzing the microstructural surface roughness and internal defects within SLJs. The adherends used in this study are 6082-T6 aluminum alloy and 50% glass fiber-reinforced PPA plates (Grivory HTV-5H1 Black 9205), while the adhesive employed is Loctite EA 9497. The adherend materials and adhesive are selected based on a real-world lightweight design for the automotive industry. Mechanical properties are obtained through tensile tests following international standards: ISO EN 485-2:2004 for adherends, ISO 527-2:2012 for epoxy adhesives, and BS ISO 4587:2003 for SLJs. The non-contact optical measurement system and mechanical extensometer are utilized to measure the displacement and strain.

Experimental methodologies for assessing the microstructural surface roughness of adherend and microstructural defects within bonding overlap of SLJ are systematically presented in this chapter. A grinding machine is employed for the surface treatment of adherends to achieve three roughness grades. A non-contact laser microscope is used to characterize microroughness profiles, with surface roughness measurements conducted in accordance with international standards, including ISO 4288:1996, BS EN ISO 11562:1997, and BS EN ISO 3274:1998. Scanning Electron Microscopy (SEM) is employed to analyze the microstructural roughness of the adhesion surface and detect defects within the bonding region. Furthermore, Computed

Tomography (CT) scanning is conducted to further examine microstructural defects in the bonding region.

3.2 Bulk properties of adhesive

Epoxy adhesives are well known for their high strength, durability, and versatility, as well as their exceptional resistance to aggressive environments. Loctite EA 9497 is a general-purpose adhesive designed for bonding a wide variety of materials. It is a two-part structural epoxy adhesive mixed using a dual cartridge applicator gun. This medium-viscosity, room-temperature-curing adhesive is well-suited for heat dissipation applications and high compression strength applications.

To obtain the bulk properties of Loctite EA 9497, the standard adhesive specimen is designed based on ISO 527-2:2012. Figure 3-1a illustrates the geometry configuration of the adhesive specimen. The epoxy adhesive is applied using a gun fitted with a nozzle and then manually spread evenly within dog-bone-shaped cavities of a 60-shore silicone mould. The adhesive is left to cure at room temperature for seven days, as shown in Figure 3-1b. The adhesive specimen features an overall length of 160 mm, with a gauge length of 50 mm and a wide gauge section of 10 mm. The ends measure 20 mm in width, while the thickness is 6 mm, as indicated in the A-A cross-sectional view. The transition between the gauge section and the wider ends incorporates a 60 mm fillet radius, designed to minimize stress concentrations and ensure uniform stress distribution during mechanical testing. The mechanical test of the adhesive specimen is carried out using Instron 5985 series machine with 250 kN, as shown in Figure 3-1c. The crosshead speed is set to 0.5 mm/min. A mechanical extensometer is employed to measure strain.

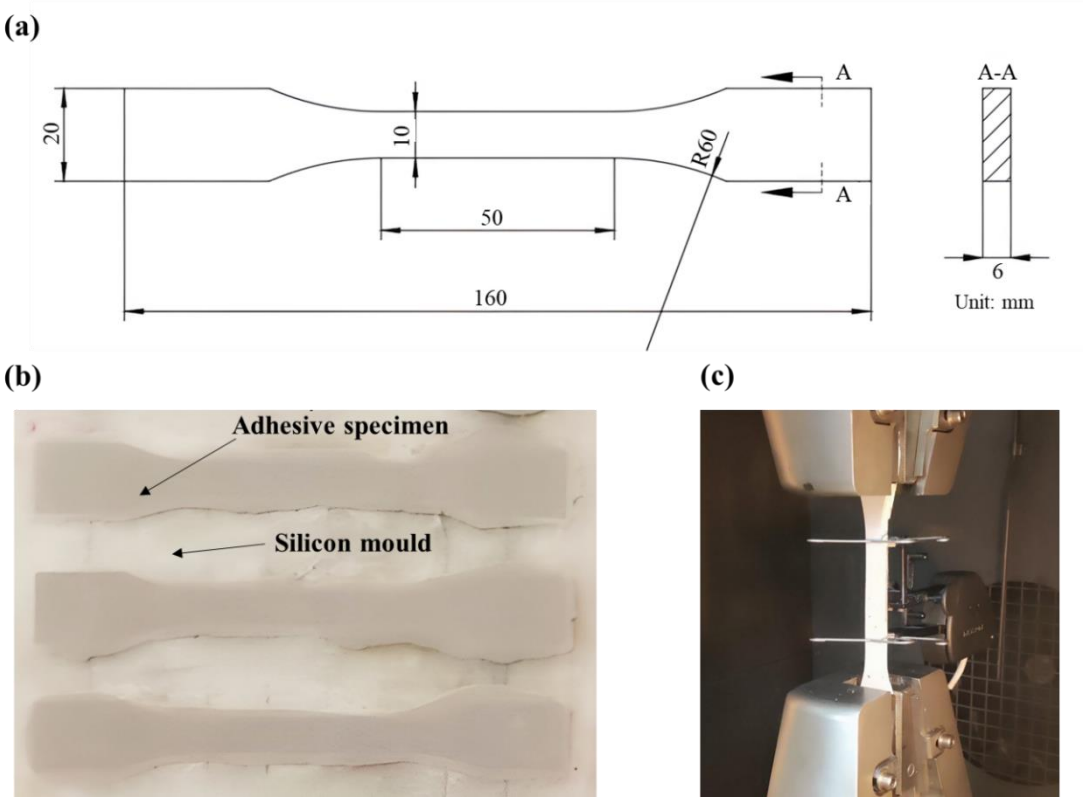

Figure 3-1. Fabrication and test of adhesive specimens. (a) Geometry configuration. (b) Fabrication. (c) Tensile test.

The Young's modulus E of epoxy adhesive is measured within a strain range of 0.05% and 0.25% following the standard EA ISO 527-2: 2012.

Young's modulus $$E = \frac{\Delta\sigma}{\Delta\varepsilon} \tag{3-1}$$

Where $\Delta\sigma$ and $\Delta\varepsilon$ represent the variations in tensile stress and strain, respectively,

Figure 3-2 illustrates the representative stress-strain curves from the tensile test results of Loctite EA 9497. The bulk properties of the tested adhesive specimens are summarized in Table 3-1. The average tensile strength and Young's modulus of the epoxy adhesive is 35.1 MPa and 9645 MPa, respectively. The coefficient of variation for the tensile strength reaches up to 12.0%, which may be attributed to the presence of

uncontrollable defects. The Poisson's ratio of the adhesive is 0.29, based on the manufacturer data.

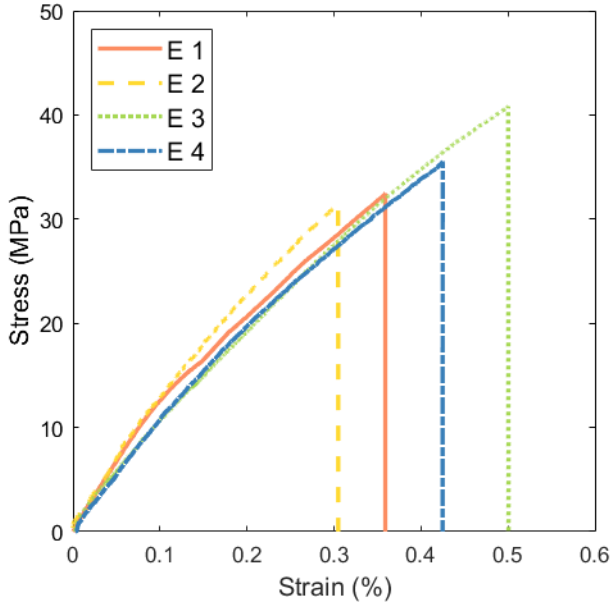

Figure 3-2. Stress-strain curves of tested adhesive specimens.

Table 3-1. The bulk properties of tested adhesive specimens.

ID	Tensile strength (MPa)	Young's modulus (MPa)	Poisson ratio
E 1	32.5	8955	/
E 2	31.4	10396	/
E 3	40.8	9585	/
E 4	35.5	9645	/
E (Average±SD)	35.1±4.2	9645±590	0.29*

*Manufacturer data, SD: Standard deviation.

3.3 Bulk properties of adherends

Two types of adherend samples of dimensions of 100×25×3 mm are cut from 6082 T6 aluminum alloy and 50% glass-fiber-reinforced PPA plates (Grivory HTV-5H1 black 9205). Specifically, the PPA plates are cut to ensure the adherend length is aligned with the fiber direction. Compared to other polyamides, the standout

characteristic of the selected PPA is its good performance at high temperatures, enabling the production of parts that are stiffer, stronger, and exhibiting better heat distortion stability and chemical resistance. The aluminum alloy is provided in bar form with dimensions of 25 mm in width, 5 m in length, and 3 mm in thickness, and is cut to the required size using a hydraulic guillotine. The PPA is supplied by EMS Switzerland in plate form, with dimensions of 100×100×3 mm. The selected adherend materials are based on a real-world lightweight design approach for the automotive industry. The mechanical testing of the adherend specimens is conducted using an Instron 5985 series testing machine with a 250 kN load cell, at a testing speed of 2 mm/min.

Figure 3-3 illustrates the representative stress-strain curves from the tensile test results of Al and PPA adherends. The bulk properties of the tested adherends are summarized in Table 3-2. The average yield stress is 284.4 MPa and 230 MPa for the Al and PPA material, respectively. The yield stress is determined by plotting the stress-strain curve and drawing a line parallel to the initial linear region of the curve, offset by 0.2% strain, until it intersects the stress-strain curve. The Young's modulus is determined over the strain range of 0.05% to 0.25% using Equation 3-1. The average Young's modulus is 70524 MPa and 17642 MPa for the Al and PPA adherend, respectively. The Poisson’s ratio is 0.30±0.03 and 0.32±0.04 for the Al and PPA material, respectively, which refers to the study [174].

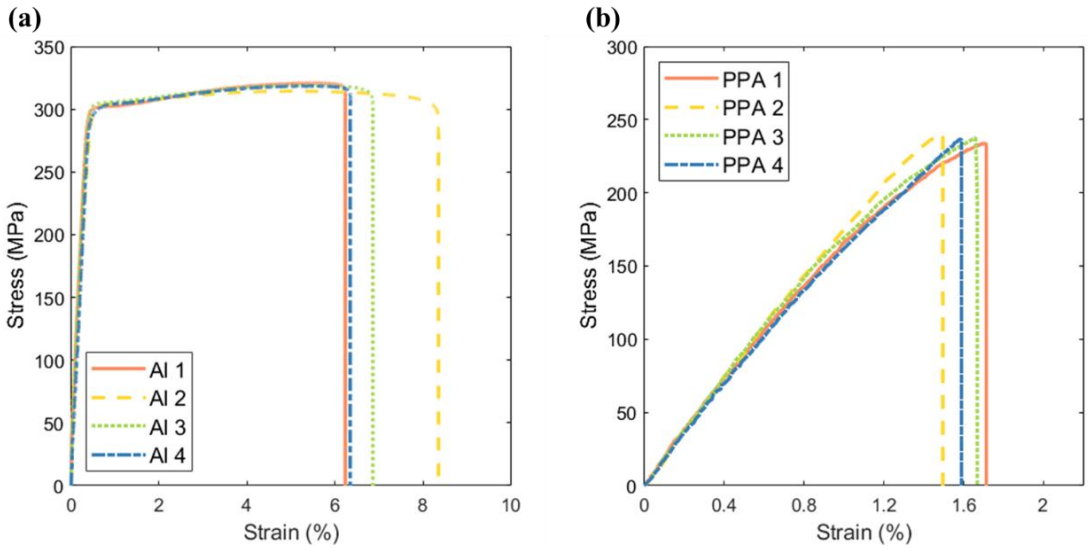

Figure 3-3. Stress-strain curves of tested adherend specimens. (a) Stress-strain curves of Al specimens. (b) Stress-strain curves of PPA specimens.

Table 3-2. The bulk properties of tested adherend specimens

Property	Al (Average±SD)	PPA (Average±SD)
Yield stress (MPa)	284.4±5.6	230.0±6.9
Young's modulus (MPa)	70524±1095	17642±471
Elongation at fracture (%)	7.0±1.0	1.6±0.1
Poisson ratio	0.30±0.03	0.32±0.04

3.4 Fabrication of multi-type SLJs

Three types of SLJs are manufactured for the SLJ shear tests according to international standard BS ISO 4587:2003, which are the Al-Al, PPA-PPA, and hybrid (Al-PPA) SLJs, as shown in Figure 3-4a. Each type of SLJ is subjected to surface treatment (details are provided in Subsection 3.4.1) of the adherends to achieve three surface roughness grades, which are labelled as G1, G2, and G3, respectively, as shown in Table 3-3.

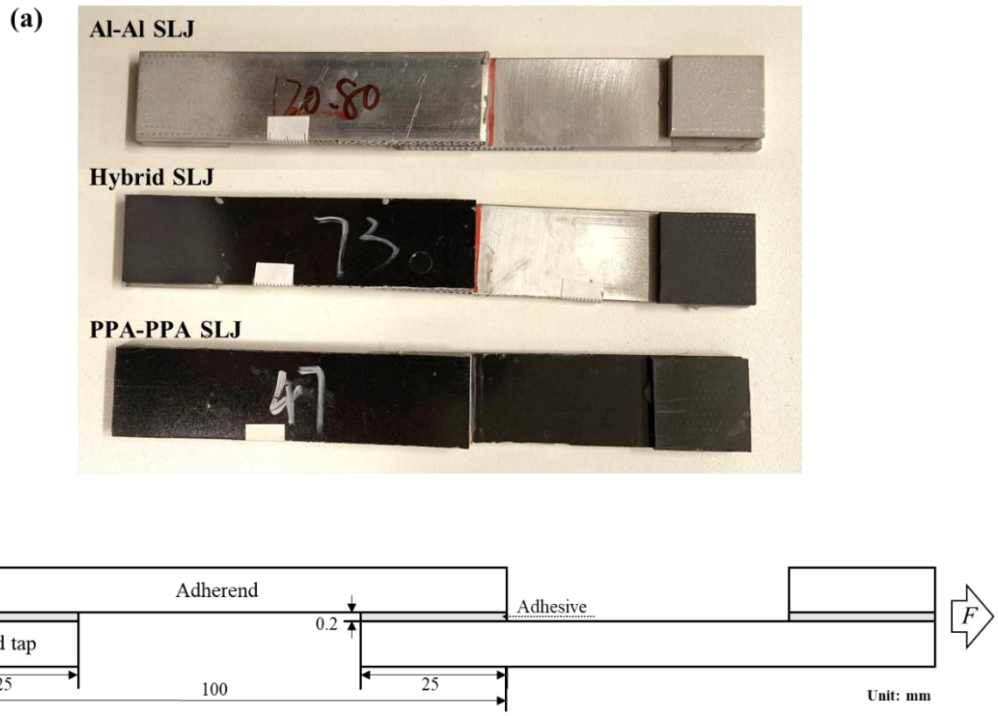

Figure 3-4. SLJ specimens. (a) Three types of SLJs. (b) Geometry configuration of SLJs.

Table 3-3. The categories of multi-type SLJs with different roughness grades.

Type	Subtype	Roughness grade of top adherend	Roughness grade of bottom adherend
Al-Al SLJ	Al-G1	Al grade 1	Al grade 1
	Al-G2	Al grade 2	Al grade 2
	Al-G3	Al grade 3	Al grade 3
PPA-PPA SLJ	PPA-G1	PPA grade 1	PPA grade 1
	PPA-G2	PPA grade 2	PPA grade 2
	PPA-G3	PPA grade 3	PPA grade 3
hybrid SLJ	Hybrid-G1	Al grade 1	PPA grade 1
	Hybrid-G2	Al grade 2	PPA grade 2
	Hybrid-G3	Al grade 3	PPA grade 3

To ensure the optimal adhesive bonding, the surface of all the adherends is cleaned after the grinding process with Acetone and Loctite SF 706 to remove grease

residuals. Six short copper wires, each with a diameter of 0.2 mm and a length of 0.5 mm, are placed on the bonding surface of one adherend to ensure a uniform adhesive layer thickness. These wires lie parallel to the direction of the applied load on the joints. Furthermore, two end tabs are bonded at the two edges of SLJs to mitigate the impact of bending induced by the eccentricity of the applied loading during tests. All SLJs undergo a seven-day curing process at room temperature conditions. The dimensions of all the SLJs are standardized, with a total length of 175 mm and a width of 25 mm. Additional specifications include an overlap length of 25 mm, adherend thickness of 3 mm, and adhesive thickness of 0.2 mm, as illustrated in Figure 3-4b.

3.4.1. Surface treatment

Silicon carbide grinding papers with grit sizes P60, P120, and P2500 are used for the surface treatment of the adherends to obtain three roughness grades. The grinding process for the adherends is carried out using a SAPHIR 330 grinding machine, operated at 100 revolutions per minute. Each specimen is ground for a duration of 2 minutes. Non-contact surface roughness measurement offers several advantages, including non-destructive evaluation, rapid measurement capability, and safe assessment of delicate materials. For high-precision microroughness profiling, the OSL5000 3D laser microscope is employed. This instrument provides exceptional angular detection sensitivity and generates high-contrast images, significantly improving the accuracy of surface characterization.

After the surface treatment of the adherends, the ground and cleaned adherends are positioned on the laser microscope for surface roughness analysis. The measuring process, illustrated in Figure 3-5, is carried out by following international standards, including ISO 4288:1996; BS EN ISO 11562:1997; BS EN ISO 3274:1998. The

roughness of the adherends is determined by calculating the average of the three different scanning areas shown in Figure 3-5.

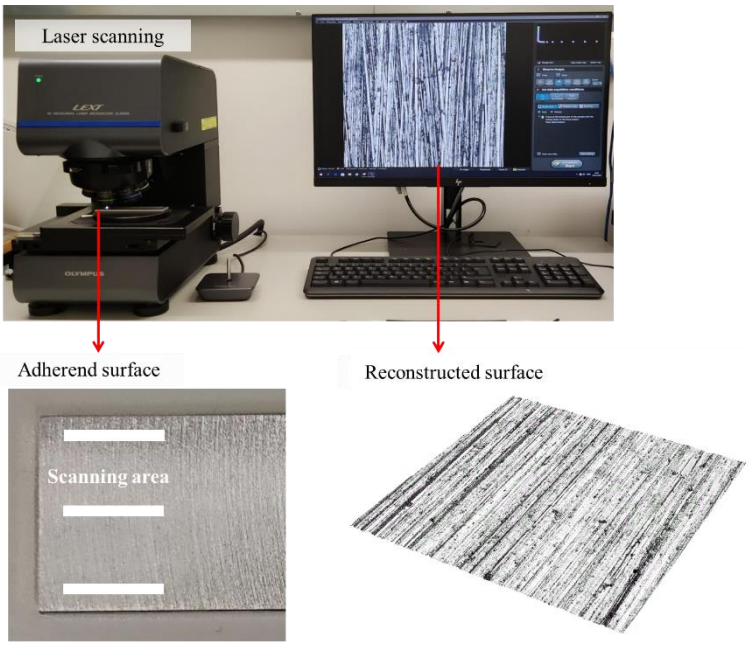

Figure 3-5. Scanning process for the ground adherends.

For roughness measurement, the reconstructed 3D surface profiles of the ground adherends are analyzed, as shown in Figure 3-6. In surface roughness measurement, the selection of sampling length and evaluation length significantly affects the accuracy and representativeness of the results. The sampling length determines the cut-off wavelength for distinguishing roughness from waviness, while the evaluation length is the profile segment used for the calculation of roughness parameters. In this study, the sampling lengths of the filter to separate roughness and waviness are set as 2.5 mm for the adherends ground by the P60 grits, while a value of 0.8 mm for the adherends abrased by the P120 and P2500 grits. The evaluation length is the scanning length of the adherend surface, determined with reference to ISO 4288:1996. The roughness grades and the detailed parameters of the ground Al and PPA adherends are shown in Table 3-4.

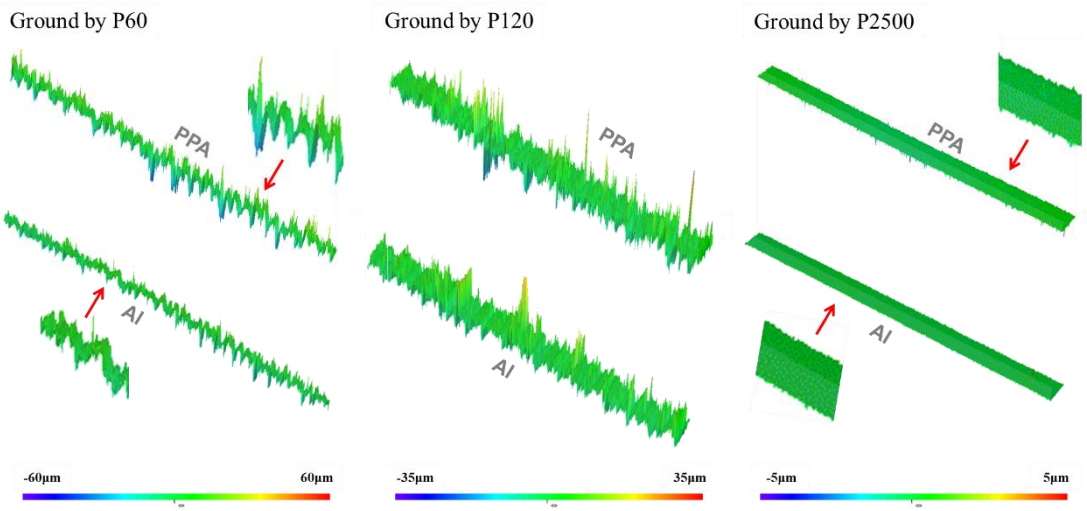

Figure 3-6. Roughness measurement of the reconstructed 3D surface profiles.

Table 3-4. The characteristics of surface roughness for the ground adherends.

Roughness grade	**Grit size**	**Al-R_a (μm)**	**PPA-R_a (μm)**	**Sampling length (mm)**	**Evaluation length (mm)**
1	P2500	< 0.204	< 0.223	0.8	4
2	P120	1.902±0.127	2.133±0.132	0.8	4
3	P60	4.045±0.255	7.048±0.536	2.5	12.5

3.4.2. Microstructure analysis

Following the fabrication of the SLJs, the overlap area of representative SLJs undergoes cutting, grinding, and polishing processes for SEM measurements and CT scanning to study microstructural interfaces and defects. Both SEM and CT scanning are widely employed techniques for microstructural analysis of materials. SEM is particularly well-suited for high-resolution imaging of surface morphology and detailed elemental composition, making it highly effective for surface-level investigations. CT scanning provides comprehensive 3D visualization of the internal structure of materials,

facilitating the analysis of features such as porosity, cracks, and voids in a fully non-destructive manner.

The samples for SEM imaging are coated with gold, which are scanned using JEOL JSM-7800F with the parameter settings shown in Table 3-5. The samples for CT scanning are scanned using Heliscan micoCT with the parameter settings shown in Table 3-6.

Table 3-5. Parameter setting of SEM scanning.

Detector type	Accelerating voltage	Gun voltage	Emission current	Working distance	Vacuum pressure	Magnification
LED	5 kV	5 kV	101.4 μA	19.36 mm	1.91×10^{-4} Pa	500×

Table 3-6. Parameter setting of CT scanning.

Trajectory	Projection per revolution	Tube voltage	Tube current	Exposure time	Voxel size
Space filling	1800	80 kV	140 μA	2.4 s	3.259 μm

3.4.2.1. Microstructural interface

SEM scanning is used to analyze the microstructural interfaces of Al and PPA adherends. Each block specimen for scanning has dimensions ranging from 5 mm to 6 mm in length, width, and height. Figure 3-7 is the scanned adhesion interfaces between the adhesive and adherend, featuring the three roughness grades, which highlights the robust bonding between the adhesive and adherend. As the surface roughness of the substrate increases, the interface between the adhesive and the adherend undergoes significant physical changes. Rougher surfaces exhibit more pits and protrusions, which

enlarge the contact area between the adherend and adhesive, facilitate the penetration of adhesive and form stronger mechanical interlockings. Additionally, the highlighted areas on the adhesive can be attributed to the Al powder, since the specimen surfaces for SEM observation are ground and polished.

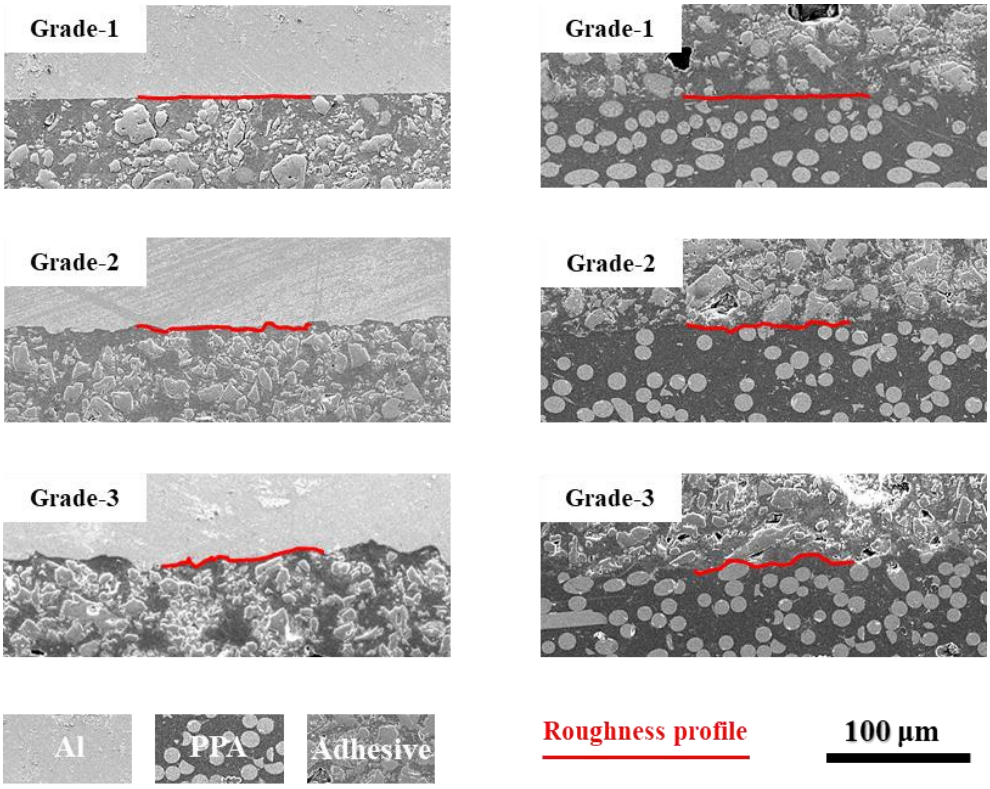

Figure 3-7. The adhesion interfaces scanned by SEM.

3.4.2.2. Microstructural defect

To detect the defects in the SLJs, both SEM and CT scanning are used. As illustrated in Figure 3-8a, the block specimens are assembled through layered bonding for the CT scanning. Each block specimen has dimensions ranging from 4.5 mm to 5 mm in length, width, and height (Figure 3-8b).

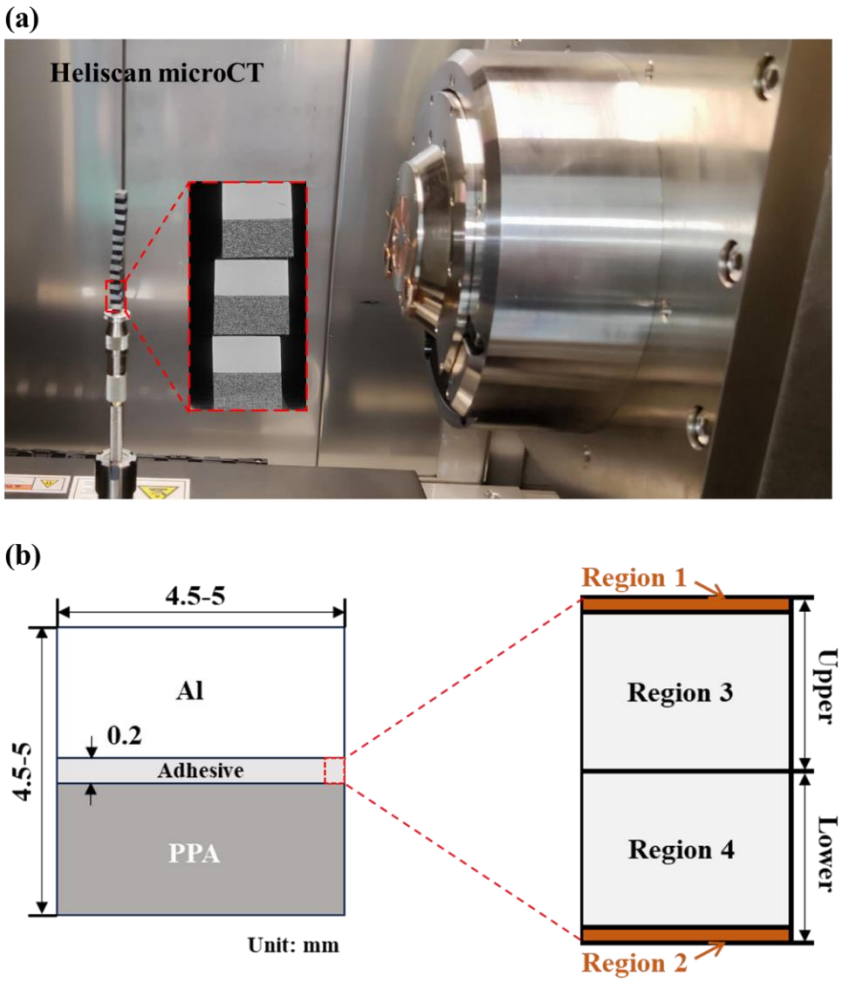

Figure 3-8. Defect detection. (a) CT scanning setup. (b) Detection regions.

In this study, the analysis focuses on two types of microstructural defects: the interfacial defects (defects on the adhesion interface) and adhesive defects (defects within the adhesive layer). As illustrated by the specimen in Figure 3-8b, the scanned adhesive layer is divided into four regions. Regions 1 and 3 are adjacent to the Al adherend (upper layer), while Regions 2 and 4 are adjacent to the PPA adherend (lower layer). The average equivalent diameters of the defects adjacent to each adherend are determined based on the defects in the upper layer and the lower layer of the adhesive, respectively. The equivalent diameter is the diameter of an equivalent sphere that has a volume equal to the irregularly shaped defect, which is reconstructed based on the CT scanning. To analyze the interfacial defects on the Al and PPA adhesion interfaces,

Regions 1 and 2 are specially designated. The thicknesses of Regions 1 and 2 are determined based on the calculated equivalent diameters of the defects, which are 19.98 μm and 20.10 μm, respectively. These two values enable the analysis of the entire interfacial defect adjacent to adherends. Additionally, Regions 3 and 4 are designated for analyzing the adhesive defects adjacent to the Al and PPA adherends, respectively.

The raw data acquired from CT scanning is reconstructed using Avizo software. Figure 3-9a shows the cross-sectional view of the overlap identified by the CT scanning. It demonstrates the presence of microstructural defects of various sizes and shapes distributed within the adhesive layer and on the adhesion interfaces. Similar results are also observed in the SEM images, as shown in Figure 3-9b. Both techniques identify two common types of defects: interfacial defects, which appear along the adhesion interfaces, and adhesive defects, which are embedded within the adhesive layer.

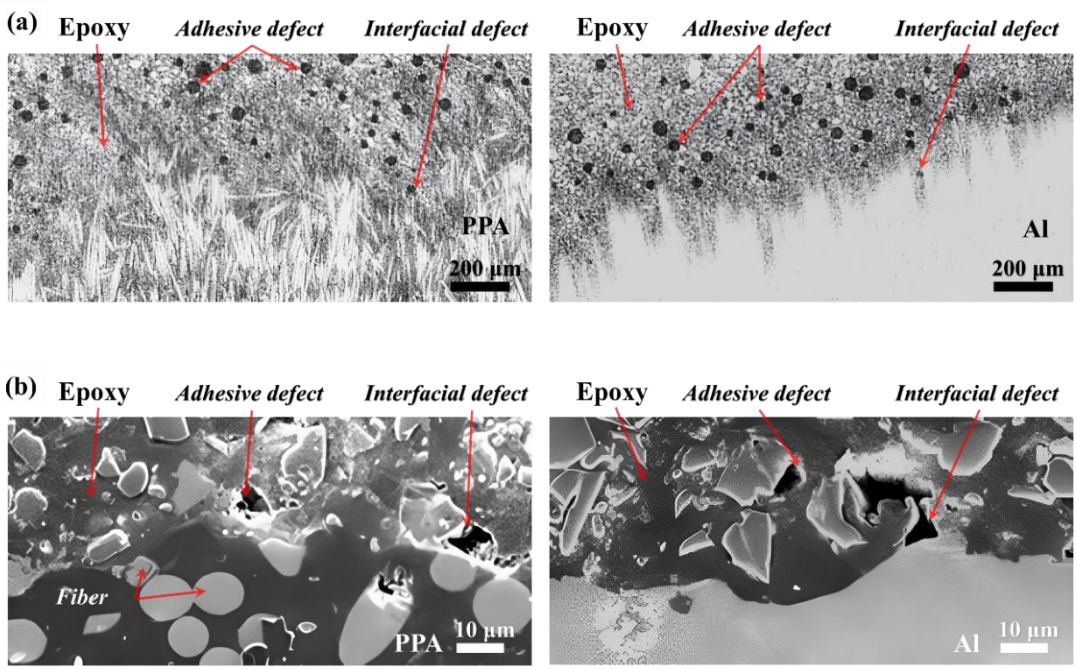

Figure 3-9. Microstructural defects. (a) CT image. (b) SEM image.

CT scanning can introduce measurement errors due to resolution limitation, potentially impacting the accuracy of defect statistics. However, considering the

precision of the existing measurement methods, these errors are anticipated to be negligible. The statistical analysis of microstructural defects is conducted on the four specific regions, as depicted in Figure 3-8. A representation of the reconstructed defect profiles is illustrated in Figure 3-10. It shows that the irregularly shaped defects with a wide range of sizes, ranging from a few tenths of a micrometer to several hundred micrometers, are discretely distributed within the adhesive layer.

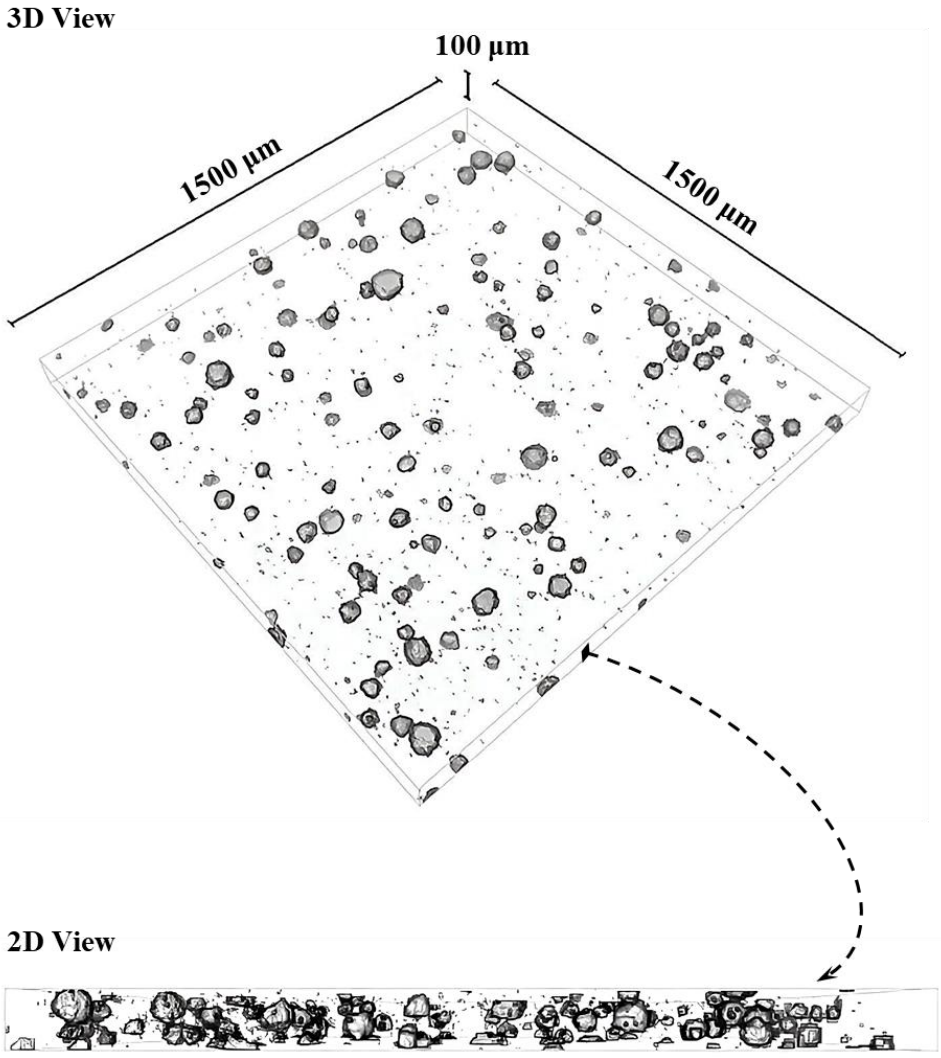

Figure 3-10. Image reconstruction of CT scanning.

The defect volume ratios across the four regions and average equivalent radius of defects are summarized in Table 3-7 based on the results of 18 samples. The defect

volume ratio is defined as the proportion of the total adhesive volume occupied by the reconstructed defects. It is observed that the average equivalent radius of microstructural defects adjacent to different adherends remains nearly the same, as the difference is 0.6%. The defect volume ratio adjacent to the PPA adherend increases 6.8%, compared to that of the Al adherend. Defects are more likely to occur within the adhesive layer than those at the interface, since the defect volume ratios of the adhesive layer are significantly higher than that of the interfaces, with a difference of 113.7% for the Al adherend and 59.6% for the PPA adherend. Additionally, the defect volume ratio at the PPA interface is 43.1% higher than that at the Al interface (1.02%). This difference can be attributed to the inferior wettability of the epoxy adhesive on PPA compared to Al, resulting from the lower surface energy of PPA.

It should be noted that the defect volume ratio obtained in this study is relatively low compared with the levels typically of concern in industrial applications. This relatively small value may be attributed to the limited statistical sampling numbers and sizes used in the micro-CT analysis. Nevertheless, it provides a representative description of high-quality bonding conditions and allows for a clear examination of the micromechanical effects of defects on joint behaviour.

Table 3-7. The statistic data of the reconstructed defects.

Region	**Defect volume ratio (Mean±SD %)**	**Average equivalent radius (Mean±SD μm)**
Region 1	1.02±0.64	9.99±5.10
Region 2	1.46±1.01	10.05±6.73
Region 3	2.18±0.82	9.99±5.10
Region 4	2.33±0.85	10.05±6.73

3.5 SLJ shear test

The SLJ shear tests are conducted using Instron 3382 equipped with a 100 kN load cell. A loading speed of 0.3 mm/min is applied to the clamped edge for the test. Imetrum, serving as a non-contact optical measurement system, is employed for recording the testing process and deformation data. The overlap area of all the testing specimens is marked with black dots for tracking and recording the movement of the designated positions by the measurement system, and a paper ruler is attached to the SLJ for calibrating the dimension. The displacements of the joints are collected by the measurement system and further calculated from the vertical displacement difference between the red points 1 and 2. The testing setup and process of SLJ shear test are shown in Figure 3-11.

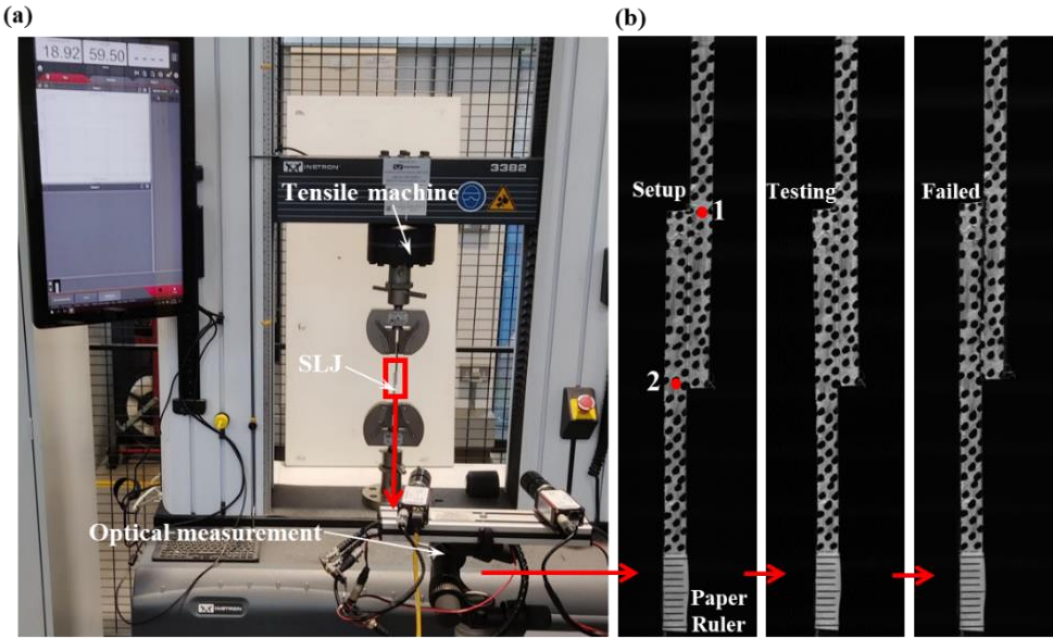

Figure 3-11. SLJ shear test. (a) Testing setup. (b) Testing process recorded by measurement system.

3.5.1. Experimental result of Al-Al SLJs

Five specimens for each roughness grade of the Al-Al SLJs are tested until they fail. The representative load-displacement curves tested from the Al-Al SLJs with three roughness grades are illustrated in Figure 3-12. It is observed that the strength and stiffness of the Al-Al SLJs increase with higher roughness grades. The average maximum failure load and stiffness of Al-G1 are 2990 N and 49126 N/mm, respectively, as presented in Figure 3-12a and Table 3-8. The stiffness is determined by performing a linear fit on the linear elastic response of the load-displacement curves. In comparison to the Al-G1, the average maximum failure loads of the Al-G2 and the Al-G3 are improved by 18.7% and 29.3%, respectively, while the average stiffnesses of the Al-G2 and the Al-G3 increase 4.6% and 10.5%, respectively.

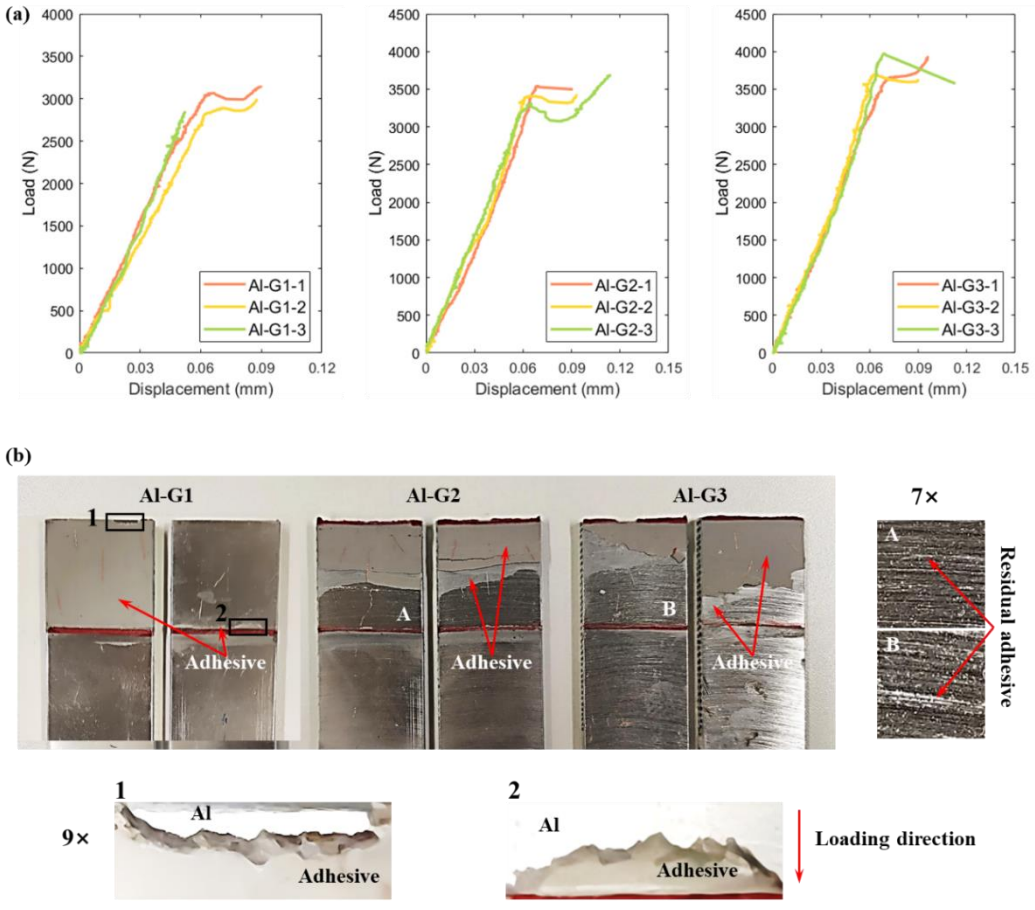

Figure 3-12. Load-displacement curves and failed samples of Al-Al SLJs. (a) Load-displacement curves. (b) Failed samples.

Table 3-8. Mechanical Properties of tested Al-Al SLJs.

ID	Max failure load (N)	Stiffness (N/mm)
Al-G1-1	3140	50496
Al-G1-2	2987	44656
Al-G1-3	2844	52226
Al-G1 (Average±SD)	2990±148	49126±3967
Al-G2-1	3542	49084
Al-G2-2	3423	51702
Al-G2-3	3684	53427
Al-G2 (Average±SD)	3550±131	51404±2187
Al-G3-1	3697	56405
Al-G3-2	3927	52406
Al-G3-3	3974	53993
Al-G3 (Average±SD)	3866±148	54268±2014

Figure 3-12b presents failure modes observed in the failed representative Al-Al SLJ. The areas A and B in Figure 3-12b represent the seven-time magnification views of the selected regions of the Al adherends. The Al-G1 presents a single-sided delamination of the joint, while the double-sided delamination occurs in the Al-G2 and the Al-G3. The failure mode of all the Al-Al joints is mixed-mode involving both adhesive and cohesive failure. It demonstrates that the primary cracks mainly propagate along the interface while simultaneously displaying some cracks propagating into the adhesive. As a result, a certain number of thin adhesive layers remain in some local regions on the surface of the debonded Al adherends.

The observation of residual adhesive on the debonded Al surface is validated by the results of SEM scanning. As shown in Figure 3-13a, the SEM image shows that a large number of microscopic protrusions are presented on the surface of the Al adherend from the Al-G3. Then Energy Dispersive X-ray Spectroscopy (EDS) is conducted in the region shown in Figure 3-13a. The EDS images and spectral analysis reveal the

presence of a significant amount of adhesive on the Al surface, particularly in the areas existing microscopic protrusions. As shown in Figure 3-13b, the majority of the surface areas exhibit an Al spectrum, whereas certain localized regions do not. Furthermore, as shown in Figure 3-13c, these regions are identified as having a C spectrum instead of Al. Additionally, the spectral analysis of two points is conducted on the microscopic protrusions illustrated in Figure 3-13a. The results show a significant presence of C, with intensity levels exceeding 30 counts per second per electron volt, as shown in Figure 3-13d.

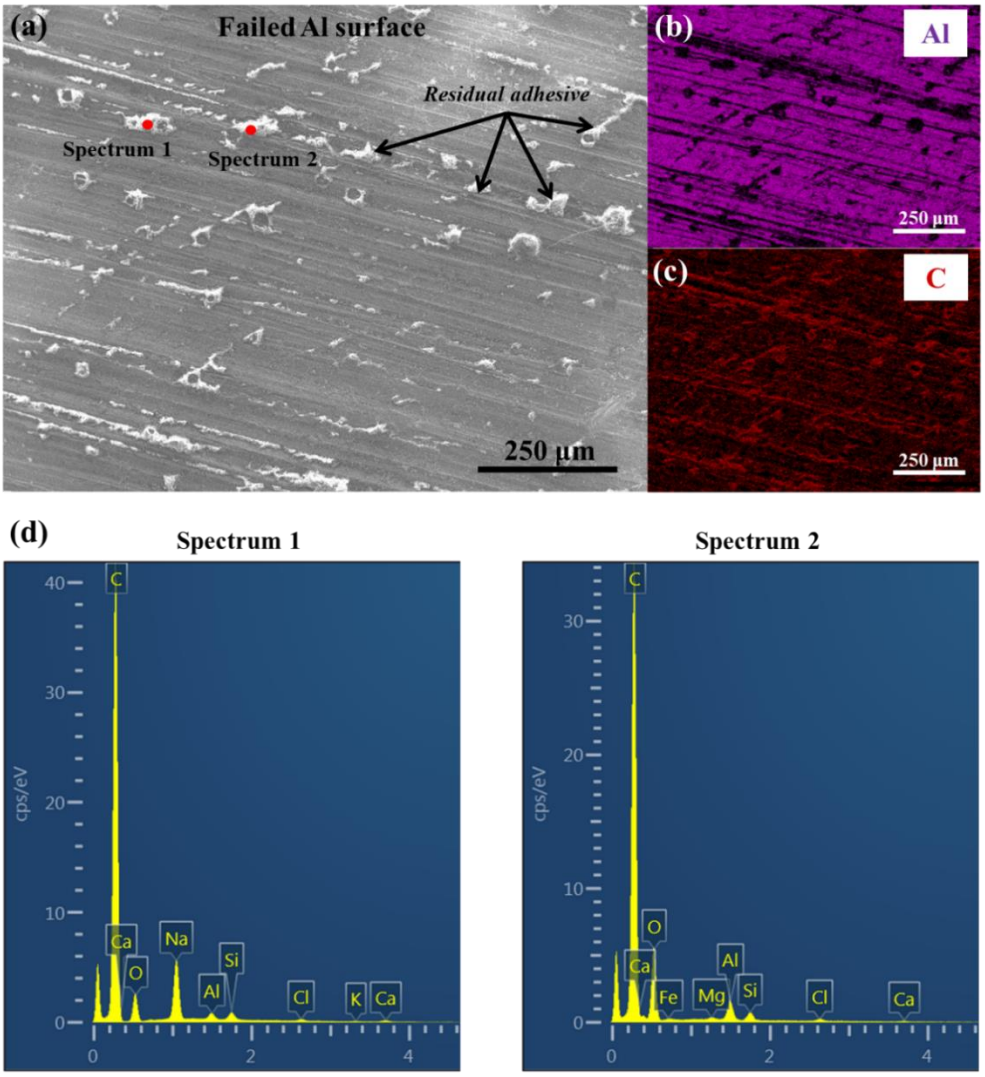

Figure 3-13. Microscopic and analysis images for the adhesion interface of the failed Al-G3. (a) SEM image. (b) EDS-Al layered image. (c) EDS-C layered image. (d) Spectral analysis.

Additionally, there is some obvious cohesive failure in the Al-Al SLJ occurring in the immediate vicinity of the end of the overlap, as shown in areas 1 and 2 of Figure 3-12b. The fracture surfaces of the adhesives exhibiting cohesive failure show irregular morphologies. It is noted that these fracture surfaces form diagonal angles relative to the Al adherend along the loading direction. The maximum length of the residual adhesives on the surface of the debonded Al adherend from Al-G1, measured along the loading direction, is up to 1.47 mm (Figure 3-12b.2).

3.5.2. Experimental result of PPA-PPA SLJs

Five specimens for each roughness grade of the PPA-PPA SLJs are tested until they fail. The representative load-displacement curves tested from the PPA-PPA SLJs with three roughness grades are illustrated in Figure 3-14. It is observed that the strength and stiffness of the PPA-PPA SLJs increase with higher roughness grades, consistent with findings from the Al-Al SLJs. As illustrated in Figure 3-14a and Table 3-9, the average maximum failure load and stiffness of PPA-G1 are 1200 N and 10168 N/mm, respectively. In comparison to the PPA-G1, the average maximum failure loads of the PPA-G2 and the PPA-G3 are improved by 37.2% and 64.8%, respectively, while the average stiffnesses of the PPA-G2 and the PPA-G3 increase 23.5% and 23.8%, respectively.

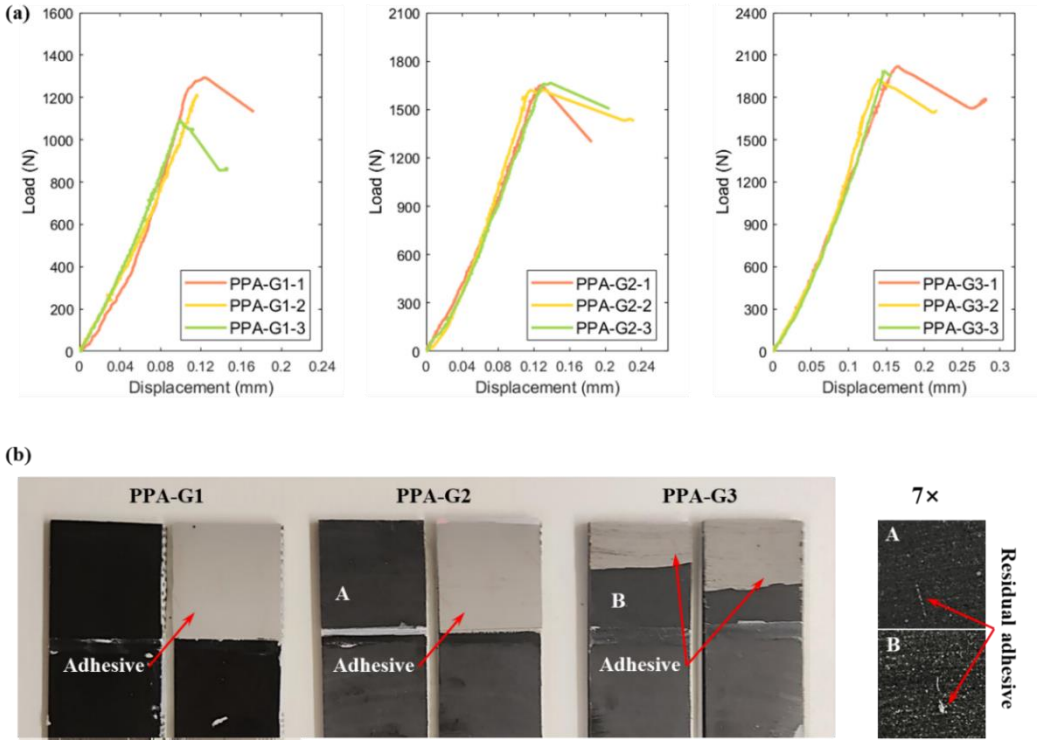

Figure 3-14. Load-displacement curves and failed samples of PPA-PPA SLJs. (a) Load-displacement curves. (b) Failed samples.

Table 3-9. Mechanical Properties of tested PPA-PPA SLJs.

ID	Max failure load (N)	Stiffness (N/mm)
PPA-G1-1	1293	10342
PPA-G1-2	1215	9818
PPA-G1-3	1091	10343
PPA-G1 (Average±SD)	1200±102	10168±303
PPA-G2-1	1652	12454
PPA-G2-2	1622	13112
PPA-G2-3	1664	12110
PPA-G2 (Average±SD)	1646±22	12559±509
PPA-G3-1	2019	12251
PPA-G3-2	1926	13089
PPA-G3-3	1986	12437
PPA-G3 (Average±SD)	1977±47	12592±440

Figure 3-14b presents failure modes observed in the failed representative PPA-PPA SLJs. The areas A and B in Figure 3-14b represent the seven-time magnification views of the selected regions of the PPA adherends. The PPA-G1 and the PPA-G2 present a single-sided delamination of the joint, while the double-sided delamination occurs in the PPA-G3. The PPA-G1 experiences pure adhesive failure along the adhesion interface. The PPA-G2 and the PPA-G3 show predominant adhesive failure with additional localized cohesive failure, resulting in a small number of residual adhesives attached to some local regions on the surface of the debonded PPA adherends. It is observed that the PPA-PPA SLJs with a higher roughness grade of the adherend exhibit a greater presence of these residual adhesives, consistent with findings of the Al-Al SLJs.

3.5.3. Experimental result of hybrid SLJs

Five specimens for each roughness grade of the hybrid SLJs are tested until they fail. The representative load-displacement curves tested from the hybrid SLJs with three roughness grades are illustrated in Figure 3-15. It is observed that the strength and stiffness of the hybrid SLJs increase with higher roughness grades, consistent with findings from the Al-Al and PPA-PPA SLJs. As illustrated in Figure 3-15a and Table 3-10, the average maximum failure load and stiffness of Hybrid-G1 are 1313 N and 17941 N/mm, respectively. In comparison to the Hybrid-G1, the average maximum failure loads of the Hybrid-G2 and the Hybrid-G3 are improved by 47.5% and 76.8%, respectively, while the average stiffnesses of the Hybrid-G2 and the Hybrid-G3 increase 26.4% and 29.5%, respectively.

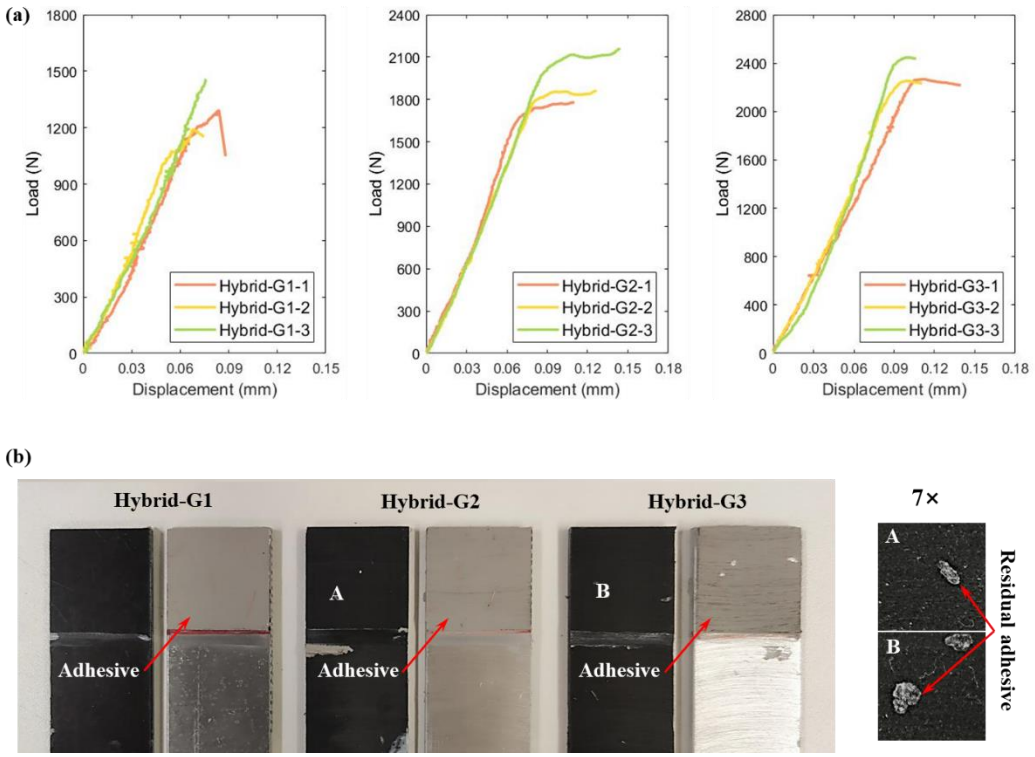

Figure 3-15. Load-displacement curves and failed samples of hybrid SLJs. (a) Load-displacement curves. (b) Failed samples.

Table 3-10. Mechanical Properties of tested hybrid SLJs.

ID	Max failure load (N)	Stiffness (N/mm)
Hybrid-G1-1	1294	16644
Hybrid-G1-2	1191	18859
Hybrid-G1-3	1455	18321
Hybrid-G1 (Average±SD)	1313±133	17941±1155
Hybrid-G2-1	1781	23541
Hybrid-G2-2	1866	22019
Hybrid-G2-3	2163	22474
Hybrid-G2 (Average±SD)	1937±201	22678±781
Hybrid-G3-1	2267	21328
Hybrid-G3-2	2252	23962
Hybrid-G3-3	2448	24410
Hybrid-G3 (Average±SD)	2322±109	23233±1665

Figure 3-15b presents failure modes observed in the failed representative hybrid SLJs. The areas A and B in Figure 3-15b represent the seven-time magnification views of the selected regions of the PPA adherends. All the hybrid SLJs present a single-sided delamination of the joint. As shown in Figure 3-15b, the Hybrid-G1 experiences pure adhesive failure along the adhesion interface of the PPA adherend. The Hybrid-G2 and the Hybrid-G3 show predominant adhesive failure with additional localized cohesive failure, resulting in a small number of residual adhesives attached to some local regions on the surface of the debonded PPA adherends. It is observed that the hybrid SLJs with a higher roughness grade of the adherend exhibit a greater presence of these residual adhesives, consistent with findings from the Al-Al and PPA-PPA SLJs.

3.6 Conclusion

In this chapter, the mechanical properties of the adhesive, adherends and multi-type SLJs used in this research are obtained through experimental studies. The statistical analysis of microstructural roughness and microstructural defects is conducted on different adherend surfaces and regions of the adhesive layer, respectively. According to the analysis of the experimental results, the following conclusions can be summarized:

- Tensile test is conducted on bulk specimens to determine the mechanical properties of Loctite EA 9497. The mechanical properties of this epoxy adhesive, used for the bonding of multi-type SLJs, are summarized in Table 3 1.
- Two different types of adherends, Al and PPA, are used in the fabrication of multi-type SLJs. The tensile tests for both adherends are conducted to characterize their mechanical properties. As indicated in Table 3-2, the yield

stress of Al is 23.7% greater than that of PPA (230 MPa). Additionally, the Young's modulus of Al is 299.8% higher than that of PPA, and Al also allows greater deformation at failure compared to PPA.

- Three roughness grades of Al and PPA adherends are manufactured, with their surface roughness values summarized in Table 3-4. The microstructural adhesion interfaces of SLJs bonded with different roughness grades of Al and PPA adherends are investigated. Rougher surfaces exhibit more pits and protrusions, which can enlarge the contact area between the adherend and adhesive, facilitate the penetration of adhesive and form stronger mechanical interlockings.
- The experimental results demonstrate the presence of microstructural defects of various sizes and shapes distributed within the adhesive layer and on the adhesion interfaces for the adhesive SLJs. Two types of microstructural defects: the interfacial defects and adhesive defects are examined through four regions of the adhesive layer. The volume ratio and equivalent radius of microstructural defects across four regions are presented in Table 3-7. Due to the inferior wettability of the PPA adherend compared to the Al adherend, interfacial defects are more likely to form at the interface of the PPA adherend when bonding with the epoxy adhesive.
- Three types of SLJs with three different roughness grades are studied through SLJ shear test. The experimental results demonstrate that the strength and stiffness of each type of SLJs increase with higher roughness grades of the adherends, as presented in Figure 3-16 and Table 3-11. Furthermore, SLJs with higher roughness grades of the adherends exhibit a more presence of residual adhesive, indicating a greater occurrence of

cohesive failure. This can be due to the fact that rougher surfaces can enlarge the contact area between the adherend and adhesive, enhance adhesive penetration and promote the formation of stronger mechanical interlocks.

- As shown in Figure 3-16 and Table 3-11, when compared at the same roughness grade, the PPA-PPA SLJs exhibit the largest deformation at failure, while the hybrid SLJs experience the second-largest deformation, due to the lower stiffness of the PPA material.
- As shown in Figure 3-16 and Table 3-11, the maximum failure load of the Al-Al SLJ is notably higher than that of both the PPA-PPA and the hybrid SLJ with the same roughness grade, although the average roughness of the Al adherend is lower than the PPA adherend. Additionally, the hybrid SLJ shows the second-highest maximum failure load. This may be explained by the criterion that requires a lower surface tension of adhesive compared to the adherend for good wetting of adhesion. The epoxy achieves excellent adhesion to metal, whilst offer weak adhesion to polymeric substrates [103]. Consequently, the interfacial adhesion between the PPA adherend and the epoxy adhesive is weaker than that between the Al adherend and the epoxy adhesive. Meanwhile, the stiffness of the adherend also plays a crucial role in determining the strength of the joints utilizing an epoxy adhesive. The increase of the stiffness could improve the joint strength [29].

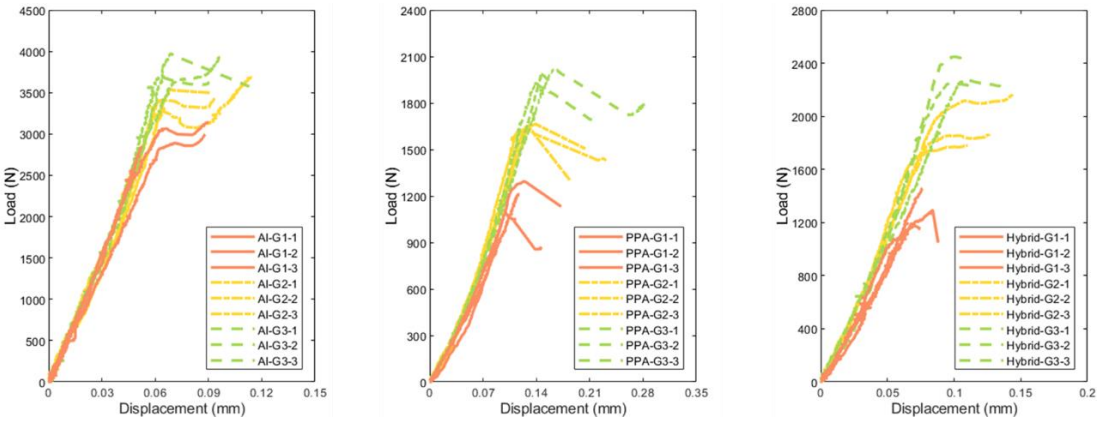

Figure 3-16. Load-displacement curves of all SLJs.

Table 3-11. Ave max failure load and ave stiffness of each subtype of SLJs.

Type	Subtype	Ave max failure load (N)	Ave stiffness (N/mm)
Al-Al SLJ	Al-G1	2990	49126
	Al-G2	3550	51404
	Al-G3	3866	54268
PPA-PPA SLJ	PPA-G1	1200	10168
	PPA-G2	1646	12559
	PPA-G3	1977	12592
Hybrid SLJ	Hybrid-G1	1313	17941
	Hybrid-G2	1937	22678
	Hybrid-G3	2322	23233

Chapter 4

4 DEM model of adhesive joints

4.1 Introduction

The DEM provides valuable insights into complex phenomena such as flow, breakage, and deformation, which are often challenging to capture using traditional continuum-based approaches. As a result, DEM has been increasingly employed to investigate failure mechanisms across various engineering disciplines, including the joints.

In this chapter, The DEM models for the adherends, adhesive, and adhesive joints utilized in Particle Flow Code software package (PFC 2D) are developed. Initially, the microparameters of the contact models for the DEM models of the Al and PPA adherends are calibrated and validated. Subsequently, the microparameters of the contact model for the interlaminar-like property of the thin adhesive layer are refined based on the validated DEM adhesive model. Finally, the DEM DCB, ENF, and SLJ models are employed to further assess the accuracy and reliability of the calibrated microparameters. Numerous experimental results are used to validate the developed DEM models in this chapter.

4.2 DEM model of adherends

4.2.1. Adherends with identical large particle size

Numerical uniaxial tensile tests are performed on adherend samples according to the actual experimental setup, as illustrated in Figure 4-1. The Al and PPA adherends

are represented by yellow and green particles, respectively. The DEM adherend model with identical particle size is composed of large adherend particles with a radius of 95.4 μm, which are packed by a hexagonal arrangement. The overall dimensions of the DEM adherend model is 100 mm×3 mm. The particle arrangement and dimensions of the DEM Al and PPA adherend model are identical, except for the different microparameters of the contact model between particles. A load speed of 0.2 m/s is selected for the DEM adherend model based on the results of a sensitivity analysis. A single particle layer at each of the left and right edges are selected as grips to apply the tensile load, while the middle particles at both edges are used to calculate the strain.

The contact model between the large adherend particles is the soft bond model, chosen for its high efficacy in modelling the ductile property and hardening behavior. The soft bond comprises elastic springs with constant normal and shear stiffnesses, distributed evenly across a cross-section on the contact plane and centered at the contact point. When the bond is active, the force and moment can be correlated with the maximum normal and shear stresses acting on the bond material at the bond periphery. However, if the maximum normal stress acting on the bond exceeds its tensile strength, it may enter a softening regime, governed by the softening factor and softening tensile strength factor.

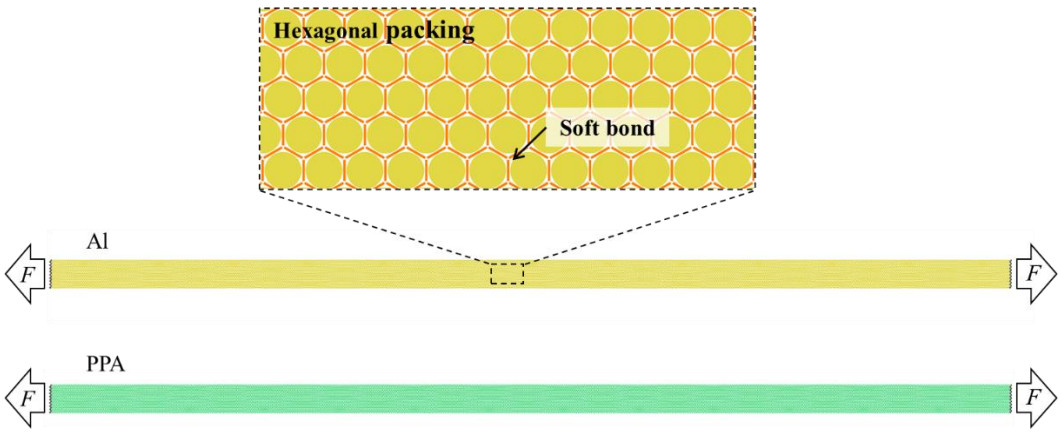

Figure 4-1. DEM model of uniaxial tensile test for adherends.

In the case of hexagonal packing for the particles, the contact stiffness (as shown in Figure 4-2) can be linked to the material properties, such as Young's modulus and Poisson's ratio by applying the general expressions for isotropic materials outlined in [175]. Accordingly, for a 2D homogeneous and isotropic continuum, the contact stiffness is given by:

Normal stiffness $$k_n = 2K_{nm} \tag{4-1}$$

Shear stiffness $$k_s = 2K_{sm} \tag{4-2}$$

Where

$$m = 1, 2, 3 \tag{4-3}$$

$$K_{n1} = \frac{\sqrt{3}}{36}(9d_{11} - 6d_{12} + d_{22})\lambda \tag{4-4}$$

$$K_{s1} = \frac{\sqrt{3}}{18}(3d_{12} - d_{22} - 3\sqrt{3}d_{13} + \sqrt{3}d_{23})\lambda \tag{4-5}$$

$$K_{n2} = \frac{\sqrt{3}}{9}(d_{22} + 2\sqrt{3}d_{23} + 3d_{33})\lambda \tag{4-6}$$

$$K_{s2} = \frac{\sqrt{3}}{18}(3d_{12} - d_{22} + 3\sqrt{3}d_{13} - \sqrt{3}d_{23})\lambda \tag{4-7}$$

$$K_{n3} = \frac{\sqrt{3}}{9}(d_{22} + 2\sqrt{3}d_{23} + 3d_{33})\lambda \tag{4-8}$$

$$K_{s3} = \frac{\sqrt{3}}{9}(d_{22} - 3d_{33})\lambda \tag{4-9}$$

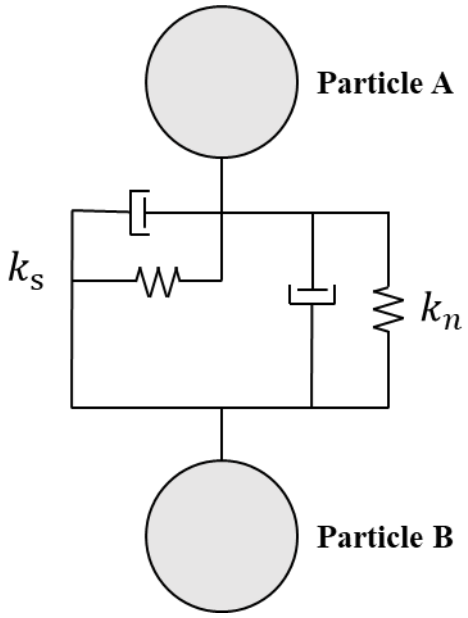

Figure 4-2. Contact between particles.

In above equations, the superscripts n and s represent the normal and shear stiffness, respectively. The terms K_{n1} and K_{s1} refer to the normal and tangential spring constants between disc 0 and disc 1, as well as between disc 0 and disc 4, due to the symmetric layout (as shown in Figure 4-3). Similarly, K_{n2} and K_{s2} correspond to the spring constants between disc 0 and disc 2, and between disc 0 and disc 5. K_{n3} and K_{s3} denote the constants between disc 0 and disc 3, and between disc 0 and disc 6, respectively. λ denotes the element thickness, and d_{ij} (with i and j ranging from 1 to 3) are the elastic coefficients from the stiffness matrix for plane stress, as given below:

$$[D] = \begin{bmatrix} d_{11} & d_{12} & d_{13} \\ d_{12} & d_{22} & d_{23} \\ d_{13} & d_{23} & d_{33} \end{bmatrix} \tag{4-10}$$

Where $d_{11} = d_{22} = E/(1-v^2)$, $d_{12} = vE/(1-v^2)$, $d_{33} = E/2(1+v)$ and $d_{13} = d_{23} = 0$.

For a 2D homogeneous and isotropic continuum, $K_{n1} = K_{n2} = K_{n3}$ and $K_{s1} = K_{s2} = K_{s3}$, Equations 4-1 to 4-9 are reduced respectively to:

$$k_n = \frac{2E\lambda}{2\sqrt{3}(1+v)}\left(1+\frac{2}{3(1-v)}\right) \tag{4-11}$$

$$k_s = \frac{2|(3v-1)|E\lambda}{6\sqrt{3}(1-v^2)} \tag{4-12}$$

where E and v represent elastic modulus and Poisson's ratio of material, respectively. The normal and shear stiffness for the bonds of the large adherend particles are calculated based on Equations 4-11 and 4-12, which are shown in Table 4-1. Other microparameters are calibrated based on the bulk properties of adherends. The detailed definitions of the microparameters can be found out in PFC manual [176].

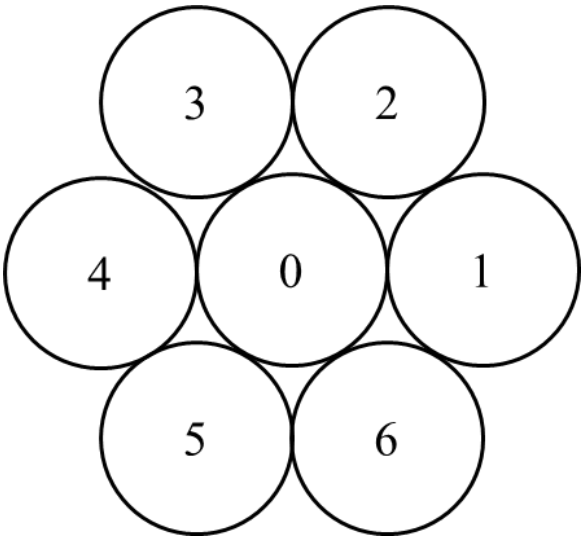

Figure 4-3. Hexagonal packing of particles.

Table 4-1. The calibrated microparameters for the bonds of the large adherend particles.

Parameter	Description	Large Al particle	Large PPA particle
k_n	Normal stiffness (N/m^3)	3.21×10^{14}	7.99×10^{13}
k_s	Shear stiffness (N/m^3)	7.83×10^{12}	7.91×10^{11}
sb_ten	Tensile strength (Pa)	2.54×10^{8}	2.41×10^{8}
sb_coh	Cohesion (Pa)	2.54×10^{8}	2.41×10^{8}
$fric$	Friction coefficient	0.2	0.2
sb_cut	Softening tensile strength factor	0.65	0.9
sb_soft	Softening factor	95	6

These calibrated parameters are applied to the numerical uniaxial tensile test for DEM adherend model, as illustrated in Figure 4-1. The reproduced numerical and experimental stress-strain curves are shown in Figure 4-4. It can be seen that there is good agreement between the numerical and experimental results of the Al and PPA adherends. The yield stress and elongation at fracture of the numerical DEM Al model (Al DEM-L) are 297 MPa and 7.1%, respectively, which are 4.4% and 1.4% higher than the average value obtained from the experimental results. The tensile stress and elongation at fracture of the numerical DEM PPA model (PPA DEM-L) are 250 MPa and 1.4%, respectively, which are 5.7% higher and 12.5% lower than the average value obtained from the experimental results. The Young's modulus of the Al DEM-L and PPA DEM-L is 70516 MPa and 17607 MPa, respectively, with errors of 0.01% and 0.2% compared to the experimental results. Although the plastic response of PPA DEM-L is not fully reproduced relative to the experimental observations, the results remain acceptable, as no PPA adherend failure is reported in previous SLJ shear experiments.

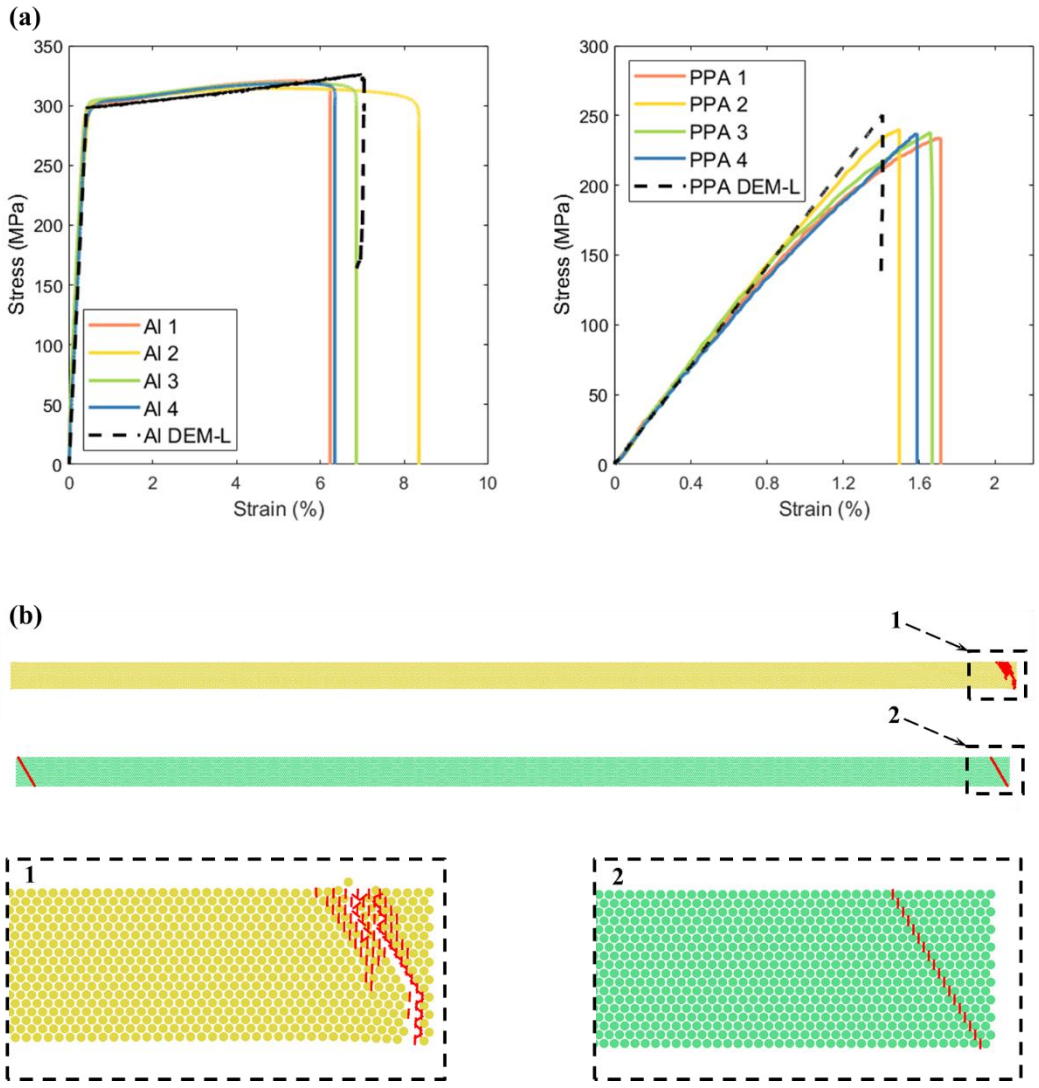

Figure 4-4. Numerical results of DEM adherend model with identical large particles. (a) Stress-strain curves. (b) Fracture results.

Larger particles used in the DEM model typically result in a rougher and less densely packed structure, whereas smaller particles promote a more compact and densely packed arrangement. To investigate the effects of particle size on the bulk properties of the DEM adherend model, five DEM adherend models with different particle layers are developed for Al and PPA using the microparameters for the contact model listed in Table 4-1. The detailed information of these models is presented in Table 4-2. The number of particle layers is calculated along the minimum dimension of the adherend, which is the thickness.

Table 4-2. Specifications of DEM adherend models with different particle layers.

Model	Particle radius (mm)	Particle Layer
DEM-L1	0.095	18
DEM-L2	0.19	9
DEM-L3	0.29	6
DEM-L4	0.57	3
DEM-L5	1.5	1

Figure 4-5 illustrates the numerical results of five DEM adherend models with varying particle layers. For the DEM Al adherend models presented in Figure 4-5a, it is observed that the yield stress and Young's modulus remain nearly identical when the number of particle layers is no fewer than three. The respective maximum differences among these models are 5.0% for yield stress and 1.7% for Young's modulus. Although the elongation at fracture varies significantly among the models, the results remain acceptable, as experimental values for the elongation at fracture of some Al specimens can exceed 20%. Compared to the average results of the models with no fewer than three particle layers, the yield stress and Young's modulus of the Al DEM-L5 model are reduced by 13.1% and 11.5%, respectively, which are 253 MPa and 62101 MPa.

For the DEM PPA adherend models presented in Figure 4-5b, similar trends are observed as in the DEM Al adherend models. The respective maximum differences among the models with no fewer than three particle layers are 5.3% for tensile stress and 3.8% for Young's modulus. Compared to the average results of the models with no fewer than three particle layers, the yield stress and Young's modulus of the Al DEM-L5 model are reduced by 6.6% and 13%, respectively, which are 241 MPa and 15267 MPa. Therefore, to ensure the mechanical properties of both Al and PPA are properly replicated in DEM models, the number of particle layers along the minimum dimension of the adherends should be at least three.

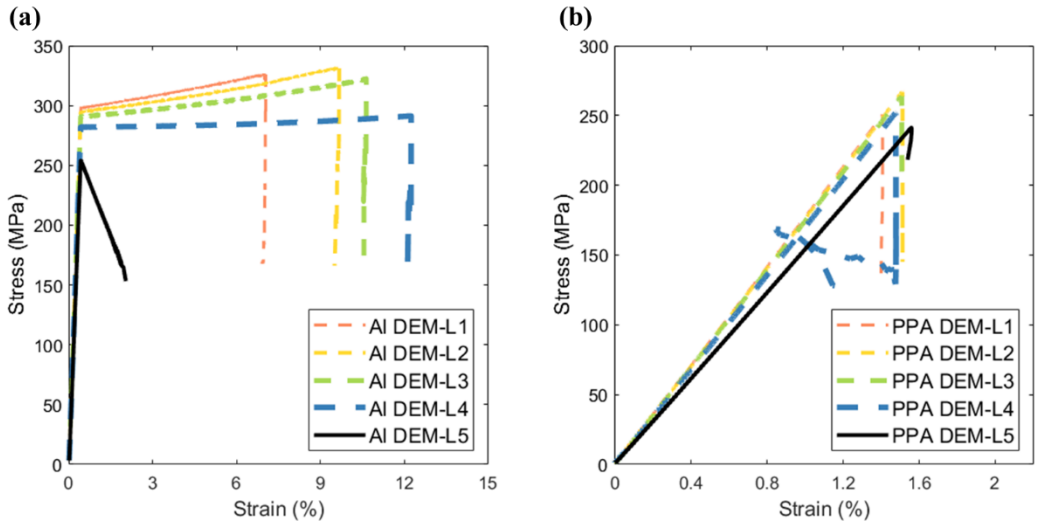

Figure 4-5. Stress-strain curves of DEM adherend models with different particle layers. (a) DEM Al models. (b) DEM PPA models.

4.2.2. Adherends with different particle sizes

To numerically investigate the effect of microstructure on the performance and fracture mechanisms of adhesive joints, the particles of DEM Al and PPA adherends can be partitioned into two regions with two distinct particle sizes, as shown in Figure 4-6. One layer of the particles along the length of the adherend in the DEM adherend model (DEM-L) is removed to generate the small size of adherend particles, as illustrated in Figure 4-6b. The area of the small adherend particles is used as the bonding overlap for the SLJs, with a length of 25 mm. The small adherend particles are randomly seeded. The arrangement of DEM adherend model with different particle sizes aims to optimize the number of total particles, facilitating the generation of microstructure and reduction in computational costs.

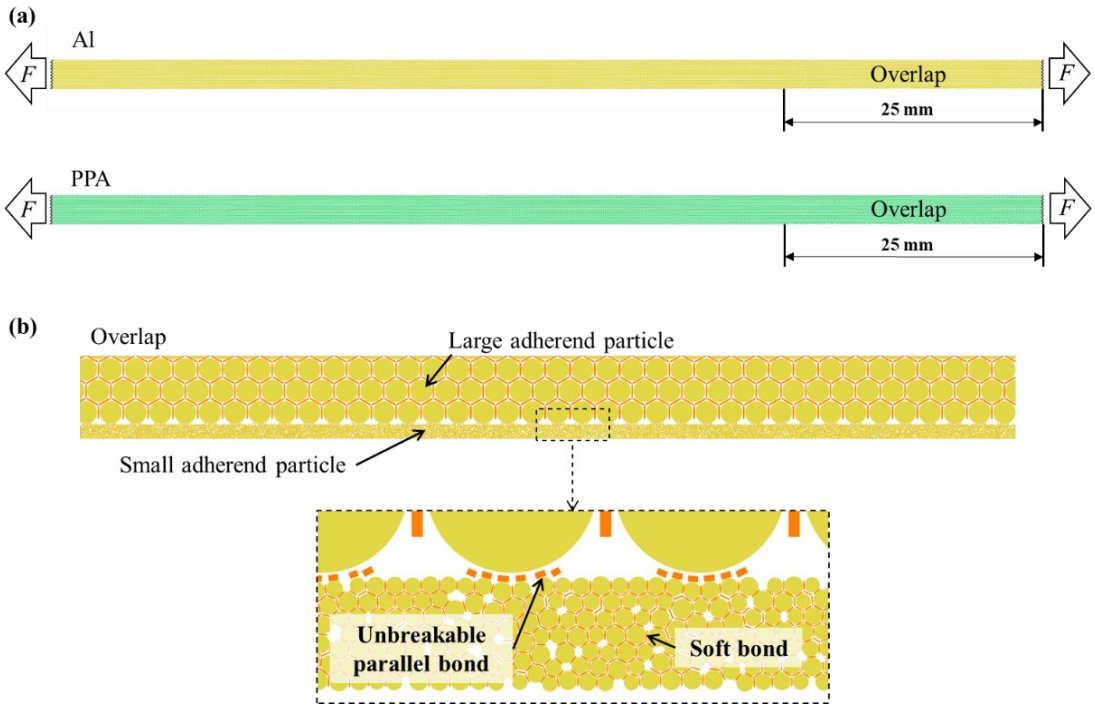

Figure 4-6. DEM model of uniaxial tensile test for adherends with different particle sizes.

Table 4-3. The calibrated microparameters for the bonds of the small adherend particles.

Parameter	Description	Small Al particle	Small PPA particle
sb_emod	Effective modulus (Pa)	9.1×10^{9}	7.87×10^{9}
sb_kratio	Normal to shear stiffness ratio	3.6	3.6
sb_rmul	Radius multiplier	1.44	1.9
sb_ten	Tensile strength (Pa)	1.5×10^{8}	1.08×10^{8}
sb_coh	Cohesion (Pa)	6×10^{8}	4.32×10^{8}
$fric$	Friction coefficient	0.2	0.2
sb_cut	Softening tensile strength factor	1×10^{-4}	0.9
sb_soft	Softening factor	200	100
sb_fa	Friction angle (˚)	30	30

The bond between the large and the small adherend particles is defined by an unbreakable parallel bond model since there is no adherend failure observed in the SLJ shear test (Section 3.5). The parallel bond comprises elastic springs with uniform normal and shear stiffnesses, distributed evenly across a cross-section on the contact plane centred at the contact point. These springs act in parallel with the springs of the linear component, producing force and moment within the bond material due to the relative motion at the contact. The contact model between the small adherend particles is the soft bond model, where the microparameters are calibrated as shown in Table 4-3.

To investigate the effect of small adherend particles, three types of DEM Al and PPA adherend models with different sizes of small adherend particles are investigated. The numerical results of these models compared to the DEM adherend with identical large particles are illustrated in Figure 4-7. The DEM-M1, DEM-M2, and DEM-M3 models are composed of the small particles with radii ranging from 50–66.5 μm, 12.5–17 μm, and 8.3–11 μm, respectively. The layers of small particles along the thickness of the adherends are approximately 1–2, 5–7, and 8–11, respectively.

It is found that the yield stress and Young's modulus of the DEM-M1, DEM-M2, and DEM-M3 of the Al adherend are almost identical, with a maximum difference of 3.5% and 0.03% respectively. The average yield stress and average Young's modulus of the DEM Al adherend model with different particle sizes are 285 MPa and 69658 MPa, respectively, which are 4.0% and 1.2% lower than those of the Al DEM-L. The elongation of the DEM Al adherend models with different particle sizes is significantly different compared to that of the DEM Al adherend model with identical large particle size, particularly in the model containing 1-2 layers of small particles. However, for all experimental results of SLJs in Section 3.5, since there is no adherend failure and only minor adherend deformation, the differences in elongation at fracture are considered

acceptable. For the DEM PPA adherend models, the tensile stress and Young's modulus of the PPA DEM-L, PPA DEM-M1, PPA DEM-M2, and PPA DEM-M3 are nearly the same, with a maximum difference of 5.6% and 1.7% respectively. Therefore, the DEM adherend models with different particle sizes used to construct the microstructure in the DEM SLJ models are appropriate.

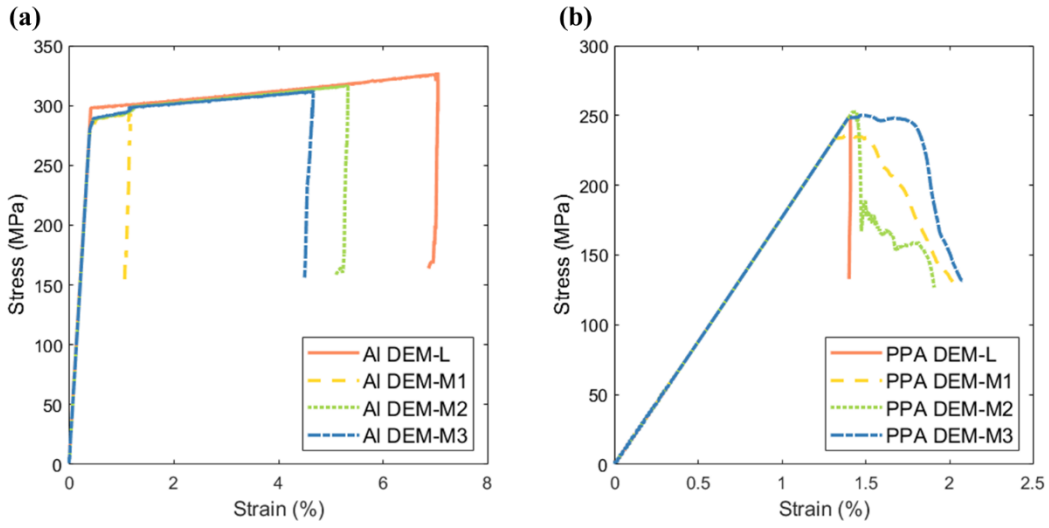

Figure 4-7. Stress-strain curves of DEM adherend models with different particle sizes. (a) DEM Al models. (b) DEM PPA models.

4.3 DEM model of adhesive

4.3.1. Parameter calibration of DEM adhesive model

A numerical uniaxial tensile test is performed on adhesive samples, with the core testing region of a dumbbell-shaped specimen modelled according to the actual experimental setup, as shown in Figure 4-8. The adhesive particles are arranged in a random packing configuration, with soft bonds connecting each particle. The overall dimension of the DEM adherend model is 50 mm×10 mm. In calibrating the DEM model for the epoxy adhesive, numerous microparameters can be adjusted to capture a

wide range of material behaviours. However, this flexibility also introduces substantial challenges in obtaining practical and reliable results. To address this, eleven main microparameters that differ from their default values are used for the numerical uniaxial tensile test. Four microparameters are selected to be fixed with constant values (as listed in Table 4-4), whereas seven microparameters (as listed in Table 4-5) can be calibrated. The tensile strength and cohesion of bond are set to half of the reference strength, and detailed definitions of the microparameters can be found in the PFC manual [176]. The loading speed for the DEM adhesive model is set to 0.05 m/s. Two particle layers at each of the left and right edges are selected as grips to apply the tensile load, while the middle particles at both edges are used to calculate the strain.

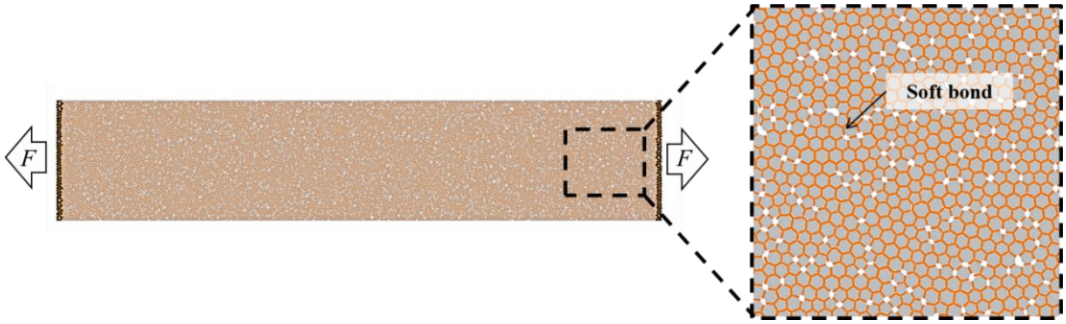

Figure 4-8. DEM model of uniaxial tensile test for adhesive.

Table 4-4. Fixed microparameters of the standard DEM adhesive model.

Symbol	Description	Values
$Porosity$	Porosity of packing particles	0.1
sb_soft	Softening factor	100
sb_cut	Softening Tensile strength factor	0.9
sb_fa	Friction angle (°)	30

Table 4-5. Adjustable microparameters of the standard DEM adhesive model.

Symbol	Parameter	Description
E_m	sb_emod	Effective modulus (MPa)
K	sb_kratio	Normal to shear stiffness ratio
m	sb_rmul	Radius multiplier
fr	sb_ref_str	Reference strength of soft bond (MPa)
r_{min}	$rmin$	Minimum particle radius (mm)
α_a	$alpha\_a$	Ratio of maximum to minimum particle radius
β	$beta$	Ratio of tensile to cohesion strength

Equations 4-13 to 4-15 present the formulas for calculating the contact model parameters of Loctite EA 9497 adhesive, which are derived from a symbolic regression model based on genetic expression programming (GEP), as described in [161]. GEP, a variant of genetic programming, belongs to the wider class of evolutionary algorithms. It focuses on the automatic generation of programs to solve complex problems. The process of GEP starts with the random creation of chromosomes for the initial population. Once the chromosomes are decoded and expressed, the next step is to evaluate the fitness of each individual. The algorithm iterates until a reliable solution is found or the predefined number of generations is reached.

Peak strain

$$\begin{aligned}\varepsilon_p = {} & \tanh(\ln f_{\mathrm{r}} - \ln E_{\mathrm{m}} / 1.1 + \tanh(r_{\mathrm{min}})) - E_{\mathrm{m}} \\ & + 1/(10^{\beta} - (K - 14.4) + \sqrt{E_{\mathrm{m}}}) + E_{\mathrm{m}} \\ & + (\tanh(\ln \sqrt{2.18 f_{\mathrm{r}}} \times \sqrt{\tanh(\alpha_{\mathrm{a}})}))^{1/5}\end{aligned} \tag{4-13}$$

Tensile strength

$$\begin{aligned}f_{\mathrm{t}} = {} & (\ln(8.21 + 106.3 / f_{\mathrm{r}}) - m)^4 \\ & + \tan^{-1}(m)((K - f_{\mathrm{r}}) \times (9.27 + m))^{2/3} \\ & + m^{(f_{\mathrm{r}}/\alpha_{\mathrm{a}})^{1/3}} - 25.13\end{aligned} \tag{4-14}$$

Secant modulus

$$E_s = 45mf_r / K - 103.7\alpha_a K + 695 / \ln(10^{r_{min}} r_{min} + \alpha_a{}^5) + 368.5m\beta + mE_m - 100 r_{min} K^m \quad (4\text{-}15)$$

According to Equations 4-13 to 4-15, the contact model parameters for Loctite EA 9497 are determined based on three macroscopic adhesive properties: tensile strength, peak strain, and secant modulus at strain of 0.001.

Since the ratio of tensile to cohesion strength, is directly associated with the reference strength, it will not be further discussed. Six other parameters are selected to investigate their individual effects on the target properties (peak strain, tensile strength, and secant modulus at a strain of 0.001). Parameters under examination are assigned with specific adjustable ranges, whereas those not under investigation are fixed (refer to Table 4-6). Based on Equations 4-13 to 4-15, the calculated ranges of the target properties for Loctite EA 9497 are presented in Figure 4-9.

Table 4-6. Assigned values of adjustable microparameters for brittle adhesive.

Symbol	Parameter	Fixed values	Adjustable ranges
E_m	sb_emod	3.65×10^3 MPa	2×10^3 - 2×10^4 MPa
K	sb_kratio	3.6	1 - 10
m	sb_rmul	1.9	0.2 - 2
fr	sb_ref_str	46.3 MPa	40 - 100 MPa
r_{min}	$rmin$	0.1 mm	0.05 - 0.5 mm
α_a	$alpha\_a$	1.33	1 - 1.5
β	$beta$	0.25	0.1 - 1

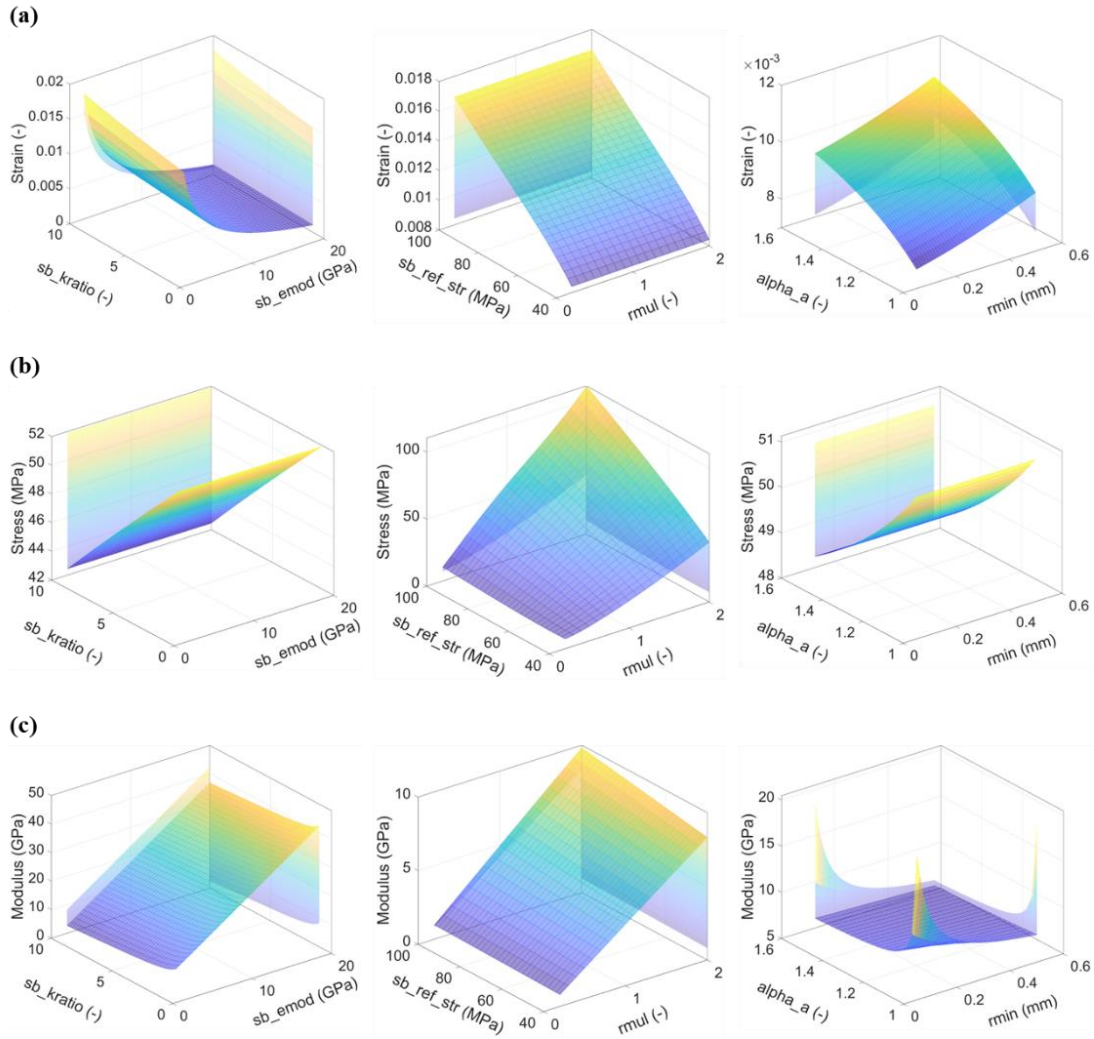

Figure 4-9. Predicted results using regression formulas of brittle adhesives [161].

As illustrated in Figure 4-9a, the effective modulus and the reference strength have a greater impact on the peak strain, while the other parameters show a relatively minor influence on strain variation. Additionally, since the radius multiplier does not appear in the strain equation (Equation 4-13), the peak strain remains unaffected by it. As shown in Figure 4-9b, the reference strength and the radius multiplier are the dominant factors influencing the tensile strength. In Figure 4-9c, it can be observed that the effective modulus and radius multiplier contribute most significantly to the secant modulus.

In general, once the target properties of the adhesives are determined based on experimental data, the parameters exhibiting the most significant influence on each respective property can be initially adjusted and subsequently fixed to obtain the approximate target values. Then, the other parameters with comparatively minor effects can be further optimized to refine the outcomes until the overall set of parameters achieves material properties closely matching the experimental targets. The microparameters for the soft bonds of the adhesive particles are determined and presented in Table 4-7. These parameters are applied to the numerical uniaxial tensile test for the DEM adhesive model, as illustrated in Figure 4-8. The reproduced numerical and experimental stress-strain curves are shown in Figure 4-10. It can be observed that the DEM results are in good agreement with the experimental results. The tensile stress and Young's modulus of the DEM adhesive model are 35.9 MPa and 9915 MPa, respectively, with deviations of 2.3% and 2.8% from the experimental results.

Table 4-7. The calibrated microparameters for the bonds of the adhesive particles.

Parameter	Description	Values
sb_emod	Effective modulus (MPa)	5.1×10^3
sb_kratio	Normal to shear stiffness ratio	4.7
sb_rmul	Radius multiplier	1.9
sb_ref_str	Reference strength of soft bond (MPa)	35
r_{min}	Minimum particle radius (mm)	0.3
$alpha\_a$	Ratio of maximum to minimum particle radius	1.33
$beta$	Ratio of tensile to cohesion strength	1
sb_cut	Softening tensile strength factor	0.9
$Porosity$	Porosity of packing particles	0.1
sb_soft	Softening factor	100
sb_fa	Friction angle (˚)	30

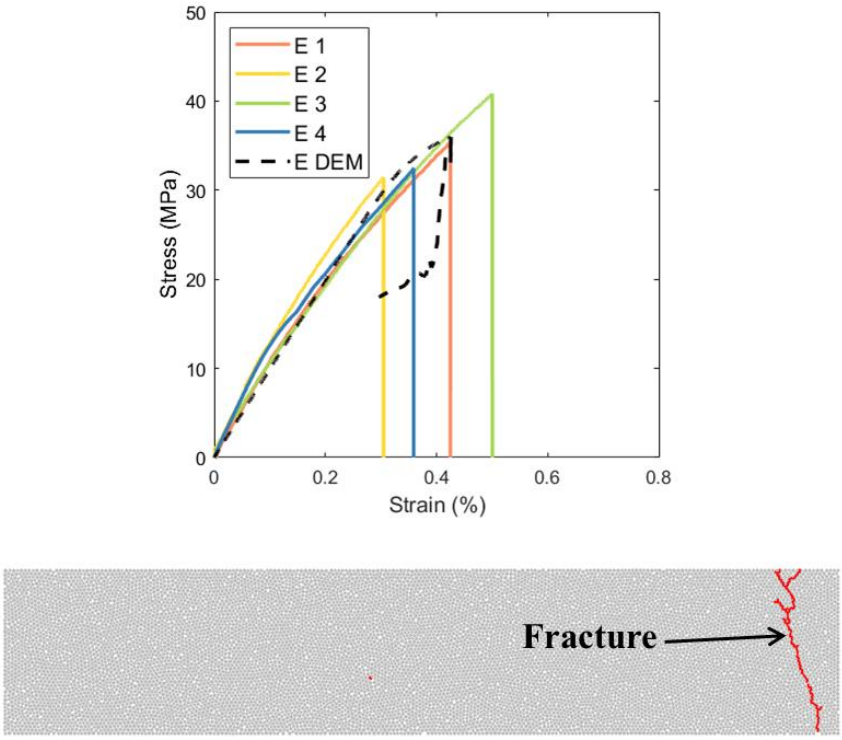

Figure 4-10. Numerical results of DEM adhesive model.

To investigate the effect of microstructure on the performance and failure mechanisms of adhesive joints, the particles of adhesive in the DEM models can be refined to microscopic sizes. However, using extremely small particles significantly increases the total number of particles, resulting in a substantial computational cost. Therefore, to balance the reproduction of microscopic particle sizes and the reduction of computational expense, the influence of particle size on the DEM adhesive model is further examined based on the microparameters presented in Table 4-7. The stress-strain curves of the DEM adhesive models with different particle layers are illustrated in Figure 4-11. The detailed information and bulk properties of these models are summarised in Table 4-8.

As shown in Figure 4-11 and Table 4-8, the tensile stresses of all DEM adhesive models are quite similar, with a maximum difference of 3.2%, whereas their Young's moduli differ significantly. Compared to the E DEM-5 model, which has a minimum

particle radius of 0.1 mm and more than 38 particle layers along the thickness direction, the Young's modulus of models with fewer than 4 particle layers along the thickness decreases by more than 13.6%. For models with more than 5 particle layers, the Young's moduli are quite similar, with a maximum difference of only 4.5%. Therefore, to ensure the mechanical properties of the adhesive are properly captured in DEM models, the adhesive along minimum dimension should be covered by more than 5 particle layers.

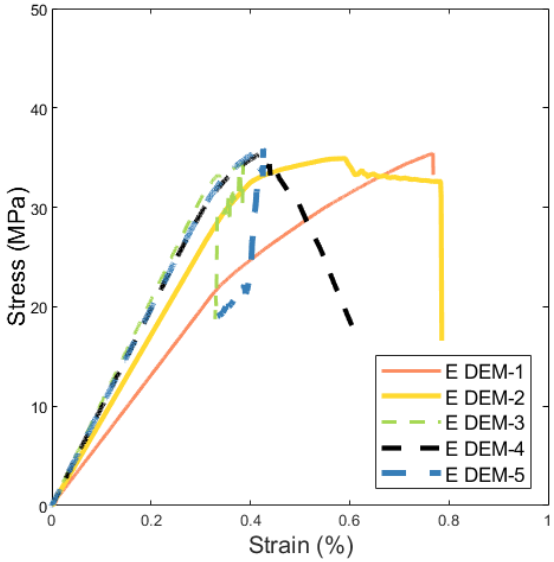

Figure 4-11. Stress-strain curves of DEM adhesive models with different particle layers.

Table 4-8. The bulk properties of different DEM adhesive models.

Model	Particle radius (mm)	Layer	Tensile strength (MPa)	Young's modulus (MPa)
E DEM-1	1.80 - 2.39	2 - 3	35.5	6559
E DEM-2	1.10 - 1.46	3 - 4	34.9	8569
E DEM-3	0.70 - 0.93	5 - 7	34.8	10366
E DEM-4	0.30 - 0.40	12 - 16	35.5	9916
E DEM-5	0.10 - 0.13	38 - 50	35.9	9915

4.3.2. Interlaminar-like property of thin adhesives in joints

Compared to the thick adhesive layers, the thin adhesive layers are more commonly used in the joint design. In such cases, the interlaminar-like properties are the primary concern in DEM modelling, particularly the fracture energy. This is because the actual performance of a thin adhesive layer is significantly influenced by factors such as adhesive thickness, the stiffness of the adherends and constraints from adherends, which affect both the fracture strength and fracture energy [161]. Due to these effects, the bulk properties of the adhesive cannot be directly used to simulate the behaviour of a thin adhesive layer constrained between adherends. Therefore, this subsection focuses on the cohesive properties of the thin adhesive layers in the joints and refines the microparameters of the contact model for the DEM model with thin adhesive layer.

The cohesive properties extracted from an adhesive layer with a thickness of 0.56 mm, which exhibited cohesive failure, are presented in Table 4-9. These properties are obtained from Al–Al joint specimens. Additional details can be found in reference [174]. To calibrate the interlaminar-like properties in both the normal and tangential directions, two simplified DEM models involving different joint configurations are conducted, as illustrated in Figure 4-12. These two DEM joint models, each incorporating adhesive layers with a thickness of 0.56 mm, are used to evaluate the normal and shear cohesive properties of the thin adhesive layer in DEM models. The Al adherends are hexagonally packed particles with a radius of 0.2 mm. The adhesive layer is comprised of randomly seeded particles with a minimum radius of 0.05 mm. For both models, a loading speed of 0.02 m/s is applied, and the right edge of the adherend is subjected to tensile loading until epoxy cracking propagated through the entire adhesive layer. The displacement for these two models is calculated as the

displacement difference between the red points (interfacial adherend particles) shown in Figure 4-12 at the middle region of adhesive layer along the loading direction.

Table 4-9. Cohesive properties of the thin adhesive layer [174].

Property	Symbol	Loctite EA 9497
Normal Fracture energy	G_{IC} (N/mm)	0.26±0.06
Tangential Fracture energy	G_{IIC} (N/mm)	0.90±0.39
Normal fracture strength	σ_n (MPa)	25.35±10.26
Tangential fracture strength	σ_t (MPa)	16±5

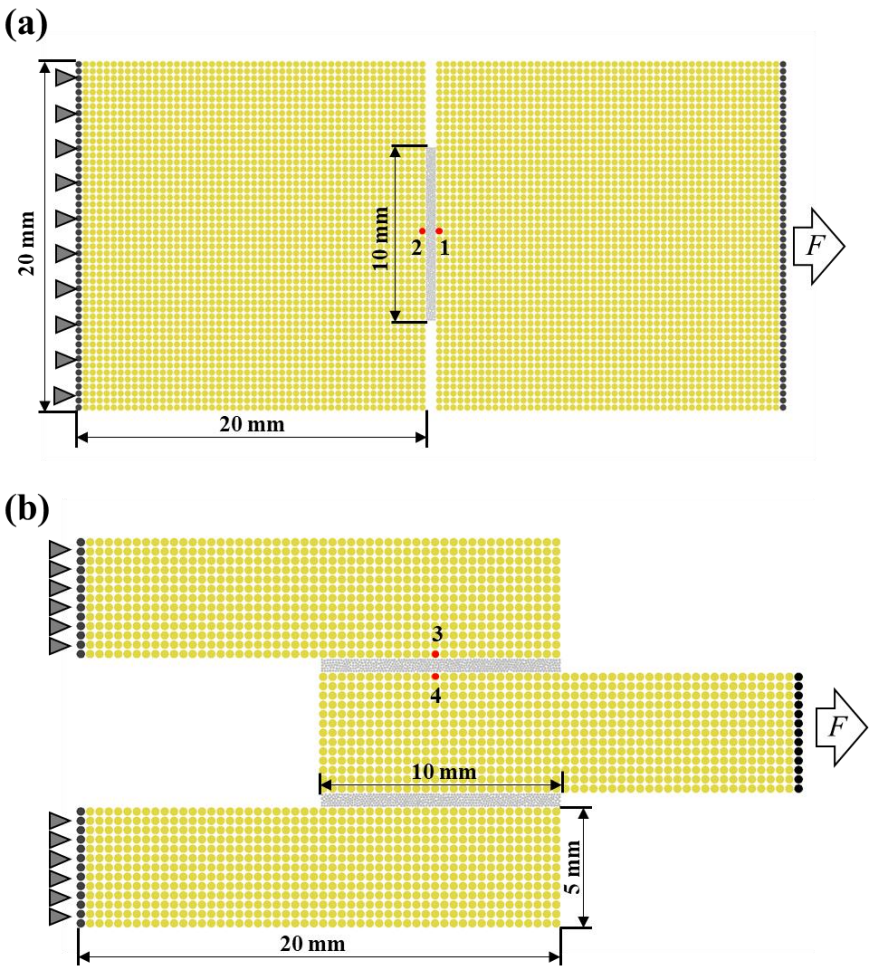

Figure 4-12. DEM models for the calibration of interlaminar-like property of thin adhesive layers. (a) Model for normal interlaminar-like property. (b) Model for tangential interlaminar-like property.

The particle configuration and contact models for both the Al adherend and the adhesive are adopted from the data presented in the previous subsection. However, the reference strength of the contact model for the adhesive particles is refined to 18 MPa. The refined microparameters for the bonds of the thin adhesive layer are summarised in Table 4-10. To ensure cohesive failure in the two DEM adhesive joint models illustrated in Figure 4-12, the interfacial bonds between the Al adherend and the adhesive particles are defined as unbreakable parallel bonds. Figure 4-13 illustrates the numerical results of DEM models for normal and tangential interlaminar-like properties of an adhesive layer with a thickness of 0.56 mm. These two models present cohesive failure of adhesive joints. According to the separation-traction law shown in Figure 4-13a, the normal and tangential fracture strengths are 15.3 MPa and 11.6 MPa, respectively. The fracture energy is calculated by integrating the normal and tangential stress over the relative displacement between two reference adherend particles located at the adhesive interface. The normal and tangential fracture energy is 0.31 N/mm and 0.70 N/mm, respectively.

Table 4-10. The refined microparameters for the bonds of the adhesive particles.

Parameter	Description	Values
sb_emod	Effective modulus (MPa)	5.1×10^3
sb_kratio	Normal to shear stiffness ratio	4.7
sb_rmul	Radius multiplier	1.9
sb_ref_str	Reference strength of soft bond (MPa)	18
r_{min}	Minimum particle radius (mm)	0.3
$alpha\_a$	Ratio of maximum to minimum particle radius	1.33
$beta$	Ratio of tensile to cohesion strength	1
sb_cut	Softening tensile strength factor	0.9
$Porosity$	Porosity of packing particles	0.1
sb_soft	Softening factor	100
sb_fa	Friction angle (˚)	30

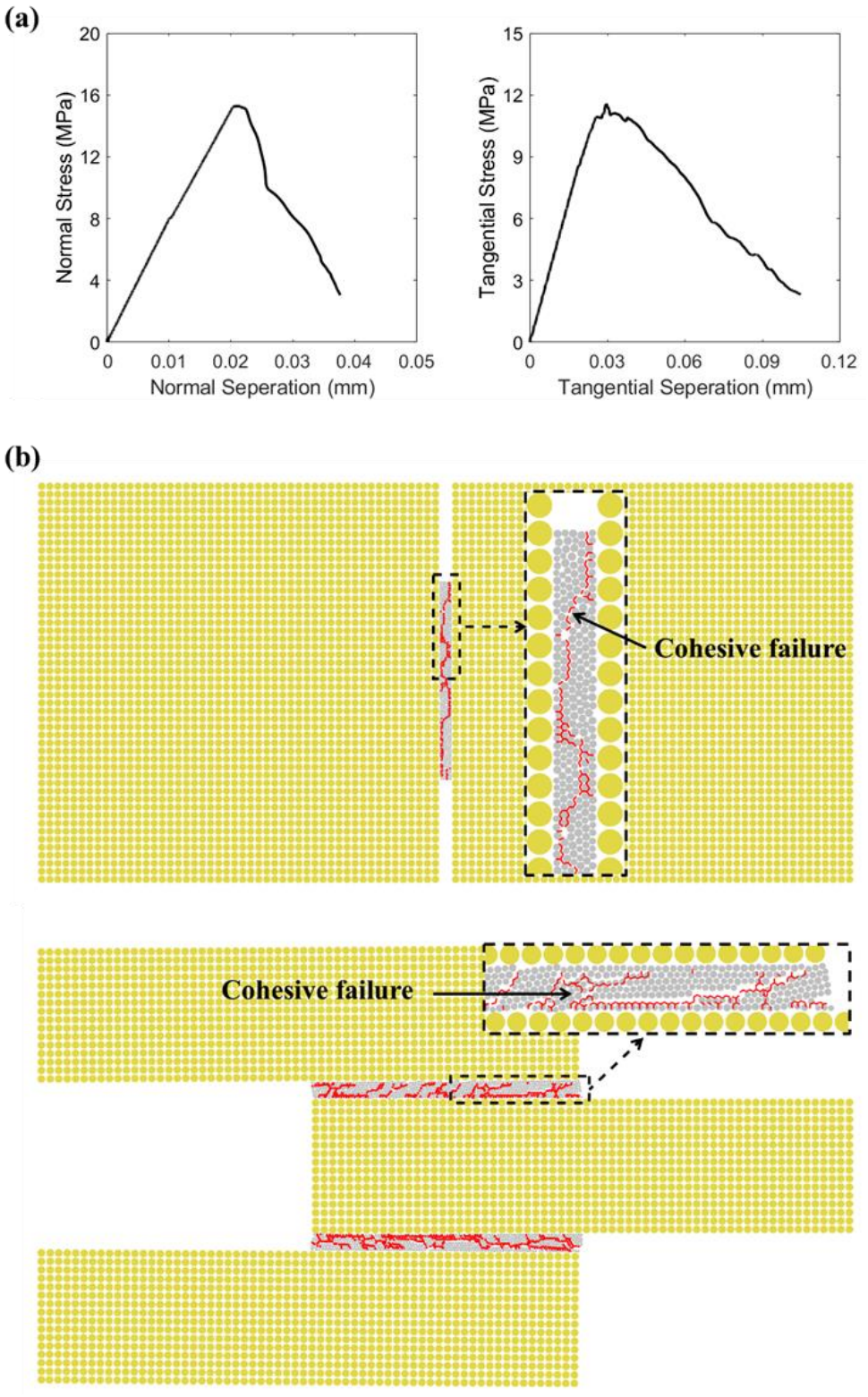

Figure 4-13. Numerical results of models for normal and tangential interlaminar-like property. (a) Separation-traction law. (b) Fracture result.

Although the normal and tangential fracture strengths and fracture energies fall within the range of the referenced experimental results in Table 4-9, some values are slightly lower or higher than the experimental means. Such deviations are reasonable, considering the relatively large standard deviations in Table 4-9, which result from the limited number of samples and the inherent variability of the adhesive properties, including microstructural defects. Therefore, the refined reference strength of the contact model for the adhesive particles can effectively reproduce the interlaminar-like property of thin adhesives in the DEM adhesive joint model.

4.4 Validation of calibrated parameters

To validate the calibrated parameters of the contact models for the adherend and adhesive particles in DEM joints, especially the cohesive properties of the thin adhesive layer, three types of DEM joint models are constructed which are DEM DCB model, DEM ENF model, and DEM SLJ model. The numerical results of the three models, obtained using the calibrated parameter sets for the Al adherend and adhesive presented in Table 4-1 and Table 4-10, are validated against experimental observations from DCB, ENF, and SLJ tests conducted with the Al adherends. All the experimental data used in this section and characterized by cohesive failure of the adhesive joints, are referenced from the study [174]. In DCB and ENF tests, the adhesive is subjected exclusively to pure mode I and mode II loading, respectively, whereas it experiences a mixed-mode load combining both mode I and mode II in the SLJ configuration.

4.4.1. DEM DCB model

The model configuration of DEM DCB model is shown in Figure 4-14. The Al adherends, with a length of 200 mm and a thickness of 12.7 mm, are modelled using hexagonally packed particles with a radius of 0.2 mm. The adhesive layer, with a length of 150 mm and a thickness of 0.56 mm, is modelled using randomly seeded particles with a minimum radius of 0.05 mm. The initial crack length in DEM DCB model is 50 mm. The loading speed for the DEM DCB model is set to 0.05 m/s at the red points shown in Figure 4-14, and the displacement of the top red point along the loading direction is recorded.

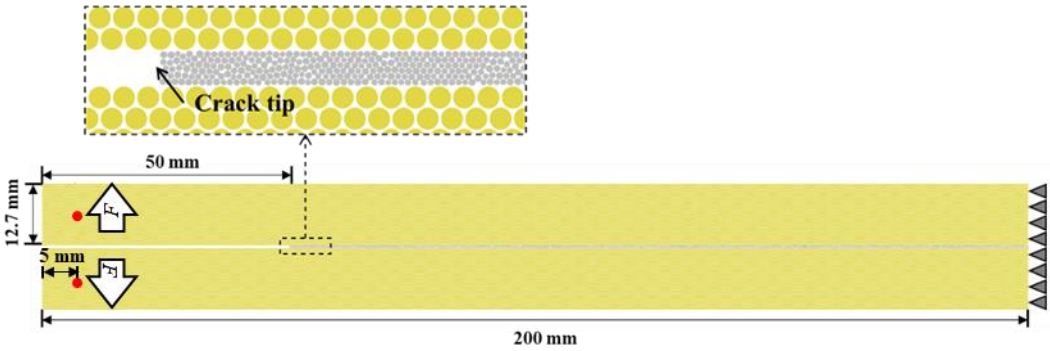

Figure 4-14. Configuration of the DEM DCB model.

Figure 4-15 illustrates the numerical result of the DEM DCB model with the experimental results (DCB E1, DCB E2, and DCB E3) referred from the study [174]. As shown in Figure 4-15a, the numerical result agrees with the experimental results. The maximum failure load and stiffness of the DEM DCB model are 951 N and 3431 N/mm, respectively. These values represent an increase of 9.1% in maximum failure load and a decrease of 7.9% in stiffness compared to the average experimental results. The numerical results show a consistency with those obtained from the DCB experiment, despite the presence of oscillations during the post-peak stage, which are attributed to dynamic effects associated with fracture propagation in DEM. The initial cracks occur

at the left end of the overlap and subsequently propagate toward the right, resulting in cohesive failure (Figure 4-15b). The calibrated parameters for the DEM DCB model show reliability in simulating mode I cohesive failure for the thin adhesive layer.

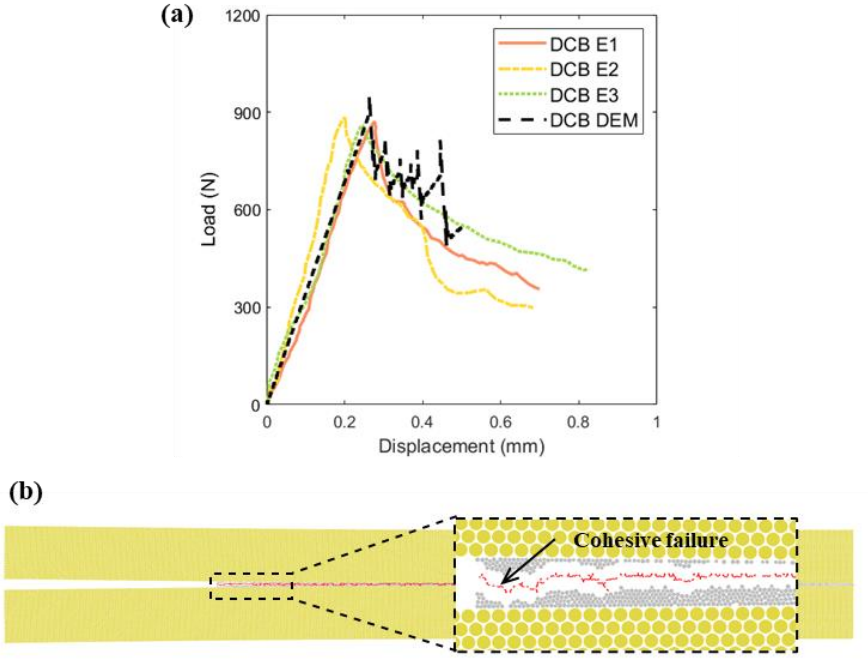

Figure 4-15. Numerical results of DEM DCB model. (a) Load-displacement curves. (b) Fracture result.

4.4.2. DEM ENF model

The model configuration of DEM ENF model is shown in Figure 4-16. Compared to the DEM DCB model, the DEM ENF model has modified dimensions, with the adherend length increased to 300 mm and the adhesive layer length increased to 250 mm, while all other parameters including the configuration of the particles remain unchanged. Additionally, one pin is placed at the midpoint of the upper adherend to apply the load, while two pins are positioned near both ends of the lower adherend, each located 25 mm from the respective edge, to fix the specimen in place. The Al adherends are hexagonally packed particles with a radius of 0.2 mm. The adhesive layer

is comprised of randomly seeded particles with a minimum radius of 0.05 mm. The loading speed for the DEM ENF model is set to 0.05 m/s at the top pin, and the displacement of the top pin along the loading direction is recorded.

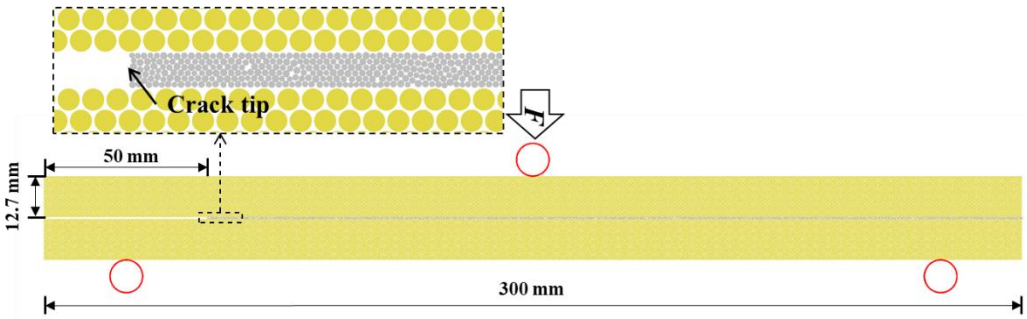

Figure 4-16. Configuration of the DEM ENF model.

Figure 4-17 illustrates the numerical result of the DEM ENF model with the experimental results (ENF E1, ENF E2, and ENF E3) referred from the study [174]. As shown in Figure 4-17a, the maximum failure load of the DEM ENF model is 9665 N with an error of 6.4% compared to the average value of the experimental results. It also has a good accuracy of predicting the behaviour of ENF at the post-peak stage. However, the stiffness of the DEM ENF model is 7006 N/mm, decreased by 23.1% compared to the experimental results. It is likely that the measured displacement in the experimental data is underestimated relative to the actual value. This can be attributed to the small displacement at peak load with a magnitude of nearly 1 mm, which poses a challenge for accurate detection by the measurement sensors. In contrast, data from other sensor indicates a displacement at peak load of around 1.5 mm [161]. Consequently, it is reasonable to consider that the recorded displacement values in the experiment are likely underestimated. As illustrated in Figure 4-17b, the initial cracks occur in the left end of the adhesive layer, and then propagate toward the right, resulting in cohesive failure. The calibrated parameters for the DEM ENF model show reliability in simulating mode II cohesive failure for the thin adhesive layer.

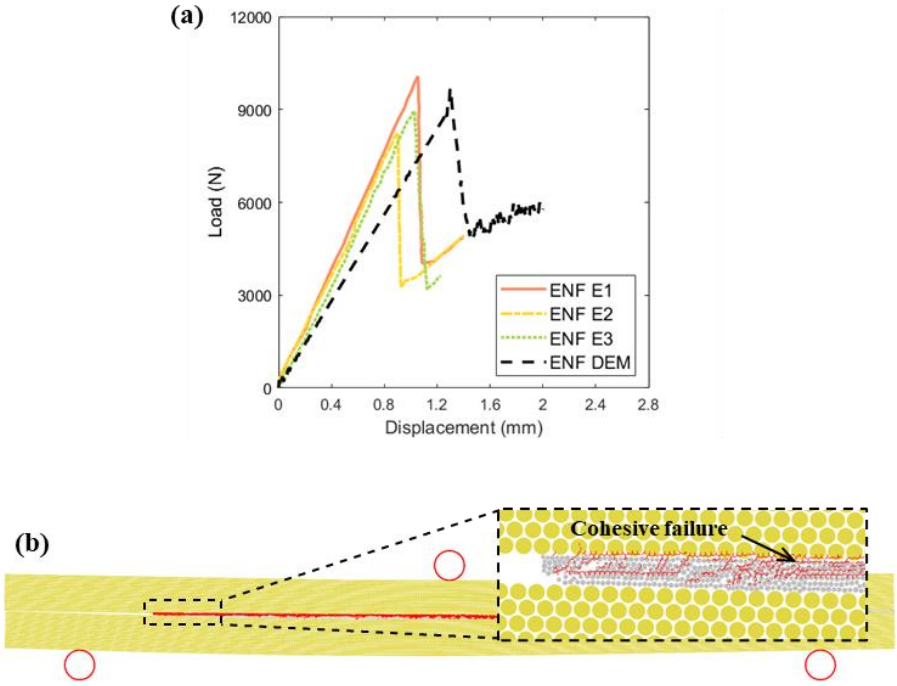

Figure 4-17. Numerical results of DEM ENF model. (a) Load-displacement curves. (b) Fracture result.

4.4.3. DEM SLJ model

The model configuration of DEM SLJ model is shown in Figure 4-18. The dimensions of the model are identical to those shown in Figure 3-4, except for the overlap length, which is 12.5 mm, and the adhesive thickness, which is 0.56 mm. The Al adherends are hexagonally packed particles with a radius of 0.16 mm. The adhesive layer is comprised of randomly seeded particles with a minimum radius of 0.05 mm. The loading speed for the DEM SLJ model is set to 0.05 m/s, and the displacement of the red point in Figure 4-18 along the loading direction is recorded.

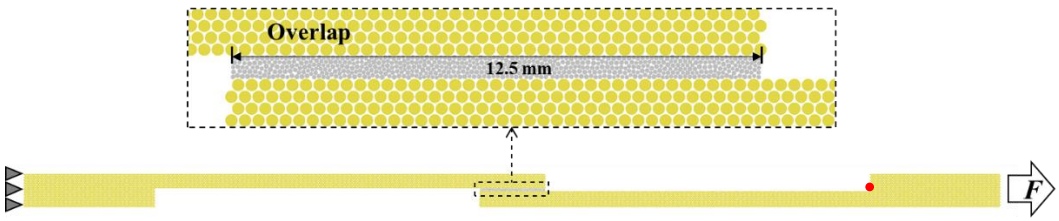

Figure 4-18. Configuration of the DEM SLJ model.

Figure 4-19 illustrates the numerical result of the DEM SLJ model with the experimental results (SLJ E1, SLJ E2, and SLJ E3) referred from the study [174]. The numerical findings closely match the experimental observations. As shown in Figure 4-19a, the average maximum failure load of the SLJ tests is 3749 N, while the numerical result is 3599 N, resulting in a difference of 4%. The average stiffness of the SLJ tests is 18173 N/mm, while the numerical result is 18119 N, resulting in a difference of 0.3%. Two initial cracks emerge at the left and right of the overlap. Then they propagate to the middle region of the overlap and join together to form complete cohesive failure of SLJ, as shown in Figure 4-19b. The calibrated parameters for the DEM SLJ model show reliability in simulating mixed-mode cohesive failure for the thin adhesive layer.

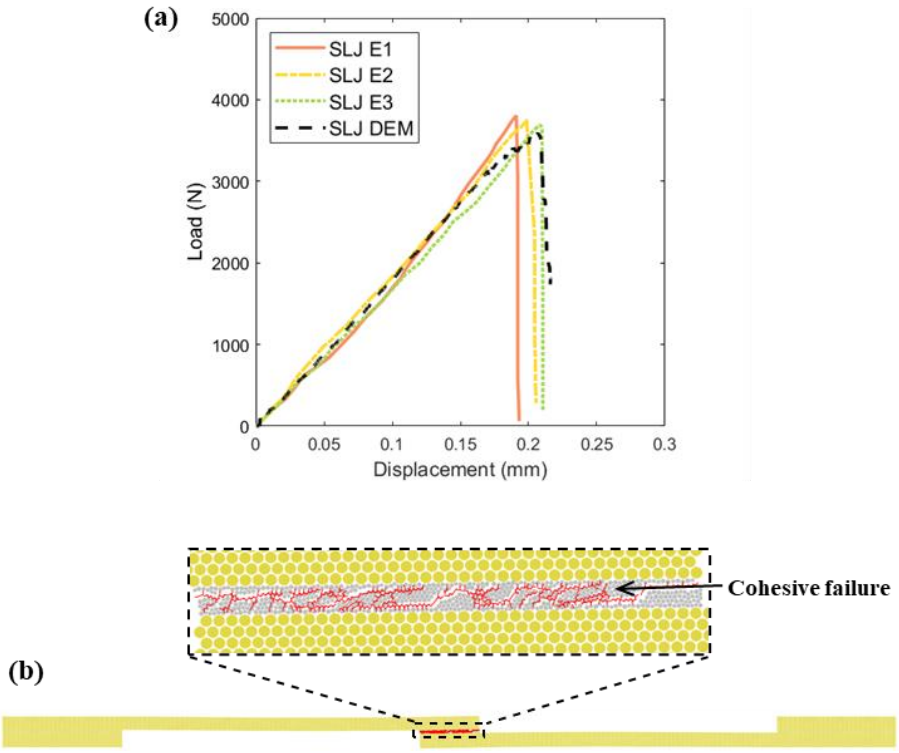

Figure 4-19. Numerical results of DEM SLJ model. (a) Load-displacement curves. (b) Fracture result.

4.5 Conclusion

In this chapter, DEM models for Al adherend, PPA adherend, and Loctite EA 9497 adhesive are developed. Specifically, the microparameters of the contact models for the adherends and adhesive are calibrated and validated through a series of experimental results. Based on the analysis of the numerical results, the following conclusions are drawn:

- For the Al and PPA adherend, the DEM models with the calibrated microparameters for the contact model between the identical large particles are built in PFC. The calibrated parameters are presented in Table 4-1. The numerical bulk properties of the adherends exhibit good agreement with the experimental data. Additionally, the minimum number of particle layers along the smallest dimension of the adherends is determined.
- To construct the microstructure for adhesive joints, the particles of DEM Al and PPA adherends can be partitioned into two regions with two distinct particle sizes. The calibrated microparameters for the large particles are provided in Table 4-1, while those for the small particles are listed in Table 4-3. The numerical results demonstrate that using different particle sizes to represent the adherend in the DEM models for this study is appropriate and effective.
- The microparameters of the contact model for the DEM adhesive model are calibrated using equations derived from a symbolic regression model based on genetic expression programming, as presented in Table 4-7. The numerical bulk properties of the adhesive successfully replicate the trends observed in the experimental data. Furthermore, the minimum

number of adhesive particle layers along the smallest dimension of the adhesive layer is determined.

- Considering the interlaminar-like property of the thin adhesive layer in joints, the microparameters of the contact model for the thin adhesive layer are refined, as listed in Table 4-10. Two simplified DEM models are conducted to evaluate the refined parameters for the thin adhesive layer. The numerical results demonstrate that the refined parameters accurately capture the interlaminar-like behaviour of the thin adhesive layer in the DEM models.
- To validate the calibrated microparameters of the contact models for the adherend and adhesive in DEM model, especially the cohesive properties of the thin adhesive layer, The DEM DCB model, DEM ENF model and DEM SLJ model are developed. The numerical results of these models validate that the calibrated parameters for the DEM adhesive joint models show reliability in simulating mode I, mode II and mixed-mode cohesive failure.

Chapter 5

5 Effect of microstructural roughness on the performance and fracture mechanism of multi-type SLJs

5.1 Introduction

Although many previous studies have dedicated on the joint performance in consideration of surface roughness, there are no sufficient investigations specifically addressing the fracture mechanisms of joints at microscale to clarify the effects of roughness on joint performance. In addition to experimental investigations, employing suitable numerical methods capable of accurately portraying the microstructural features and capturing the micromechanical behaviors is also crucial to explore more insightful information about the effect of roughness on the fracture mechanisms of adhesive joints.

This chapter conducts systematic numerical investigations into the performances and microscale fracture mechanisms of multi-type SLJs affected by surface roughness, with a microscale focus on analyzing the characteristics and properties of the adhesion interfaces resulting from the different adherend materials and surface profiles. Based on the experimental results, the microparameters of the contact models for the adhesion interface of the Al-Al and PPA-PPA SLJ models with minimum roughness grades are calibrated respectively, which are assumed to be close to zero roughness. Then, the calibrated microparameters are applied to other DEM SLJ models with higher roughness grades by introducing real microstructural roughness profiles measured by experiments. Consequently, the performance and fracture mechanisms of

multi-type SLJs encompassing both identical and hybrid SLJs, affected by the microstructural roughness can be investigated.

5.2 Numerical modelling

5.2.1. Model configuration for the adherends and adhesive

The DEM utilized PFC 2D is employed for the numerical investigation on the influence of roughness on the performance and fracture mechanism of multi-type SLJs at microscale. A representative arrangement of particles of the DEM SLJ model is illustrated in Figure 5-1 using a hybrid SLJ. In this study, the Al and PPA components are denoted by yellow and green particles, respectively, whereas the epoxy adhesive is shown by grey particles.

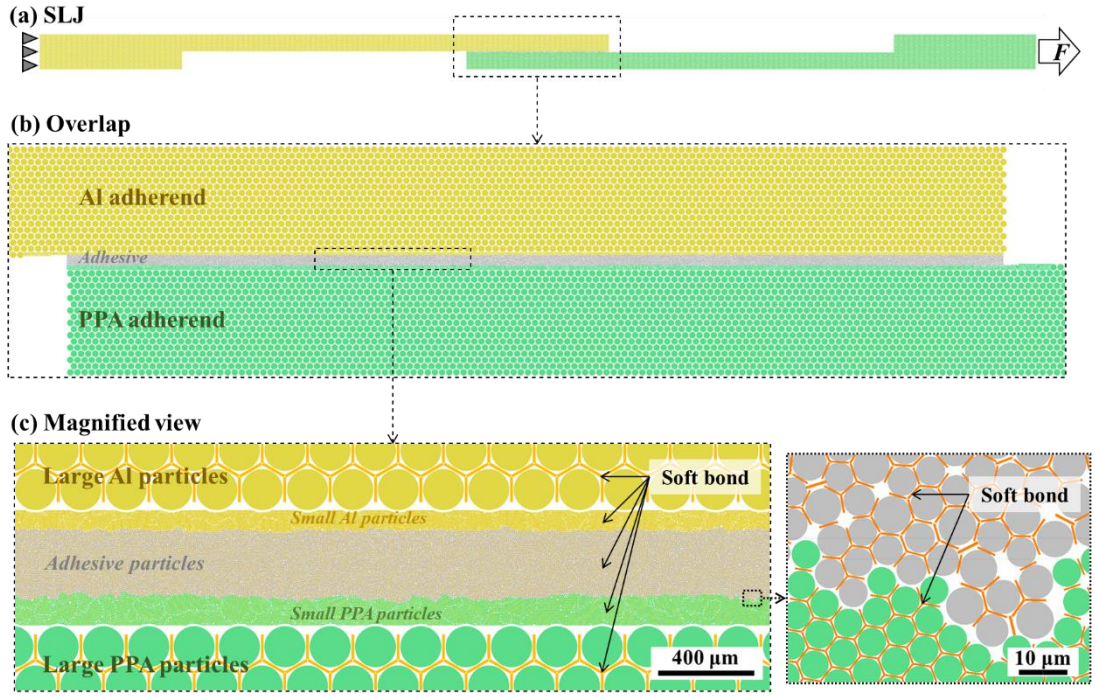

Figure 5-1. The arrangement of particles for SLJ with roughness. (a) The entire structure of SLJ. (b) The overlap area of SLJ. (c) The particle composition and contact model.

The Al and PPA particles, representing the adherends, are partitioned into two regions with two distinct particle sizes, as shown in Figure 5-1c. A hexagonal arrangement is used to pack the large adherend particles of 95.4 μm in radius, encompassing a substantial portion of the entire model. The small adherend and adhesive particles are randomly generated. On average, there are more than ten layers of small adherend particles through the thickness direction to mitigate the non-uniform stress transmissions induced by the difference in radii of the adherend particles. The radius of the small adherend and adhesive particles is set to be 3.2 μm and 3.2-4.3 μm, respectively. In this study, the determined arrangement and size of the particles aim to optimize the number of total particles, facilitating the generation of microroughness profiles and reduction in computational costs. The contact model between the particles with the same properties is the soft bond model. The microparameters of the soft bond models for the large adherend particles, small adherend particles, and adhesive particles are presented in Table 4-1, Table 4-3, and Table 4-10, respectively.

5.2.2. Model configuration for the interfaces

There are no specific microroughness profiles for the Al-G1, PPA-G1, and Hybrid-G1 DEM SLJ models due to the measured R_a of the adherends with G1 roughness is close to zero and approximately an order of magnitude lower than the those measured for the G2 and G3 adherends, as shown in Table 3-4. The profiles of grade 2 and grade 3 roughness are quantified from the randomly selected ground Al and PPA adherend surfaces, and subsequently reconstructed in the DEM models for the Al-Al, PPA-PPA, and hybrid SLJs.

The characteristics for the adhesion interfaces of the DEM SLJ models are summarized in Table 5-1, where L_r is the ratio of the true curved length of rough

surfaces to that of a flat surface. The average roughness R_a of the randomly selected surface roughness profiles for the DEM SLJ models is in the range specified in Table 3-4. For the DEM SLJ models, the quantity of the interfacial bonds for the adhesion interfaces improves with the increase in the average roughness of the adherend surface. This is attributed to the enlarged contact area between the adherend and adhesive, resulting from the rougher adherend surface.

Table 5-1. The characteristics of the adhesion interfaces for the DEM SLJ models.

Adherend	R_a (μm)	L_r	Number of interfacial bonds
Al grade 1	< 0.204	1	4974
Al grade 2	1.980	1.275	6476
Al grade 3	4.072	1.377	6986
PPA grade 1	< 0.223	1	4974
PPA grade 2	2.189	1.358	6714
PPA grade 3	6.884	1.469	7292

Figure 5-2 demonstrates the method of generation of the adhesive and adhesion interfaces in the DEM SLJ models. The hybrid SLJ models are used as examples. First, the Al (top) and PPA (bottom) adherends are placed with 0.2 mm distance as the baseline model (Figure 5-2a). Then, adhesive particles are randomly seeded and expanded to fully fill in the area between the adherends, forming two interfaces with the adherend particles for the Hybrid-G1 model, as illustrated in Figure 5-2b. The models portrayed in Figure 5-2c and Figure 5-2d are from Hybrid-G2 model and Hybrid-G3 model, respectively. These two models are constructed by regenerating the microroughness profiles along the interfaces of the baseline model. According to the measured coordinate data of the microscopic surface from the Al and PPA adherends, small adherend particles are deleted along the edges of the adherends to create surface roughness profiles, then the adhesive particles undergo random seeding and size-

controlled expansion between the adherends to form the Hybrid-G2 model and Hybrid-G3 model. The same modeling method is also used for the Al-Al and PPA-PPA SLJ models.

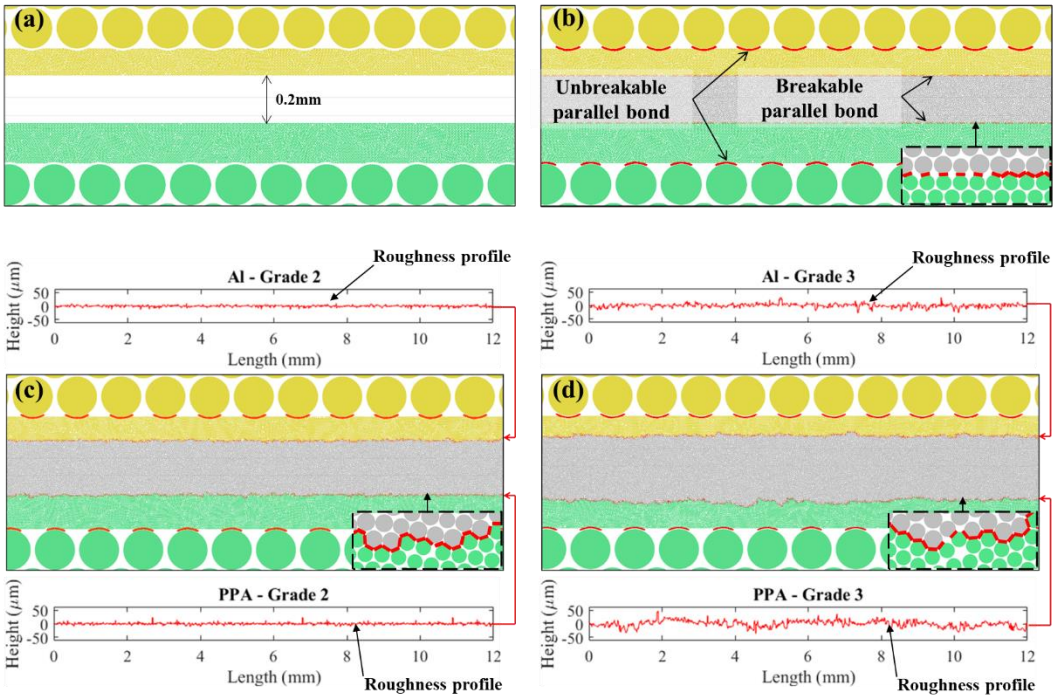

Figure 5-2. The generation for hybrid SLJ models (local magnification view). (a) The baseline model. (b) The Hybrid-G1 model. (c) The Hybrid-G2 model. (d) The Hybrid-G3 model.

Due to the particle-based nature of the developed model, the Al-G1, PPA-G1 and Hybrid-G1 models also can exhibit some weak interlocking and frictional effects even without a constructed roughness profile, as illustrated in Figure 5-2b. However, the density of the small particles is quite high along the interface, and it is also observed that weak interlocking and frictional effects exist in the experiments for the SLJ with G1 roughness profile (Figure 3-7). Thus, this error can be negligible.

The bond between the large and the small adherend particles is defined by an unbreakable parallel bond model since there is no adherend failure observed in the SLJ shear test. The contact model for the interfacial bonds between the small adherend and

the adhesive particles is defined by a breakable linear parallel bond model. It cracks in tension when the positive normal stress acting on the bond reaches the tensile strength, or in shear when the absolute value of the shear stress acting on the bond reaches the shear strength. Moreover, the tensile strength of the parallel bond $\overline{\sigma_c}$ is a modifiable microparameter. However, the shear strength of the bond $\overline{\tau_c}$ is initially set by the modifiable cohesion $\bar{c}$, then updated by following equations:

$$\text{Shear strength} \qquad \overline{\tau_c} = \bar{c} - \bar{\sigma}\, tan\overline{\emptyset} \tag{5-1}$$

$$\text{Normal stress} \qquad \bar{\sigma} = \overline{F_n}/\bar{A} \tag{5-2}$$

$$\text{Cross-sectional area} \qquad \bar{A} = 2\bar{R}t \tag{5-3}$$

where $\bar{A}$ denotes the cross-section area of the parallel bond. $\bar{R}$ represents the radius of the minimum particle between two particles multiplied by radius multiplier. t equals to 1 for a 2D model. $\overline{F_n}$ and $\bar{\sigma}$ represent the normal force and normal stress acting on the bond, respectively. $\overline{\emptyset}$ denotes the friction angle.

According to Equations 5-1 to 5-3 and the failure criteria of the parallel bond, when two particles are in a steady state of tension, the shear strength reduces, with the increase of positive normal stress, resulting in breakage of bond either in tension or shear. In the scenario where two particles are mutually compressed, the bond will exclusively experience shear crack. This is because the negative normal stress cannot exceed the defined tensile strength of bond.

The experiment results show that the failure of all the SLJs in this research predominantly occurs at the adhesion interface. Therefore, it is crucial to accurately calibrate the microparameters of the interfacial bonds for the DEM SLJ models.

Excessively great initial shear strength (cohesion) of the interfacial bonds should be avoided as it will result in only tension cracks when the adhesive and adherend particles are under tension, or unbreakable interfacial bonds in both shear and tension when the adhesive and adherend particles are under compression.

As illustrated in Figure 5-3, when the tension cracks predominate along the adhesion interfaces in the DEM models, a large amount of bonds along the adhesion interface maintains intact due to the compressive effect between some adhesive and adherend particles, causing the propagation of massive cracks into the adhesive to demonstrate a form of cohesive failure. As a result, the failure mode and performance of the DEM SLJ models are not consistent with the experimental results. To overcome the above difficulties, the tensile strength, initial shear strength (cohesion) and friction angle of the interfacial bonds are calibrated to ensure that the bond cracks at the adhesion interface are predominantly shear cracks. The calibrated microparameters for the interfacial bonds are summarized in Table 5-2.

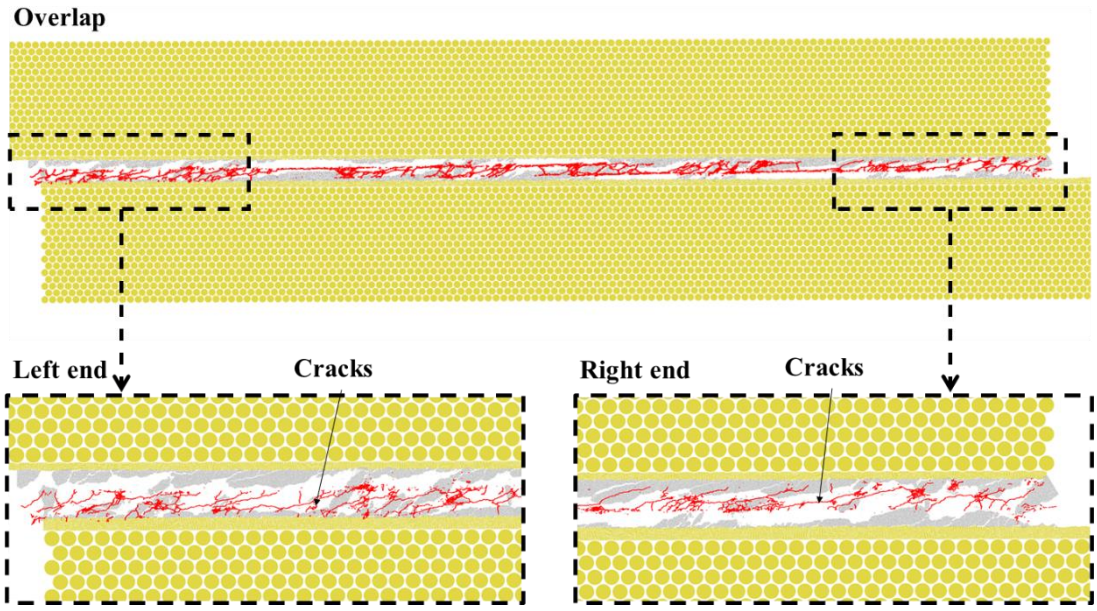

Figure 5-3. Fracture results of Al-Al SLJ model with excessively great initial shear strength of the interfacial bonds.

Table 5-2. The calibrated microparameters for the interfacial bonds.

Parameter	Description	Al adhesion interface	PPA adhesion interface
pb_kn	Normal stiffness (N/m^3)	3.38×10^{11}	4.47×10^{10}
pb_ks	Shear stiffness (N/m^3)	2.84×10^{11}	4.37×10^{10}
pb_ten	Tensile strength (Pa)	4.38×10^{7}	6.08×10^{7}
pb_coh	Cohesion (Pa)	3.84×10^{6}	1.14×10^{6}
pb_fa	Friction angle (°)	14	14

5.3 Numerical results

5.3.1. Al-Al SLJ

Figure 5-4 presents the deformation and fracture mechanisms of the Al-G1 model. The maximum failure load and stiffness of the Al-G1 model are 2941 N and 50808 N/mm, respectively. The errors between the numerical and experimental results of the Al-G1 SLJ are 1.6% and 3.4% in predicting the maximum failure load and the stiffness, respectively. While the joint exhibits sudden failure in experiments, the numerical results show a more gradual failure process. This behaviour can be attributed to the fact that failure occurs between individual particles, and the numerical model consists of a large number of discrete particles, which distributes the damage over time.

For the Al-G1 model, the failure mode is mixed-mode failure, predominantly adhesive failure along the interface, with cohesive failure at the two ends and the middle region of the overlap. The initial cracks coalesce within the adhesive and the adhesion interfaces near the two ends of the overlap region, resulting from the local stress concentrations, as illustrated in Figure 5-4c.1. Then the primary cracks within the adhesive from the two ends propagate quickly to and along the two adhesion interfaces towards the middle region of the overlap. With the increase of the load, the primary

cracks eventually join each other within the adhesive layer and induce a large number of cracks around, leading to a complete fracture (Figure 5-4b).

Apart from minor cohesive failure at both ends and in the middle region, the predominant failure mode of the Al-G1 model is adhesive failure. As shown in areas A-D of Figure 5-4b, no residual adhesive remains on the surface of the debonded Al adherends after failure, except at the two ends of the adherend. This is also observed in the experiment (Figure 3-12). The number of the cracks in the Al-G1 model is 14798.

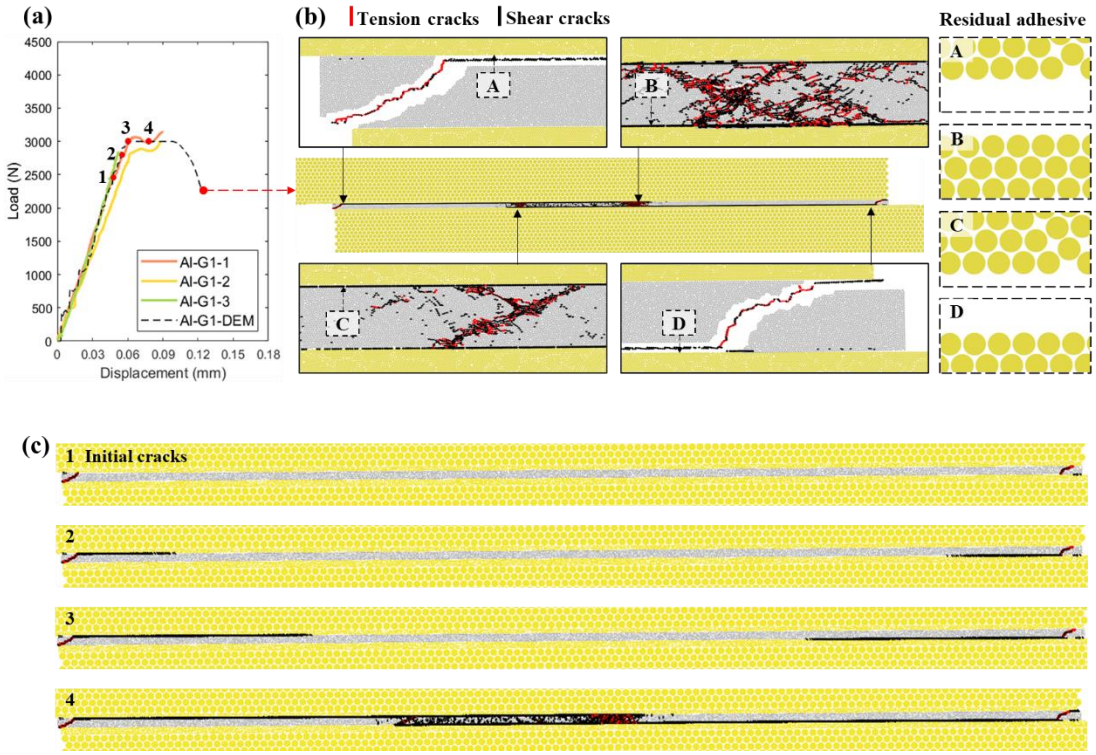

Figure 5-4. Load-displacement curves and fracture process of Al-G1 SLJ. (a) Load-displacement curves of Al-G1. (b) Numerical fracture result of Al-G1. (c) Crack propagation of Al-G1.

Figure 5-5 presents the deformation and fracture mechanisms of the Al-G2 model. The maximum failure load and stiffness of the Al-G2 model are 3557 N and 54145 N/mm, respectively. The errors between the numerical and experimental results

of the Al-G2 SLJ are 0.2% and 5.3% in predicting the maximum failure load and the stiffness, respectively.

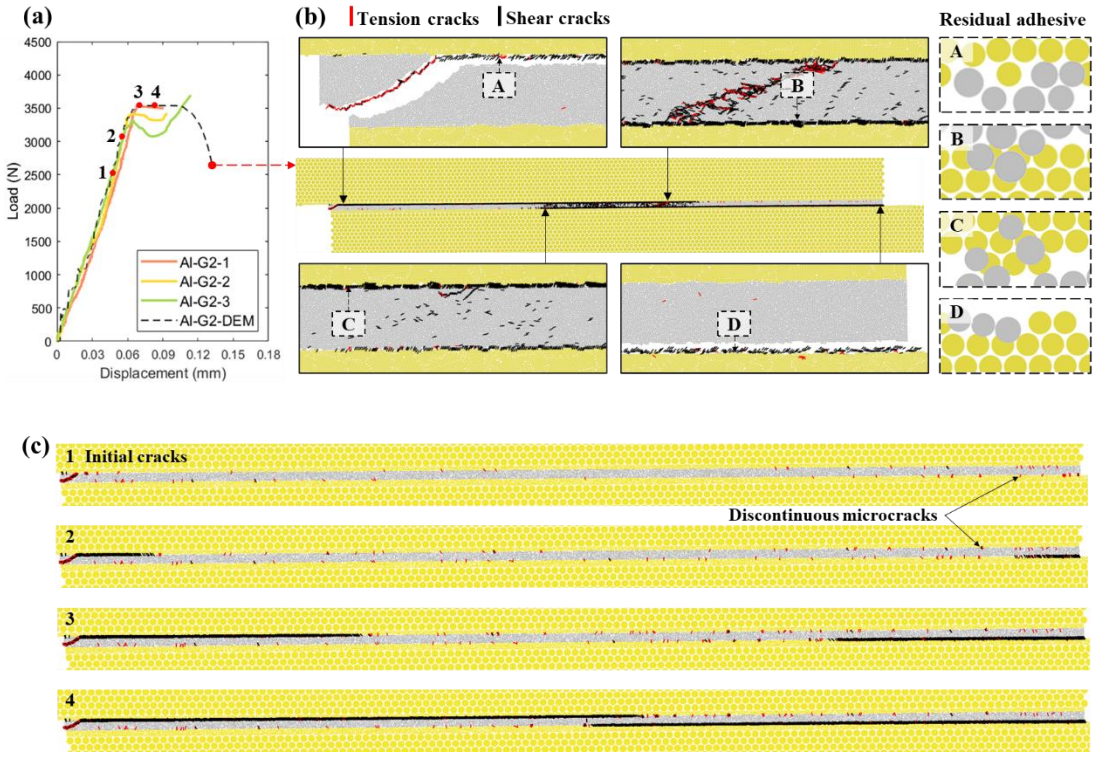

Figure 5-5. Load-displacement curves and fracture process of Al-G2 SLJ. (a) Load-displacement curves of Al-G2. (b) Numerical fracture result of Al-G2. (c) Crack propagation of Al-G2.

The failure mode of the Al-G2 model is mixed-mode failure. The fracture process of the Al-G2 model is slightly different to that of the Al-G1 model. With the increase of the surface roughness, the microscopic profiles of the adherend surface become more complex, thereby developing more stochastic local stress concentrations. Consequently, minor discontinuous microcracks firstly occur along the two adhesion interfaces and within the adhesive in the immediate vicinity of the interfaces, while the initial primary cracks emerge from both ends of the overlap, as shown in Figure 5-5c.1 and Figure 5-5c2. With the increase of the external loading, the primary cracks propagate along the two interfaces to the central region of the joint, and more

discontinuous microcracks are induced, as demonstrated in Figure 5-5c.2 to Figure 5-5c.4.

Since the primary cracks grow tortuously through the interface and the discontinuous microcracks in the vicinity of the interfaces, residual adhesives exist discretely on some local regions of the surface of the debonded Al adherends after failure (areas A-D of Figure 5-5b), which is also observed in the experiment (area A of Figure 3-12). Additionally, the position and morphology of the initial primary cracks from the two ends are not entirely symmetric as shown in Figure 5-5c.2. It is attributed to the variations of the local microroughness profile at the two ends, resulting in complicated and distinct local stress concentrations in these two regions. The number of the cracks in the Al-G2 model is 16343, which is greater than that in the Al-G1 model.

Figure 5-6 presents the deformation and fracture mechanisms of the Al-G3 model. The maximum failure load and stiffness of the Al-G3 model are 3679 N and 54924 N/mm, respectively. The errors between the numerical and experimental results of Al-G3 SLJ are 4.8% and 1.2% in predicting the maximum failure load and the stiffness, respectively.

The failure mode of the Al-G3 model is mixed-mode failure. The fracture process of the Al-G3 model is similar to that of the Al-G2 model. Initially, discontinuous cracks also occur along the two interfaces and within the adhesive in the immediate vicinity of the interfaces, while the primary cracks initiate from the two ends of the overlap (Figure 5-6c.1). The primary cracks propagate tortuously through the interface and the discontinuous microcracks, as shown in Figure 5-6c.2. However, the number of the discontinuous microcracks in the adhesive is greater due to more stochastic local stress concentrations induced by the higher grade of surface roughness, resulting in more residual adhesives on some local regions of the surface of the debonded Al

adherends (areas A-D of Figure 5-6b), which is also observed in the experiment (area B of Figure 3-12).

Additionally, there are some diagonal continuous cracks developed within the adhesive during the propagation of the primary cracks, as shown in Figure 5-6c.2-4. This is due to the fact that the increased number of discontinuous microcracks reduces the average distance between the two individual microcracks located on the opposite interfaces. Consequently, the probability of forming a continuous crack through the adhesive increases. The number of cracks in the Al-G3 model is 19011, which is greater than that in both the Al-G2 and Al-G1 models.

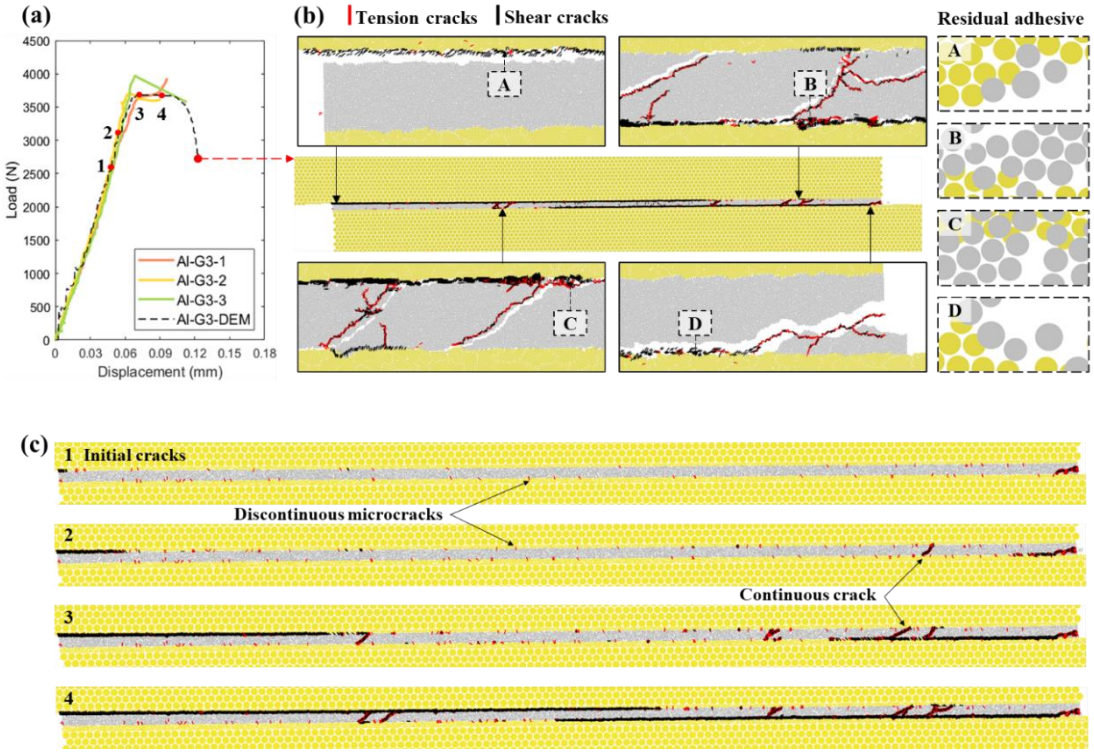

Figure 5-6. Load-displacement curves and fracture process of Al-G3 SLJ. (a) Load-displacement curves of Al-G3. (b) Numerical fracture result of Al-G3. (c) Crack propagation of Al-G3.

5.3.2. PPA-PPA SLJ

Figure 5-7 presents the deformation and fracture mechanisms of the PPA-G1 model. The maximum failure load and stiffness of the PPA-G1 model are 1217 N and 10289 N/mm, respectively. The errors between the numerical and experimental results of the PPA-G1 SLJ are 1.4% and 1.2% in predicting the maximum failure load and the stiffness, respectively.

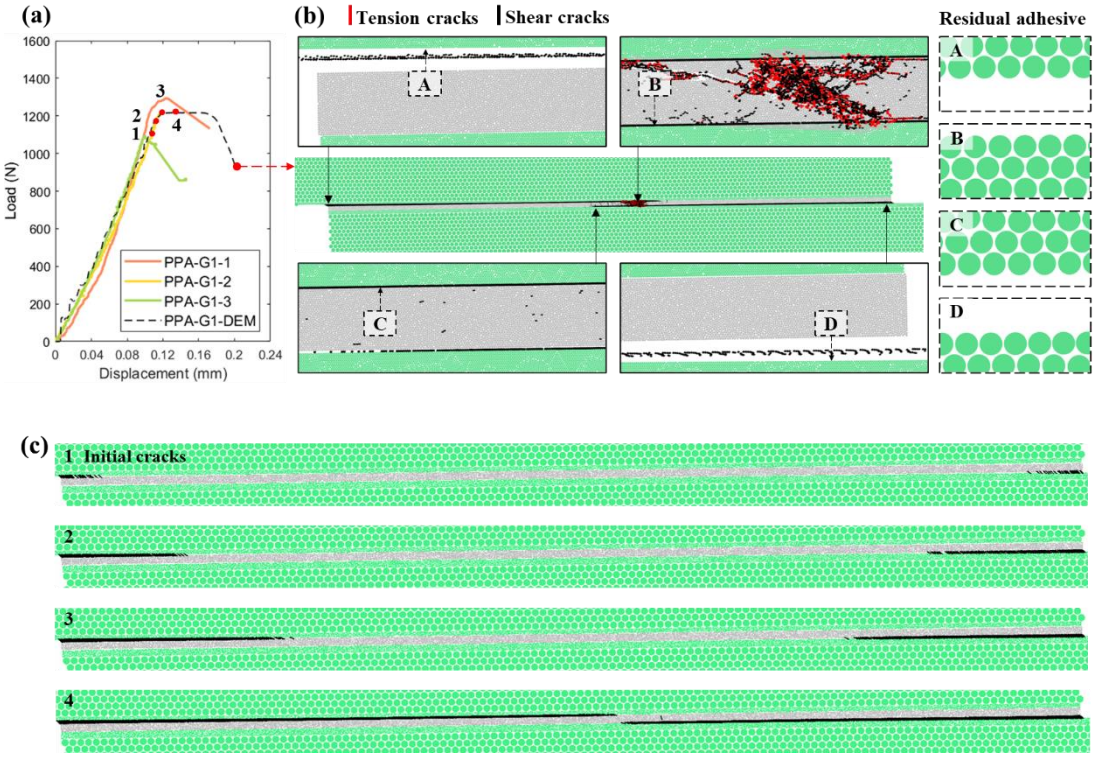

Figure 5-7. Load-displacement curves and fracture process of PPA-G1 SLJ. (a) Load-displacement curves of PPA-G1. (b) Numerical fracture result of PPA-G1. (c) Crack propagation of PPA-G1.

The failure mode of the PPA-G1 is characterized by predominantly adhesive failure along the interface, with cohesive failure at the middle region of the overlap. The crack initiation and propagation of the PPA-G1 model exhibit some distinctive features compared to the Al-G1 model, showing more adhesive failure in the PPA-PPA SLJs. The initial primary cracks of the PPA-G1 model only coalesce on the adhesion

interfaces at the two ends of the overlap, as illustrated in Figure 5-7c.1. With the increase of the external loading, the primary cracks then continuously propagate along the two interfaces and towards the central regions of the overlap (Figure 5-7c.2 to 4). Ultimately, the primary cracks at the top and the bottom interfaces join within the adhesive layer, generating some cracks around and causing the final fracture, as shown in Figure 5-7b. The number of the cracks in the PPA-G1 model is 10441.

Figure 5-8 presents the deformation and fracture mechanisms of the PPA-G2 model. The maximum failure load and stiffness of the PPA-G2 model are 1633 N and 11756 N/mm, respectively. The errors between the numerical and experimental results of the PPA-G2 SLJ are 0.8% and 6.4% in predicting the maximum failure load and the stiffness, respectively.

The failure mode of the PPA-G2 is mixed-mode failure. The fracture process observed in the PPA-G2 model demonstrates variations that are distinctive to the ones observed in the PPA-G1 model. The initial cracks predominantly take place at the two ends of the adhesion interfaces to coalesce the initiation of the primary cracks. Simultaneously, minor discontinuous microcracks occur along the two adhesion interfaces and within the adhesive in the immediate vicinity of the interfaces due to the stochastic local stress concentrations induced by surface microroughness, as shown in Figure 5-8c.1. Consequently, a diagonal continuous crack coalesces within the adhesive at the right end of the overlap as the new primary crack, which is induced by the increased number of discontinues microcracks at the specific local regions, as shown in Figure 5-8c.2. With the increase of the external loading, the primary cracks propagate tortuously through the two interfaces and the discontinuous microcracks, towards the central region of the overlap, resulting in some residual adhesives discretely attached to some local regions on the surface of the debonded PPA adherends (areas A-D of Figure

5-8b). This is the same as the observations in the experiment results (area A of Figure 3-14). Finally, the primary cracks link up with some cracks within the adhesive layer in the middle region of the joint. Whilst, the diagonal continuous crack connects to some cracks at the top-right adhesion interface, leading to a complete fracture (Figure 5-8c.4 and Figure 5-8b). The number of the cracks in the PPA-G2 model is 16531, which is greater than that in the PPA-G1 model.

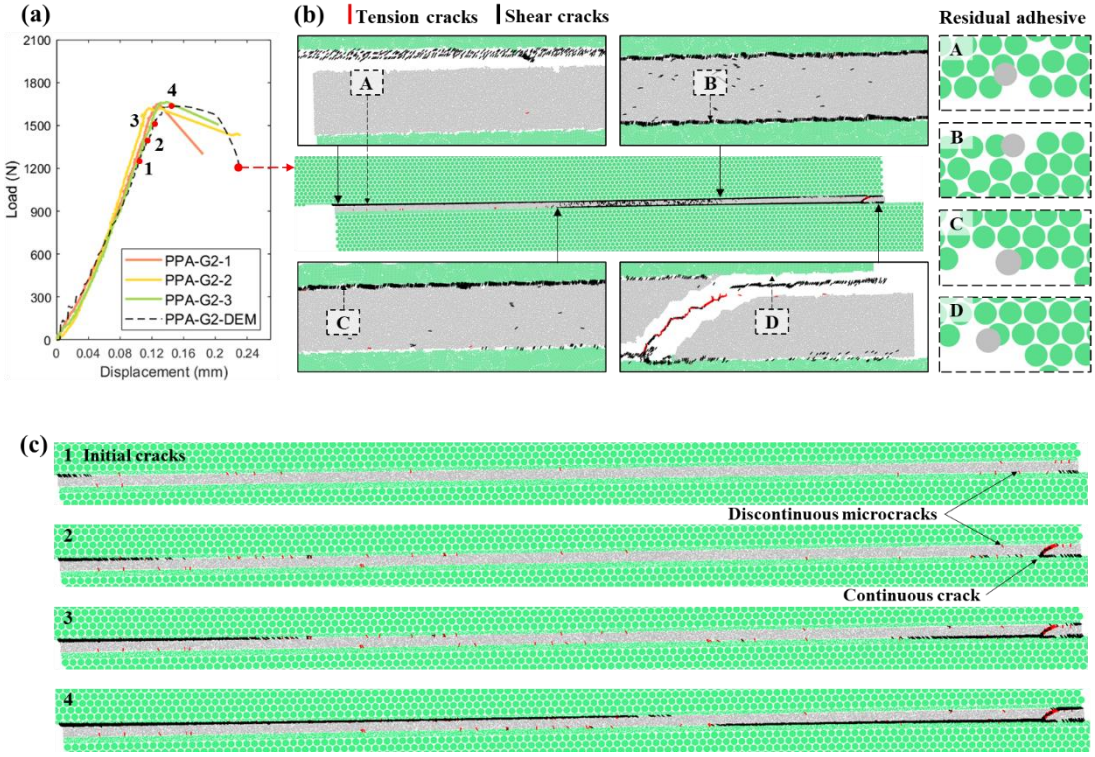

Figure 5-8. Load-displacement curves and fracture process of PPA-G2 SLJ. (a) Load-displacement curves of PPA-G2. (b) Numerical fracture result of PPA-G2. (c) Crack propagation of PPA-G2.

Figure 5-9 presents the deformation and fracture mechanisms of the PPA-G3 model. The maximum failure load and stiffness of the PPA-G3 model are 2072 N and 12779 N/mm, respectively. The errors between the numerical and experimental results of the PPA-G3 SLJ are 4.8% and 1.5% in predicting the maximum failure load and the stiffness, respectively.

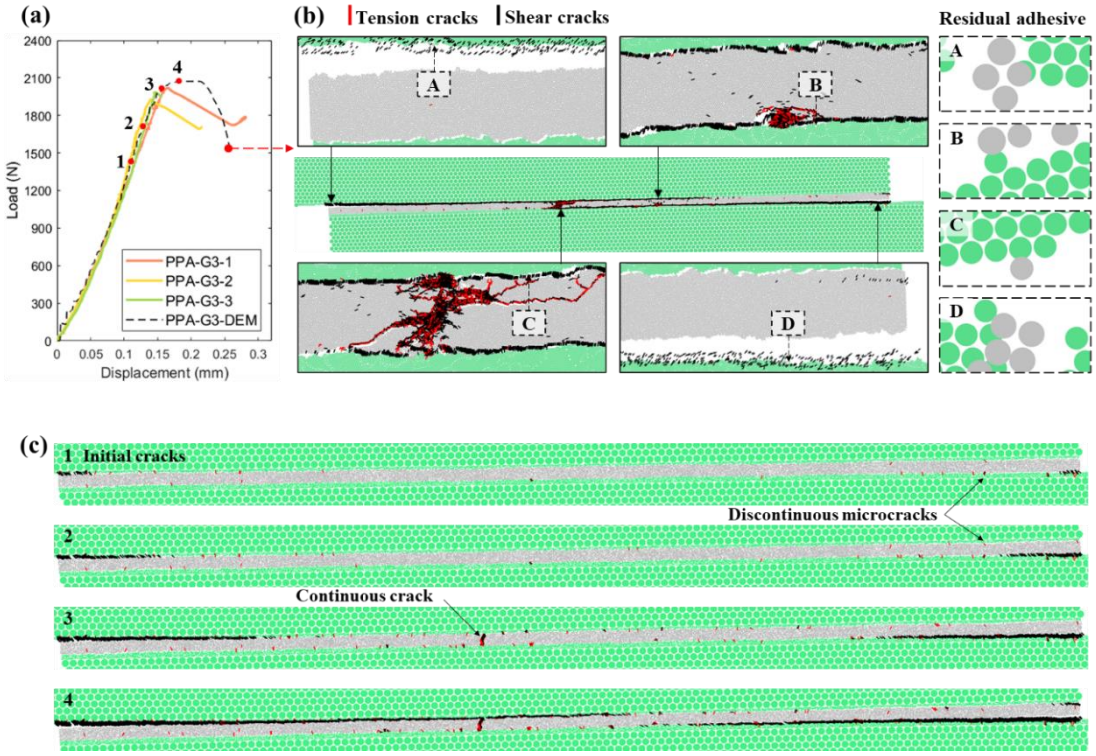

Figure 5-9. Load-displacement curves and fracture process of PPA-G3 SLJ. (a) Load-displacement curves of PPA-G3. (b) Numerical fracture result of PPA-G3. (c) Crack propagation of PPA-G3.

The failure mode of the PPA-G3 is mixed-mode failure. For the PPA-G3 model shown in Figure 5-9, the initial microcracks, primary cracks, and crack propagation are similar to those observed from the PPA-G2 model, but the position of the diagonal continuous crack within the adhesive layer is different due to the different surface profiles (Figure 5-9c.3). The initial primary cracks coalesce at the two ends of the adhesion interfaces, and the initial discontinuous microcracks also occur along the interfaces and within the adhesive in the immediate vicinity of the interfaces, as illustrated in Figure 5-9c.1. Then, the primary cracks propagate tortuously through the two interfaces and the discontinuous microcracks, towards the central region of the overlap. The primary cracks ultimately join together, whilst induce additional cracks within the adhesive layer (Figure 5-9b). Moreover, as shown in areas A-D of Figure 5-9b, the number of residual adhesives on the surface of the debonded PPA adherends

is greater than that of the PPA-G2 model (areas A-D of Figure 5-8b), which is also observed in the experiment (Figure 3-14). It is because there are increased discontinuous microcracks induced by more stochastic local stress concentrations due to the higher roughness grade of the PPA adherends. The number of the cracks in the PPA-G3 model is 24578, which is greater than that in both the PPA-G2 and PPA-G1 models.

5.3.3. Hybrid SLJ

Figure 5-10 presents the deformation and fracture mechanisms of the Hybrid-G1 model. The maximum failure load and stiffness of the Hybrid-G1 model are 1373 N and 18695 N/mm, respectively. The errors between the numerical and experimental results of the Hybrid-G1 SLJ are 4.6% and 4.2% in predicting the maximum failure load and the stiffness, respectively.

In the case of the Hybrid-G1 model, the failure mode involves pure adhesive failure. An initial primary crack coalesces at the right end of the adhesion interface on the loaded PPA adherend, as illustrated in Figure 5-10c.1. Subsequently, another primary crack coalesces at the left end of the same adhesion interface, as illustrated in Figure 5-10c.2. Eventually, these two primary cracks propagate along the interface of the PPA adherend and towards the central region, causing a complete fracture. The coalescence and propagation of all the cracks are only along the adhesion interface of the PPA adherend since the epoxy adhesive offers weaker adhesion to polymeric than metal substrate [103], resulting in a single-sided delamination of the joint (Figure 5-10b), which agrees with the experiment results (Figure 3-15). The number of the cracks in the Hybrid-G1 model is 6987.

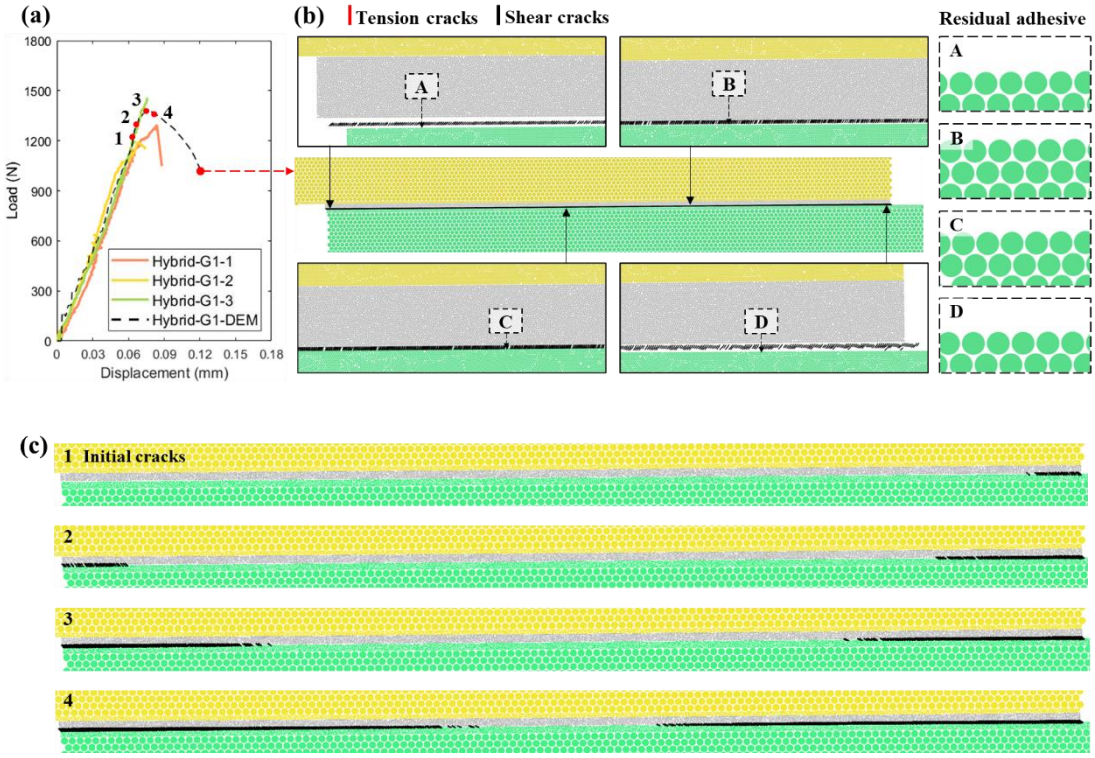

Figure 5-10. Load-displacement curves and fracture process of Hybrid-G1 SLJ. (a) Load-displacement curves of Hybrid-G1. (b) Numerical fracture result of Hybrid-G1. (c) Crack propagation of Hybrid-G1.

Figure 5-11 presents the deformation and fracture mechanisms of the Hybrid-G2 model. The maximum failure load and stiffness of the Hybrid-G2 model are 1930 N and 21763 N/mm, respectively. The errors between the numerical and experimental results of the Hybrid-G2 SLJ are 0.4% and 4.0% in predicting the maximum failure load and the stiffness, respectively.

The failure mode of the Hybrid-G2 model is characterized by predominant adhesive failure with additional localized cohesive failure. The fracture process of the Hybrid-G2 model differs slightly from that of the Hybrid-G1 model. An initial primary crack also coalesces at the right end of the interface on the loaded PPA adherend, while a limited number of discontinuous microcracks appear along the two interfaces and within the adhesive in the immediate vicinity of the interfaces due to the local stress concentrations induced by surface microroughness (Figure 5-11c.1). Then, another

primary crack coalesces at the left end of the same interface. These two primary cracks propagate tortuously through the interface of PPA adherend and the discontinuous microcracks, and towards the central region (Figure 5-11c.2 and 3). Finally, the primary cracks from both sides of the overlap region join together, along with two diagonal continuous cracks occurring in the adhesive layer, as illustrated in Figure 5-11c.4. The presence of the diagonal continuous cracks is also due to that the increased number of discontinues microcracks reduces the average distance between the two individual microcracks located on the opposite interfaces.

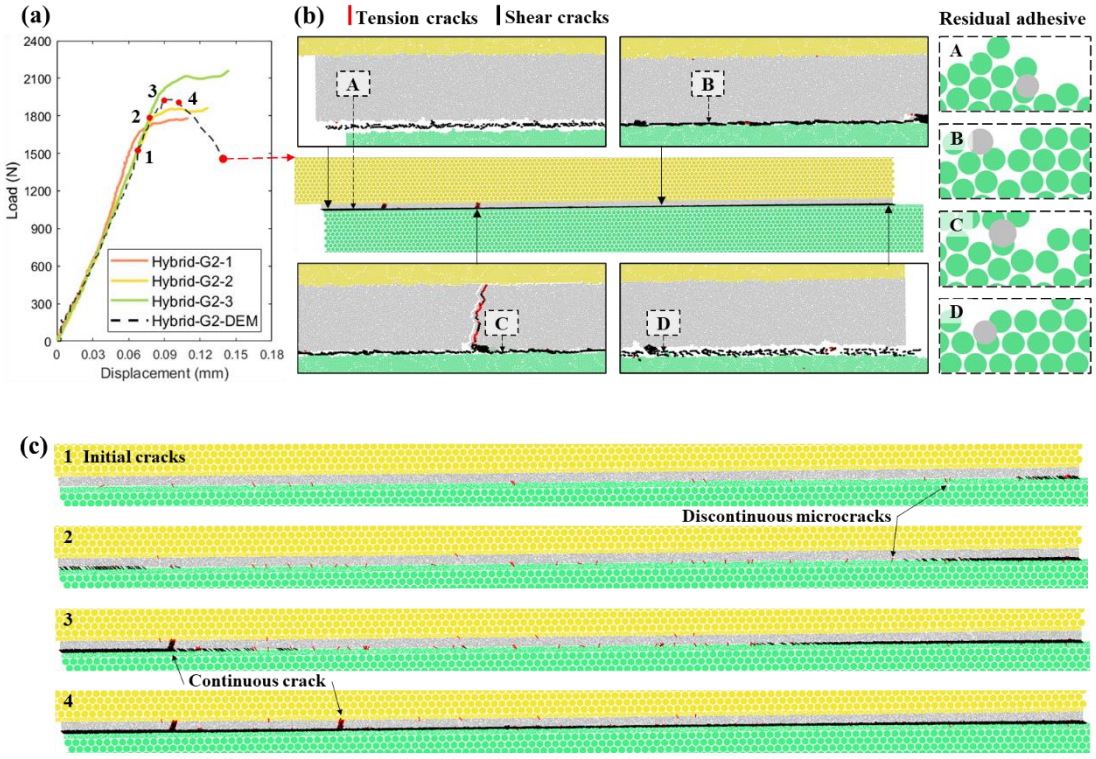

Figure 5-11. Load-displacement curves and fracture process of Hybrid-G2 SLJ. (a) Load-displacement curves of Hybrid-G2. (b) Numerical fracture result of Hybrid-G2. (c) Crack propagation of Hybrid-G2.

The fracture of the Hybrid-G2 model is a single-sided delamination of the joint with some residual adhesives discretely attached to some local regions on the surface of the debonded PPA adherend (areas A-D of Figure 5-11b), which is consistent with

the observation from the experiment results (area A of Figure 3-15). The number of the cracks in the Hybrid-G2 model is 12017, which is greater than that in the Hybrid-G1 model.

Figure 5-12 presents the deformation and fracture mechanisms of the Hybrid-G3 model. The maximum failure load and stiffness of the Hybrid-G3 model are 2313 N and 22714 N/mm, respectively. The errors between the numerical and experimental results of the Hybrid-G3 SLJ are 0.4% and 2.2% in predicting the maximum failure load and the stiffness, respectively.

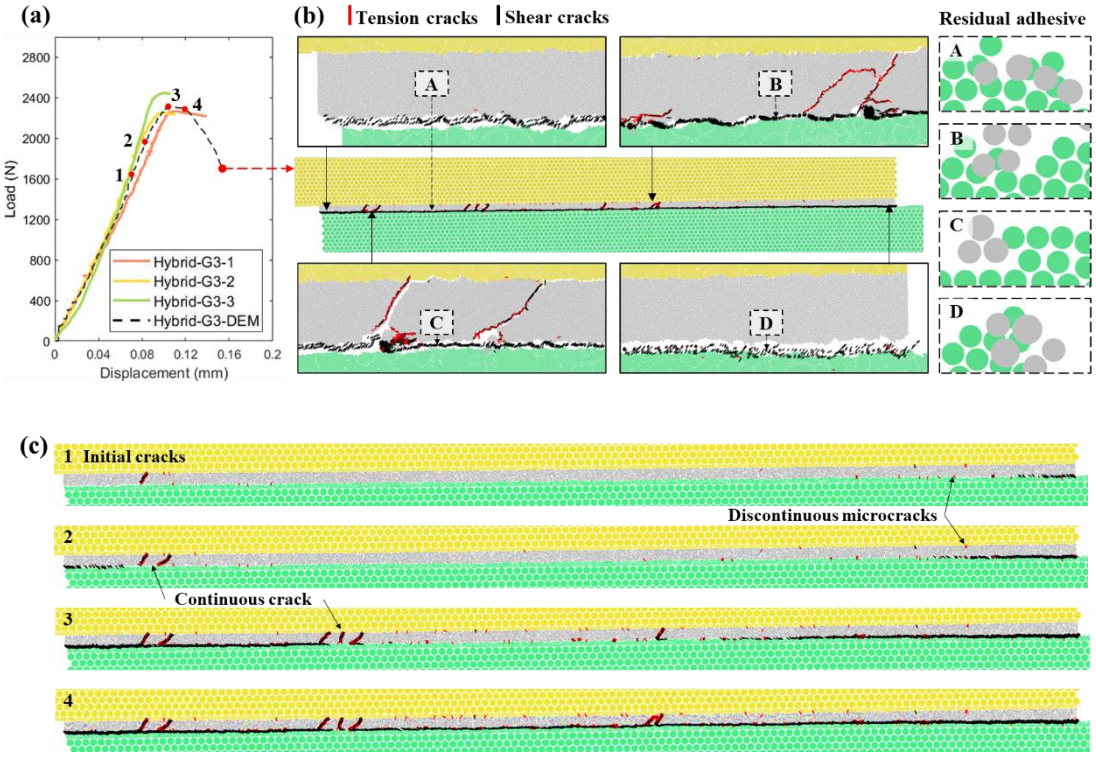

Figure 5-12. Load-displacement curves and fracture process of Hybrid-G3 SLJ. (a) Load-displacement curves of Hybrid-G3. (b) Numerical fracture result of Hybrid-G3. (c) Crack propagation of Hybrid-G3.

The failure mode of the Hybrid-G3 model is characterized by predominant adhesive failure with additional localized cohesive failure. Comparing the Hybrid-G3 model to the Hybrid-G2 model, the fracture processes of both are similar. Nevertheless,

an increased number of discontinuous microcracks emerge both at the initial stage of fracture and during the crack propagation, as depicted in Figure 5-12c.1 to 4, due to more stochastic local stress concentrations resulting from the higher roughness grades of the PPA and Al adherends. As a result, the quantity of the diagonal continuous cracks within the adhesive is greater, along with an increased presence of residual adhesives attached to the surface of the debonded PPA adherend (areas A-D of Figure 5-12b), which is in line with the experimental results in (area B of Figure 3-15). The number of the cracks in the Hybrid-G3 model is 17456, which is greater than that in both the Hybrid-G2 and Hybrid-G1 models.

5.4 Discussion

As presented in Table 5-3, the predicted numerical results demonstrate that the strength and the stiffness of the Al-Al SLJ, the PPA-PPA SLJ, and the hybrid SLJ increase with higher roughness grades of the adherends, which is consistent with the experimental results. Comparing the Al-G3 model with both the Al-G1 model and the Al-G2 model, the respective increases of the maximum failure load are 25.1% and 3.4%, while the respective increases of the stiffness are 8.1% and 1.4%. Comparing the PPA-G3 model with both the PPA-G1 model and the PPA-G2 model, the respective increases of the maximum failure load are 70.3% and 26.9%, while the respective increases of the stiffness are 24.2% and 8.7%. Comparing the Hybrid-G3 model with both the Hybrid-G1 model and the Hybrid-G2 model, the respective increases of the maximum failure load are 68.5% and 19.8%, while the respective increases of the stiffness are 21.5% and 4.4%. It is noted that there is a positive correlation between the maximum failure load and the crack number for the same type SLJs. It is due to that more bonds participate in the fracture process and more energy is needed to form cracks.

Table 5-3. Numerical results of each subtype of SLJ model.

Model type	Model subtype	Ave max failure load (N)	Ave stiffness (N/mm)	Crack number
Al-Al SLJ	Al-G1	2941	50808	14798
	Al-G2	3557	54145	16343
	Al-G3	3679	54924	19011
PPA-PPA SLJ	PPA-G1	1217	10289	10441
	PPA-G2	1633	11756	16531
	PPA-G3	2072	12779	24578
Hybrid SLJ	Hybrid-G1	1373	18695	6987
	Hybrid-G2	1930	21763	12017
	Hybrid-G3	2313	22714	17456

As shown in Table 5-1, the quantity of the bonds for the adhesion interfaces increases with the increase of the average roughness of adherend surface in the SLJ models. The increased interfacial bonds are equivalent to the increased contact area between adherend and adhesive, consequently improving the maximum failure load of the SLJs. According to the failure criteria of the determined linear parallel bond for the DEM SLJ models, the interfacial bonds between the adhesive and the adherend during compression develop a form of mechanical interlockings, as illustrated in Figure 5-13. A greater number of compressive interfacial bonds in SLJs with higher roughness grades can create stronger mechanical interlockings, thereby enhancing the strength of SLJs with higher roughness grades. Furthermore, the quantity of the residual adhesive observed in areas A-D, as illustrated in Figure 5-4b to Figure 5-12b, can validate this finding at microscale. Additionally, the mechanical interlockings may also prevent the adhesive from slipping along the interface. This is likely the reason for the increased stiffness of each type SLJs with higher roughness profiles of the adherends.

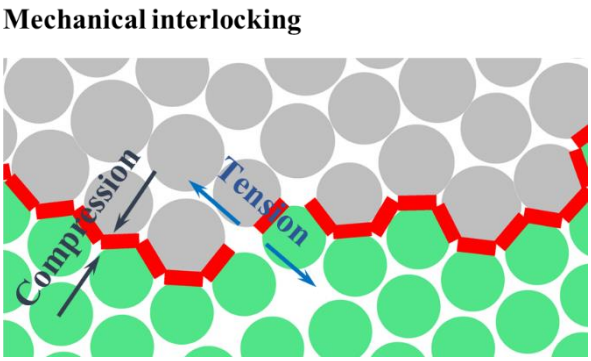

Figure 5-13. Microscale mechanical interlocking in DEM SLJ model.

The maximum failure load of the Al-Al SLJ is notably higher than that of both the PPA-PPA and the hybrid SLJ with the same roughness grade, although the average roughness of the Al adherend is lower than the PPA adherend. Additionally, the hybrid SLJ shows the second-highest maximum failure load. This may be explained by the criterion that requires a lower surface tension of adhesive compared to the adherend for good wetting of adhesion. The epoxy achieves excellent adhesion to metal, whilst offer weak adhesion to polymeric substrates [103]. Meanwhile, the stiffness of the adherend also plays a crucial role in determining the strength of the joints utilizing an epoxy adhesive. The increase of the stiffness could improve the joint strength [29]. At the same roughness grade across different types of SLJs, the PPA-PPA SLJs exhibit the largest deformation at failure, followed by the hybrid SLJs, due to the lower stiffness of the PPA material.

The fractures of the Al-G1, PPA-G1, and PPA-G2 models produce a double-sided delamination in contrast to the single-sided delamination observed in the experiments (Section 3.5). This may be attributed to the identical roughness profile applied to both the top and the bottom adherends for these models, while it is not achievable in experiments. The other factors include uncontrollable defects introduced in the process of applying the adhesive may also contribute to the difference between the fracture predicted by the numerical methods and observed from the experiments.

For each type DEM SLJ model, the discontinuous microcracks only appear along the interfaces and within the adhesive in the immediate vicinity of the interfaces for the SLJs with rough surface due to the stochastic local stress concentrations induced by the surface roughness. With higher roughness grades, the number of discontinuous microcracks increases due to more stochastic local stress concentrations, resulting in more residual adhesives attached to the surface of the debonded adherend. Additionally, the location and quantity of the discontinuous microcracks influence the coalescence, morphology, location, and quantity of the diagonal continuous cracks within the adhesive. The same type SLJs with a higher roughness grade requires a greater load to cause the initiation and coalescence of the primary cracks (as illustrated in the red points 1 of Figure 5-4a to Figure 5-12a). Furthermore, the stochastic local stress concentrations developed by the surface roughness influence the morphology, location, and propagation of the primary cracks, consequently resulting in the differences in the failure modes at microscale.

5.5 Conclusion

Based on the experimental results, this chapter conducts numerical investigations into the performance of Al-Al, PPA-PPA, and hybrid SLJs affected by microstructural surface roughness, focusing on the analysis of fracture mechanisms at microscale. The developed DEM models demonstrate efficacy and precision in predicting the strength and stiffness of multi-type SLJs with distinct microstructural roughness profiles, as well as in forecasting and capturing the failure modes at microscale, including the crack initiation, coalescence, and propagation within the adhesive and interfaces. Based on the analysis of the results, the following conclusions can be summarized:

- The predicted numerical results indicate that higher roughness grades of the adherends increase the strength and stiffness of the same type SLJs, exhibiting a greater presence of residual adhesives attached to the surface of the debonded adherend. Compared to the same roughness grade, the Al-Al SLJs manifest the highest strength and the hybrid SLJs show the second-highest strength. Furthermore, the PPA-PPA SLJs exhibit the largest deformation at failure, while the hybrid SLJs experience the second-largest deformation. These results are consistent with the experimental results presented in Chapter 3.
- Higher roughness grades of the joints induce more interfacial bonds at microscale, which are equivalent to the increased contact area between the adhesive and the adherend, thereby enhancing the strength of the SLJs. Furthermore, higher roughness grades of the joints also demonstrate more enhanced and effective microscale mechanical interlocking, consequently contributing to the improvement in both strength and stiffness of the SLJs.
- Microstructural roughness of the SLJs possesses the capability to influence the initiation, location, and quantity of the discontinuous microcracks along the adhesion interfaces and within the adhesive in the immediate vicinity of the interfaces, and further influence the coalescence, morphology, location, and quantity of the diagonal continuous cracks within the adhesive layer.
- Microstructural roughness of the SLJs also demonstrates the ability to mitigate the coalescence of the initial primary cracks, influence the morphology and location of the primary cracks as well as the propagation of the primary crack within the adhesive and interface, consequently resulting in the differences of the failure modes at microscale.

Chapter 6

6 Effect of microstructural defect on the performance and fracture mechanism of multi-type SLJs

6.1 Introduction

Although many previous studies have focused on the performance of adhesive joints with defects, there is still a lack of detailed investigations specifically into the fracture mechanisms at microscale. In practice, some defects in adhesive joints can be very small, ranging from a few microns to tens of microns in size [177, 178]. Considering the difficulties in precisely controlling the sizes and distributions of defects in experimental investigations for the SLJs, utilizing appropriate numerical methods, capable of precisely depicting microstructural defects and capturing micromechanical behaviors, are crucial to gain profound insights into the effect of defects on the performance and fracture mechanisms of adhesive joints. In FEM modelling, defects are typically introduced in the models by selectively removing elements from the adhesive layer, including strip defects [169, 179, 180] and circular defects [181, 182]. However, these numerical investigations generally focus on the macroscale defects, ranging from fractions of a millimeter to several millimeters.

Therefore, based on the experimental results, this chapter conducts numerical investigations into the effect of microstructural defects using multi-type adhesive SLJs with different interfacial adhesion. Specifically, this study examines how different densities and types of microstructural defects influence joint strength, crack initiation, coalescence, and propagation at microscale. Initially, the DEM model for the Al-Al SLJ, PPA-PPA SLJ, and hybrid SLJ, which incorporate the measured mean volume ratios of

the interfacial defects and the adhesive defects, are calibrated based on the experimental results of multi-type SLJs with G1 roughness. Subsequently, the Al-Al, PPA-PPA, and hybrid SLJ models incorporating different types and densities of microstructural defects are investigated. Finally, the performance and microscale fracture mechanism of three types of SLJs with different interfacial adhesion influenced by microstructural defects are examined.

6.2 Numerical modelling

6.2.1. Model configuration for the adherends, adhesive and defect

The numerical investigation of the effect of microstructural defects on the performance and fracture mechanisms of SLJs employs the DEM using the PFC 2D software package. An illustrative modelling process for the hybrid SLJ model is presented in Figure 6-1. The Al and PPA adherends are represented by yellow and green particles, respectively, and the epoxy adhesive is represented by grey particles. As demonstrated in Figure 6-1c.1, the Al and PPA adherends are divided into two regions characterized by two different particle sizes. The large adherend particles with a radius of 95.4 μm, are packed by a hexagonal arrangement. The radii of the small adherend and adhesive particles are 10.2 μm and 8.3-11 μm, respectively. In this study, the models generally comprise more than eight layers of the small adherend particles in the thickness direction. These layers are designed to establish a transition area between the large adherend particles and the adhesive particles, and to alleviate the non-uniform stress transmission caused by the different radii in the adherend particles. Additionally, the determined arrangement and size of the particles aim to optimize the number of total particles and computational costs. The contact model between the particles with the same properties is the soft bond model. The microparameters of the soft bond models

for the large adherend particles, small adherend particles, and adhesive particles are presented in Table 4-1, Table 4-3, and Table 4-10, respectively.

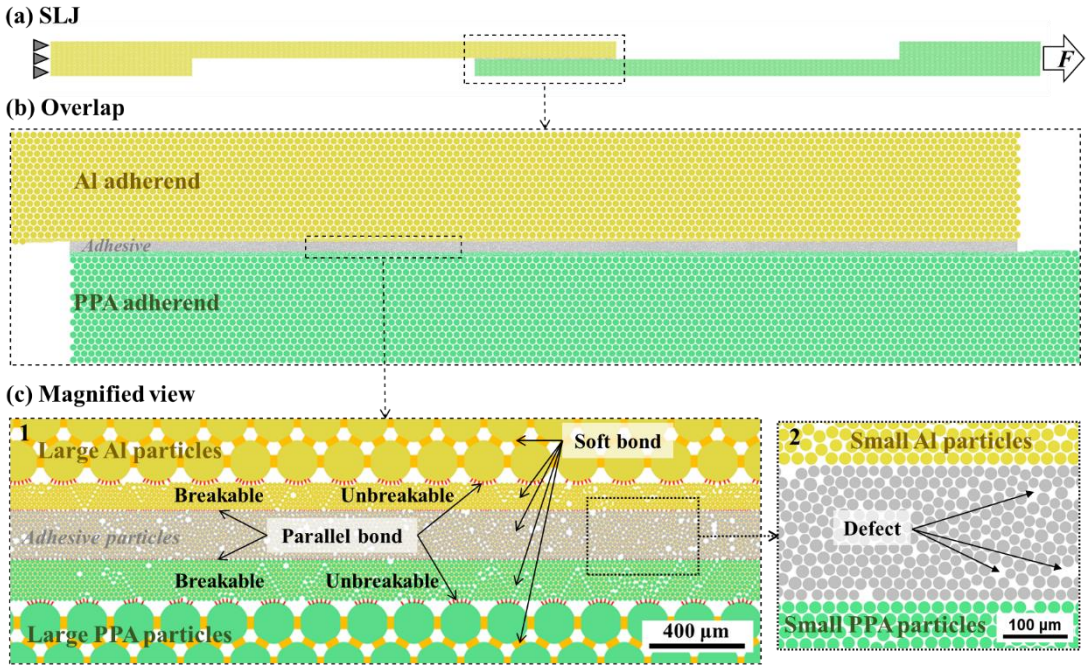

Figure 6-1. The arrangement of particles for SLJ with defects. (a) The entire structure of SLJ. (b) The overlap area of SLJ. (c) The particle composition, contact model and defect.

Figure 6-2a to Figure 6-2d illustrates the generation process of microstructural defects in the hybrid SLJ models, including both the interfacial and adhesive defects. Initially, the top Al adherend and bottom PPA adherend are positioned with a 0.2 mm gap (Figure 6-2a). Then, the adhesive particles are randomly seeded and expanded to the desired size to fill the space between the adherends (Figure 6-2b), forming the defect-free hybrid SLJ model. Finally, a specific number of the adhesive particles along the adhesion interface and within the adhesive layer is randomly selected (Figure 6-2c) and removed (Figure 6-2d) from Regions 1-4 (Figure 3-8) respectively, forming the hybrid SLJ model incorporating the interfacial and adhesive defects, according to the statistical analysis of the results of the CT scanning (Table 3-7). The modelling method

for the Al-Al and PPA-PPA SLJ models is similar to that of the hybrid SLJ model. In these models, the statistical data of microstructural defects obtained from Regions 1 and 3 (Figure 3-8) are used to develop the Al-Al SLJ model, while the statistical data from Regions 2 and 4 (Figure 3-8) are used for the PPA-PPA SLJ model.

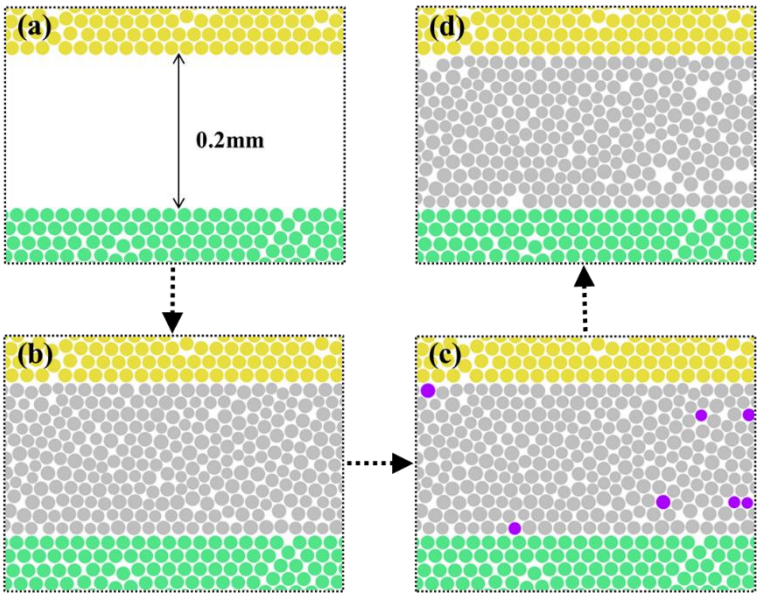

Figure 6-2. *Modelling process for hybrid SLJ with microstructural defects. (a) Placement of adherend. (b) Generation of adhesive. (c) Selection of adhesive particles. (d) Removed adhesive particles as defects*

6.2.2. Model configuration for the interfaces

The arrangement of the contact models between the particles is illustrated in Figure 6-1c.1. Due to the absence of adherend failure observed in the SLJ shear test, the contact model between the large and small adherend particles is defined using an unbreakable linear parallel bond model. The contact model for the adhesion interfaces between the small adherend and adhesive particles is defined using a breakable linear parallel bond model. The calibrated microparameters for the interfacial bonds are summarized in Table 6-1.

Table 6-1. The calibrated microparameters for the interfacial bonds.

Parameter	Description	Al adhesion interface	PPA adhesion interface
pb_kn	Normal stiffness (N/m^3)	3.55× 10^{11}	4.47 × 10^{10}
pb_ks	Shear stiffness (N/m^3)	2.98× 10^{11}	4.37 × 10^{10}
pb_ten	Tensile strength (Pa)	4.38 × 10^7	6.08 × 10^7
pb_coh	Cohesion (Pa)	4.83 × 10^6	1.44 × 10^6
pb_fa	Friction angle (˚)	14	14

6.3 Numerical results

For the three types of the DEM SLJ models, the defect-free model is labelled as *DF*. To investigate the effect of different types of microstructural defects on the performance and failure mechanisms of the SLJs, the models that incorporate only the interfacial defects and only the adhesive defects are labelled as *IM* and *AM*, respectively. The model incorporating both the interfacial defects and adhesive defects is labelled as *CM*. The mean defect volume ratios determined through CT scanning are used in each region of these models.

To further investigate the effect of increased defect density on the performance and failure mechanisms of the SLJs, the upper bounds (mean value plus standard deviation) of the measured defect volume ratios are used to develop the models. The models that incorporate only the interfacial defects and only the adhesive defects are labelled as *IS* and *AS*, respectively. The model incorporating both the interfacial defects and adhesive defects, is labelled as *CS*. The measured defect volume ratios used to develop the models are presented in Table 3-7. The notation of the SLJ models with defects is presented in Table 6-2. Since the interfacial adhesion between the PPA adherend and the adhesive is weaker than that between the Al adherend and the adhesive, this study classifies the PPA-PPA and the hybrid SLJ models as the SLJ with weaker

interfacial adhesion, while the Al-Al SLJ models are classified as the SLJ with stronger interfacial adhesion.

Table 6-2. Notation of SLJ model with defects.

Model	Defect type	Volume ratio
DF	/	/
AM	Adhesive defect	Mean
IM	Interfacial defect	Mean
CM	Adhesive and interfacial defect	Mean
AS	Adhesive defect	Mean+SD
IS	Interfacial defect	Mean+SD
CS	Adhesive and interfacial defect	Mean+SD

6.3.1. SLJ with weaker interfacial adhesion

6.3.1.1. PPA-PPA SLJ

Figure 6-3 presents the numerical calibration result of the *PPA-CM-1* incorporating both the mean value of the interfacial defects and adhesive defects. As shown in Figure 6-3a, the maximum failure load and stiffness of the *PPA-CM-1* with weaker interfacial adhesion are 1208 N and 9825 N/mm, respectively. The maximum failure load and stiffness of the *PPA-CM-1* show good agreement with the experimental results (PPA-G1 in Figure 3-14a and Table 3-9), with errors of 0.67% and 3.3%, respectively.

According to the fracture result shown in Figure 6-3b, the initial primary cracks in the *PPA-CM-1* resulting from the local stress concentrations only coalesce on the two adhesion interfaces located at the two ends of the overlap, and then continuously propagate along the interfaces towards the middle region of the joint until the total failure due to the relative weak interfacial adhesion. The fracture of the *PPA-CM-1*

exhibits a predominant adhesive failure mixed with minor microscale cohesive failure in the middle region of the overlap, showing a double-sided delamination. In contrast, the experiment shows a single-sided delamination of the PPA-G1 (Figure 3-14b). This difference can be attributed to the identical surface profile and interfacial defect volume ratio applied to both the top and the bottom adherends of the model, thereby resulting in an almost identical interfacial adhesion for the adherends, while it is unachievable in the experiment.

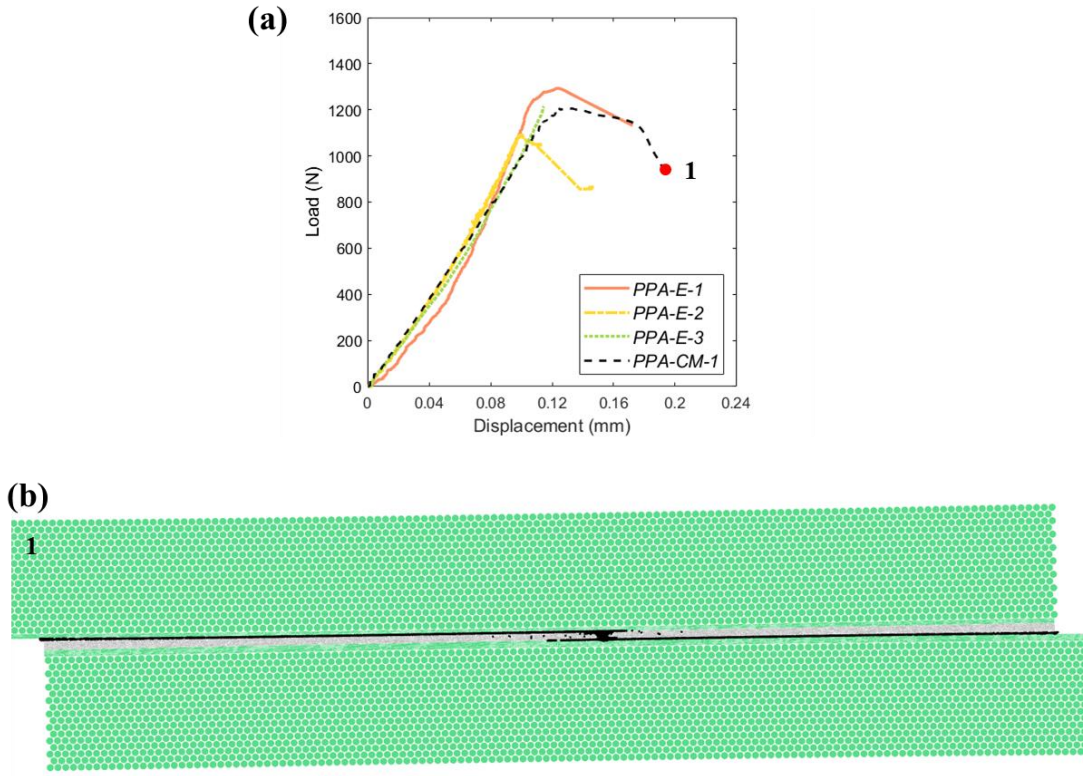

Figure 6-3. *Numerical calibrated results of the PPA-CM-1 model. (a) Load-displacement curves. (b) Numerical fracture results.*

To investigate the effect of different types and densities of microstructural defects on the PPA-PPA SLJ, different PPA-PPA SLJ models are developed. Each PPA-PPA SLJ model incorporating the same defect volume ratio and defect type, is generated and simulated 3 times by randomly distributing the defects in the desired regions. The stiffness of PPA-PPA SLJ models is minimally affected by defects, with a

maximum difference of 0.9% observed across the models. Figure 6-4 shows the average maximum failure loads of the PPA-PPA SLJ models with different defect characteristics, along with representative failed samples.

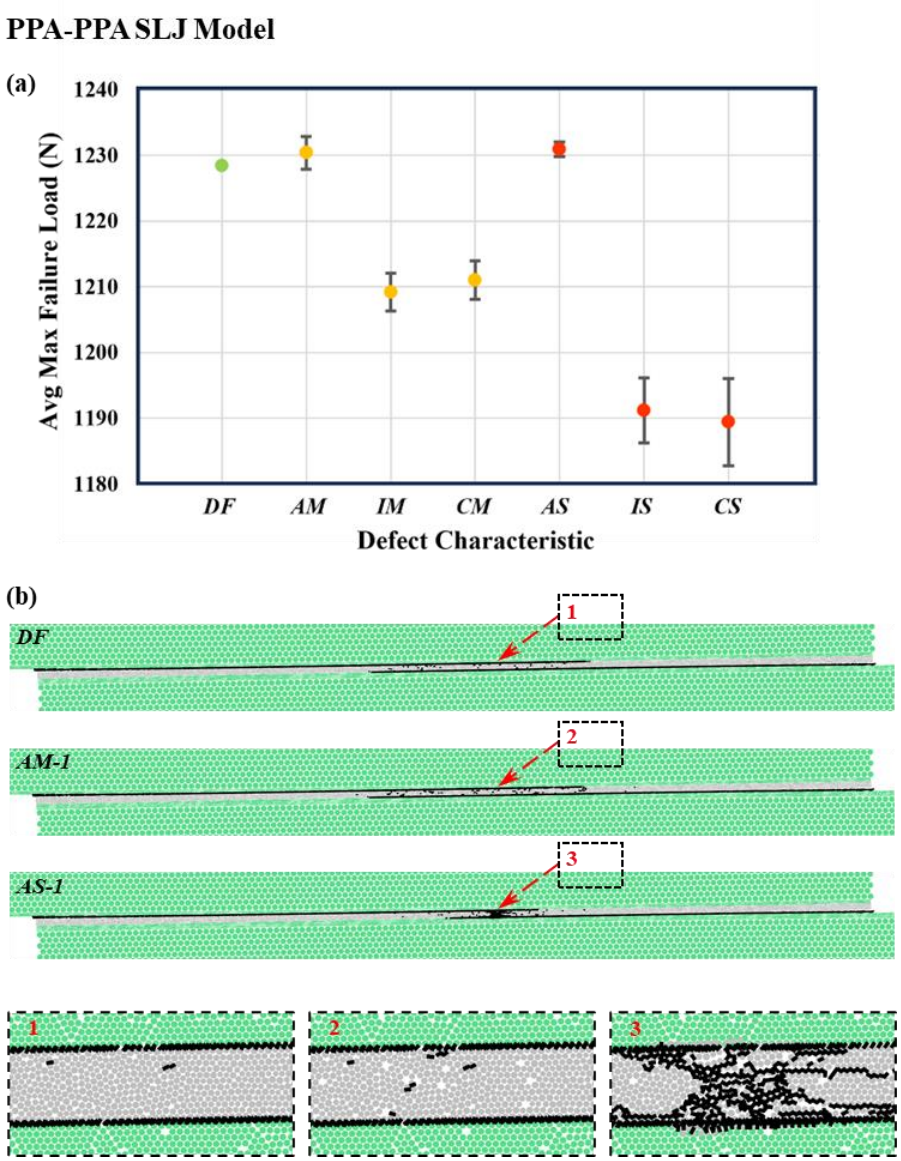

Figure 6-4. *Avg max failure loads of different PPA-PPA SLJ models and representative fracture. (a) Avg max failure loads. (b) Representative failed samples.*

As shown in Figure 6-4a, the coefficients of variation of the average maximum failure loads for all PPA-PPA SLJ models are less than 0.5%, indicating that the distribution of microstructural defects has a minimal effect on the strength of the PPA-

PPA SLJs. The minor variations can be mainly due to the randomness of microstructural defects. The average maximum failure loads of the *PPA-AM*, *PPA-AS*, and the *PPA-DF* are nearly the same, as the respective differences are less than 0.2%. Similarly, the maximum failure loads of the *PPA-IM* and *PPA-CM* are also close, with a difference of 0.15%, as well as of the *PPA-IS* and *PPA-CS* with a difference of 0.15%. Thus, the adhesive defects exert no significant effect on the strength of the PPA-PPA SLJs with the same density of the interfacial defects. This finding is consistent with the results in the study [89], which demonstrate that adhesive defects have a minor influence on the joint strength when the interfacial strength of the joints is insufficient.

Comparing the average maximum failure loads of the *PPA-IM* and the *PPA-IS* with that of the *PPA-DF*, they are decreased by 1.6% and 3%, respectively. It indicates that the interfacial defects dominantly affect the strength of the PPA-PPA SLJ. This is due to the presence of the interfacial defects that reduces the area of the intact interfacial bonds, thus inducing additional localized stress concentrations. This finding agrees with the results reported in the study [118]. The remaining interfacial bonds experience greater stresses, leading to a reduction in the overall interfacial strength of the PPA-PPA SLJ. An increased density of the interfacial defects further decreases the overall joint strength.

The fracture progresses of all the PPA-PPA SLJ models are generally similar to that of the *PPA-CM-1* (Figure 6-3b), including crack initiation, coalescence, and propagation. However, the presence of the adhesive defects may result in different crack coalescence and propagation in the middle region of the overlap for the PPA-PPA SLJ models. As shown in Figure 6-4b, the number of microcracks in the middle region of the overlap of the *PPA-AM-1* are greater than that observed in the *PPA-DF*, while the *PPA-AS-1* demonstrates an obvious cohesive failure at microscale and macroscale in

this region. This is because the random distribution of the adhesive defects induces stochastically localized stress concentrations in the adhesive layer and the associated localized weakening of the adhesive strength of the middle region.

Although the presence of the adhesive defects in the *PPA-AM-1* and the *PPA-AS-1* influences the macroscale and microscale fractures in the middle region of the overlap, the joint strength remains nearly equivalent to that of the *PPA-DF*. This is because all the models reach their maximum failure loads before the primary cracks propagate to the middle region, which explains the conclusion of research [88] at microscale. It states that defects located in the central portion of the overlap cause only a minor reduction in the overall fracture strength of joints.

6.3.1.2. Hybrid SLJ

Figure 6-5 presents the numerical calibration results of the *Hybrid-CM-1* incorporating both the mean value of the interfacial defects and adhesive defects. As shown in Figure 6-5a, the maximum failure load and stiffness of the *Hybrid-CM-1* with weaker interfacial adhesion are 1304 N and 17140 N/mm, respectively. The maximum failure load and stiffness of the *Hybrid-CM-1* show good agreement with the experimental results (Hybrid-G1 in Figure 3-15a and Table 3-10), with errors of 0.69% and 4.6%, respectively.

According to the fracture result shown in Figure 6-5b, one initial primary crack in the *Hybrid-CM-1* coalesces at the right end of the interface of the PPA adherend, which is followed by a new primary crack that develops at the left end of the same interface. These two primary cracks subsequently propagate along the interface of the PPA adherend, ultimately joining together to form the complete fracture. The fracture

of the *Hybrid-CM-1* exhibits pure adhesive failure, showing a single-sided delamination, which agrees with the-experimental observations (Figure 3-15b).

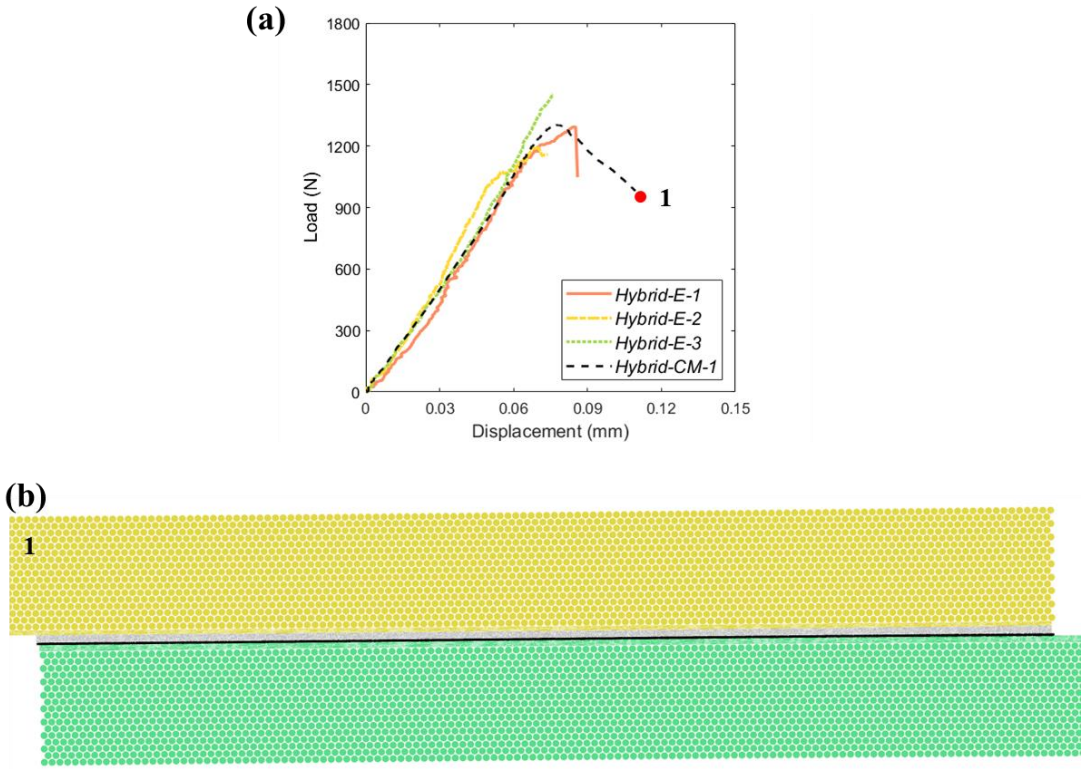

Figure 6-5. *Numerical calibrated results of the Hybrid-CM-1 model. (a) Load-displacement curves. (b) Numerical fracture results.*

To investigate the effect of different types and densities of microstructural defects on the hybrid SLJ, different hybrid SLJ models are developed. Each hybrid SLJ model incorporating the same defect volume ratio and defect type, is generated and simulated 3 times by randomly distributing the defects in the desired regions. The stiffness of hybrid SLJ models is minimally affected by defects, with a maximum difference of 0.8% observed across the models. Figure 6-6 shows the average maximum failure loads of the hybrid SLJ models with different defect characteristics, along with representative failed samples.

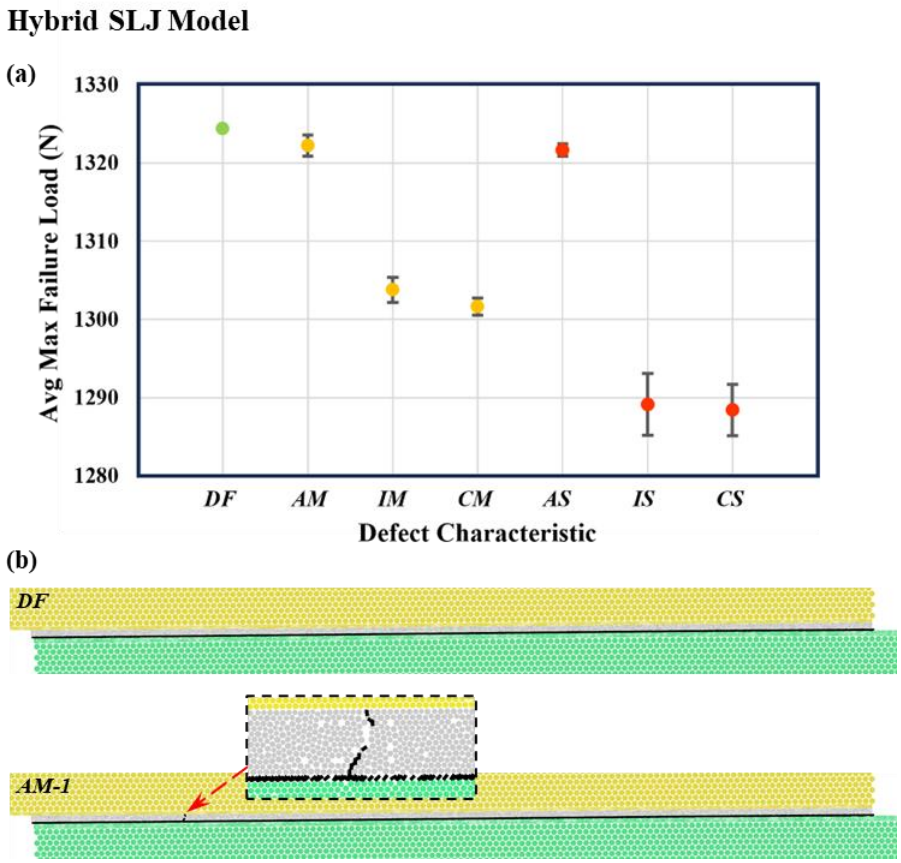

Figure 6-6. *Avg max failure loads of different hybrid SLJ models and representative fracture. (a) Avg max failure loads. (b) Representative failed samples.*

As shown in Figure 6-6a, the coefficients of variation of the average maximum failure loads for all hybrid SLJ models are less than 0.3%, indicating that the distribution of defects has a minimal effect on the strength of the hybrid SLJs. The average maximum failure loads of the *Hybrid-AM*, the *Hybrid-AS*, and the *Hybrid-DF* are almost the same, with a maximum difference of 0.21%. The average maximum failure loads of the *Hybrid-IM* and the *Hybrid-CM* are also very close, with a difference of 0.23%. The same observation applies to the *Hybrid-IS* and the *Hybrid-CS*, with a difference of 0.13%. These results confirm that the adhesive defects have no significant impact on the strength of the hybrid SLJs, consistent with findings from the PPA-PPA SLJ models. Comparing the *Hybrid-IM* and *Hybrid-IS* with the *Hybrid-DF*, the maximum failure loads are decreased by 1.7% and 2.7%, respectively. As shown in

Figure 6-6b, the fracture progresses of all hybrid SLJ models are generally similar to that of *Hybrid-CM-1* (Figure 6-5b). Since no cracks occur on the adhesion interface of the Al adherend, the interfacial defects on the PPA interface, where this interface coincides with the primary fracture path, are the sole factor dominantly influencing the strength of the hybrid SLJs. The presence of the interfacial defects on the PPA interface in the hybrid SLJs reduces their overall interfacial strength, similar to the effect of the interfacial defects on the PPA-PPA SLJs.

Additionally, the presence of the adhesive defects may contribute to the differences of localized cohesive cracks in the hybrid SLJ models. The representative fracture results of the *Hybrid-DF* and *Hybrid-AM-1* models are shown in Figure 6-6b. In the *Hybrid-AM-1*, there are microcracks propagating into the adhesive layer compared to that of the *Hybrid-DF*. Although the presence of localized cohesive failure in the *Hybrid-AM-1*, the overall joint strength remains equivalent to that of the *Hybrid-DF*. These findings are similar to the observations in the PPA-PPA SLJ models.

6.3.2. SLJ with stronger interfacial adhesion (Al-Al SLJ)

Figure 6-7 presents the numerical calibration results of the *Al-CM-1* incorporating both the mean value of the interfacial defects and adhesive defects. As shown in Figure 6-7a, the maximum failure load and stiffness of the *Al-CM-1* with stronger interfacial adhesion are 3018 N and 48210 N/mm, respectively. The maximum failure load and stiffness of the *Al-CM-1* show good agreement with the experimental results (Al-G1 in Figure 3-12a and Table 3-8), with errors of 0.94% and 1.9%, respectively.

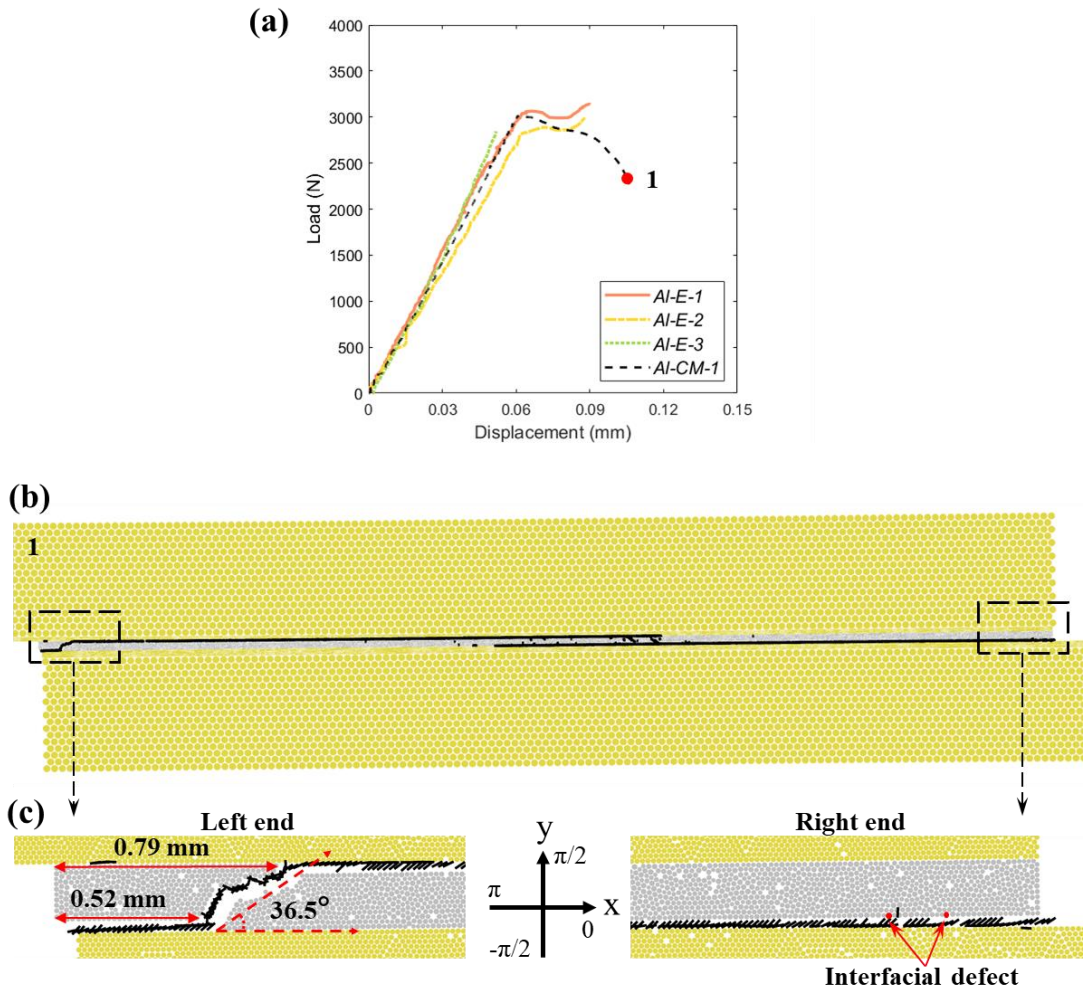

Figure 6-7. *Numerical calibrated results of the Al-CM-1 model. (a) Load-displacement curves. (b) Numerical fracture results. (c) Magnified view.*

According to the fracture result shown in Figure 6-7b and Figure 6-7c, the left primary crack in the *AL-CM-1* initially coalescing within the adhesive is diagonal due to the stronger interfacial adhesion, while the right primary crack only coalesces at the interface due to the greater presence of the interfacial defects at the right end. These two primary cracks propagate quickly along the adhesion interfaces towards the middle region of the joint, causing the complete fracture. The fracture of the *Al-CM-1* exhibits mixed mode failure with both adhesive and cohesive failure, also showing a double-sided delamination. In contrast, the experiment shows a single-sided delamination of

the Al-G1 (Figure 3-12b). The reason can be the same to the finding for the *PPA-CM-1*.

As shown in Figure 6-7c, the length of the residual adhesive on the surface of the debonded Al adherend along the x direction (loading direction) ranges from 0.52 mm to 0.79 mm, which is in the range observed in the experiments (areas 1 and 2 of Figure 3-12). The approximate angle between the diagonal cracks within the adhesive layer and the loaded Al adherend is 36.5 degrees, which is similar to the observation in the experiments (areas 1 and 2 of Figure 3-12). Before the crack initiation in the *Al-CM-1*, at a displacement of 0.041 mm, the directions of the maximum principal stress of 100 randomly selected adhesive particles at the left end are calculated and summarized. The results show that the directions of maximum principal stress range from 100 to 133.6 degrees, and from -43.5 to -15.3 degrees in 39% and 61% adhesive particles, respectively. The approximate angles of the diagonal cracks within the brittle adhesive and the directions of the maximum principal stress of the particles satisfy the maximum principal stress criterion of fracture, *i.e.*, cracks in brittle material grow perpendicular to the maximum principal stress [183].

To investigate the effect of different types and densities of microstructural defects on the Al-Al SLJ, different Al-Al SLJ models are developed. Each Al-Al SLJ model incorporating the same defect volume ratio and defect type, is generated and simulated 5 times by randomly distributing defects in the desired regions. The stiffness of Al-Al SLJ models is minimally affected by defects, with a maximum difference of 0.8% observed across the models. Figure 6-8 shows the average maximum failure loads of the Al-Al SLJ models with different defect characteristics. It is noted that the standard deviations of the average maximum failure loads observed in the Al-Al SLJ models incorporating defects are generally larger compared to those of the PPA-PPA and hybrid

SLJ models. The maximum coefficient of variations of the average maximum failure loads is up to 2.6%, indicating that the distribution of defects affects the strength of Al-Al SLJs.

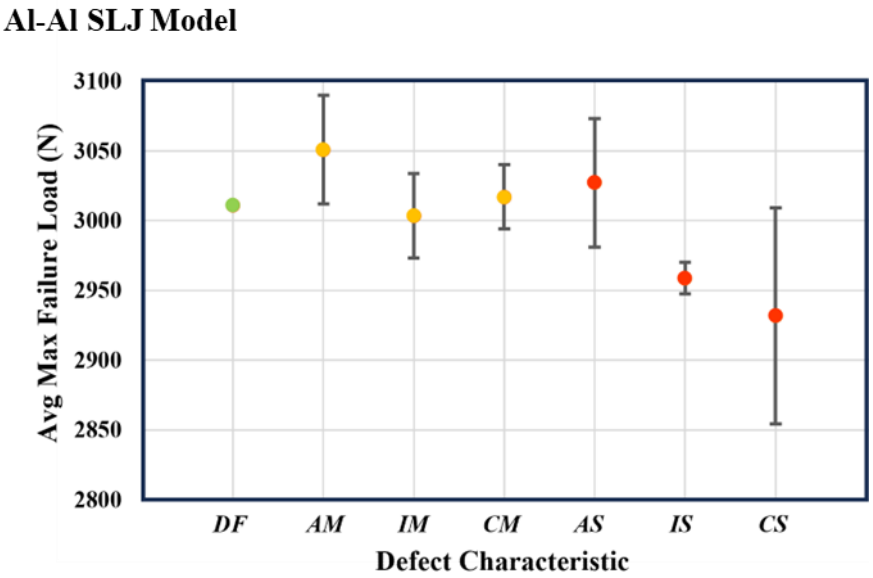

Figure 6-8. *Avg max failure loads of different Al-Al SLJ models.*

To further investigate the effect of the interfacial defects and adhesive defects, representative numerical results of the Al-Al SLJ models are illustrated in Figure 6-9. The approximate lengths and angles of the diagonal cracks within the adhesive layer of these models are summarized in Table 6-3. Except that some variations of fractures are observed at the two ends and in the middle region of the overlap, the overall fracture pattern of all the Al-Al SLJ models is almost identical. The interfacial and adhesive defects likely contribute to the different fractures at both ends, which are shown by the red points in Figure 6-9b. For the *Al-AM-1*, *Al-AM-2*, and *Al-AS-1* that show nearly identical microscale fractures at the two ends of the overlap, it is observed that their maximum failure loads are almost the same, although the *Al-AM-1* and the *Al-AM-2* incorporate different distributions of the adhesive defects, and the *Al-AS-1* model has an increased density of the adhesive defects.

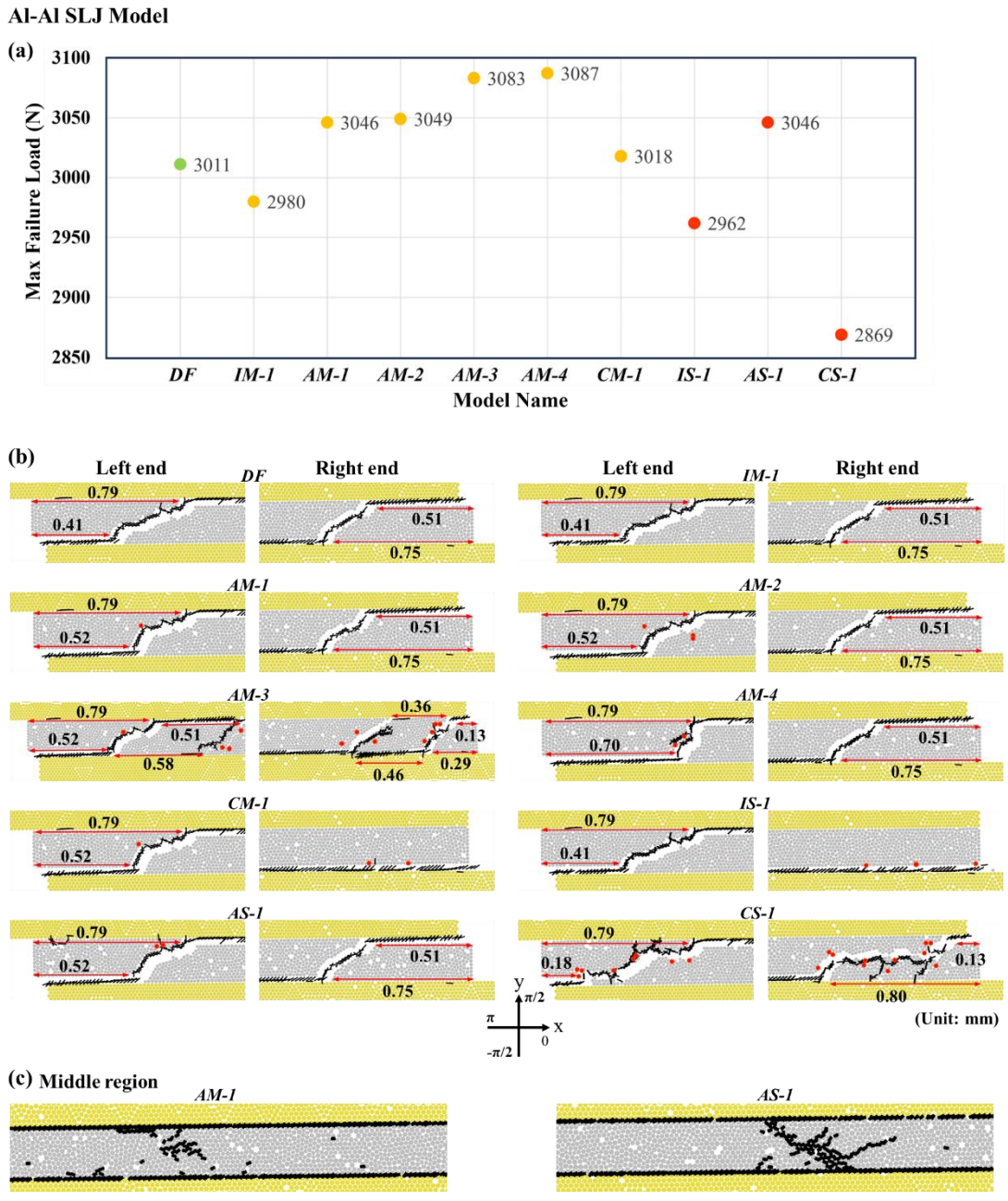

Figure 6-9. *Max failure load and fracture of representative Al-Al SLJ models. (a) Max failure load. (b) Fracture difference at the two ends. (c) Fracture difference in the middle region.*

Furthermore, comparing the *Al-AM-1* and *Al-AS-1*, although the adhesive defects in the middle region of the overlap affect the microcracks within the adhesive in this region (Figure 6-9c), they have no significant effect on the joint strength. This result is similar to the observations in the PPA-PPA and hybrid SLJ models.

Additionally, the fracture pattern at the two ends of the *Al-IM-1* and *Al-DF* is nearly identical, while the joint strength is decreased by 1.0%. This reduction is attributed to the decreased interfacial strength of the *Al-IM-1* induced by the interfacial defects.

Table 6-3. The characteristics of the diagonal crack within the adhesive layer.

Model	Crack length (mm)		Crack angle (°)	
	Left end	Right end	Left end	Right end
Al-DF	0.43	0.31	27.8	39.8
Al-IM-1	0.43	0.31	27.8	39.8
Al-AM-1	0.34	0.31	36.5	39.8
Al-AM-2	0.34	0.31	36.5	39.8
Al-AM-3	0.34&0.28	0.33&0.26	36.5&45.0	37.6&51.3
Al-AM-4	0.22	0.31	65.8	39.8
Al-CM-1	0.34	0	36.5	0
Al-IS-1	0.34	0	36.5	0
Al-AS-1	0.34	0.31	36.5	39.8
Al-CS-1	0.64	0.70	18.2	16.6

The diagonal cracks in all the models are the initial primary cracks, which subsequently propagate to the interfaces. Following the coalescence of these diagonal cracks within the adhesive layer, both mode I and mode II fractures coexist at the tips of the diagonal cracks, governing the stress fields near the crack tips [184, 185]. Within the framework of the linear elastic fracture mechanics [186], the stress field around the crack tip of a diagonal crack within the adhesive layer can be described based on a polar coordinate system, as illustrated in Figure 6-10.

Figure 6-10 indicates that the stress distributions around the diagonal crack tip are determined by the length of the diagonal crack l, the angle of the diagonal crack θ, as well as the distance r to the diagonal crack tips. In this study, the length of the diagonal crack within the adhesive layer decreases as the angle of the diagonal crack

increases since the thickness of the adhesive layer is a constant. Therefore, the analysis can focus exclusively on the angle of the diagonal crack as the primary factor.

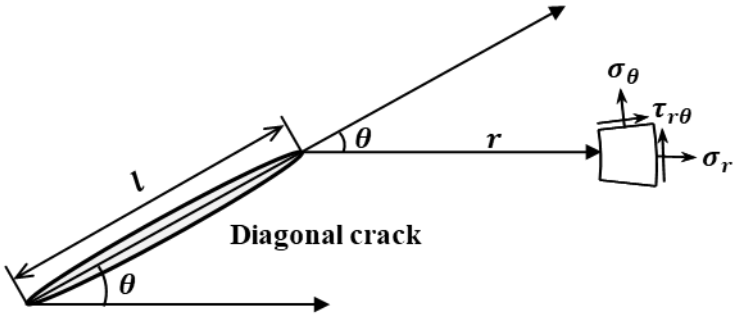

Figure 6-10. *Stress field around diagonal crack tip in a polar coordinate.*

Since the differences in the angle of the diagonal crack within the adhesive are induced by both the microscale interfacial and adhesive defects, the stress fields near the diagonal crack tips can vary significantly. However, the rapid and asynchronous propagation of the diagonal crack within the adhesive to the interfaces leads to the difficulties in acquiring a comparative analysis of the *Al-DF*, *Al-AM-1*, and *Al-AM-4*. To solve this issue and investigate the effect of different angles of the diagonal crack on the performance of the Al-Al SLJ, three models incorporating different pre-cracks between the chosen adhesive particles are developed based on the *Al-DF* by setting relevant bond strength to zero, as depicted in Figure 6-11a. Three types of pre-cracks are positioned within the adhesive at the left end of the overlap, originating from the same interfacial point 1 and extending to different interfacial points 2, 3, and 4, respectively. The angles between the three pre-cracks and the Al adherend are approximately 30, 60, and 90 degrees, respectively.

In all three models, the pre-crack firstly propagates to the interface on the right side of point 1 (as indicated by the arrows in Figure 6-11a), and then to the interface on the left side of points 2, 3, or 4. Therefore, considering the importance of the initiation

of the interfacial cracks, stress distributions of the ten adhesive particles at the right side of point 1 are analyzed, when the model is subjected to a displacement and a load of 0.041 mm and 2000 N (prior to pre-crack propagation), respectively. As shown in Figure 6-11b-d, the statistical results based on the ten adhesive particles show that the model with a 60-degree pre-crack experiences the largest σ_{xx}, while the model with a 30-degree pre-crack experiences the smallest σ_{xx}. The absolute value of σ_{xy} and σ_{yy} decrease as the pre-crack angle increases.

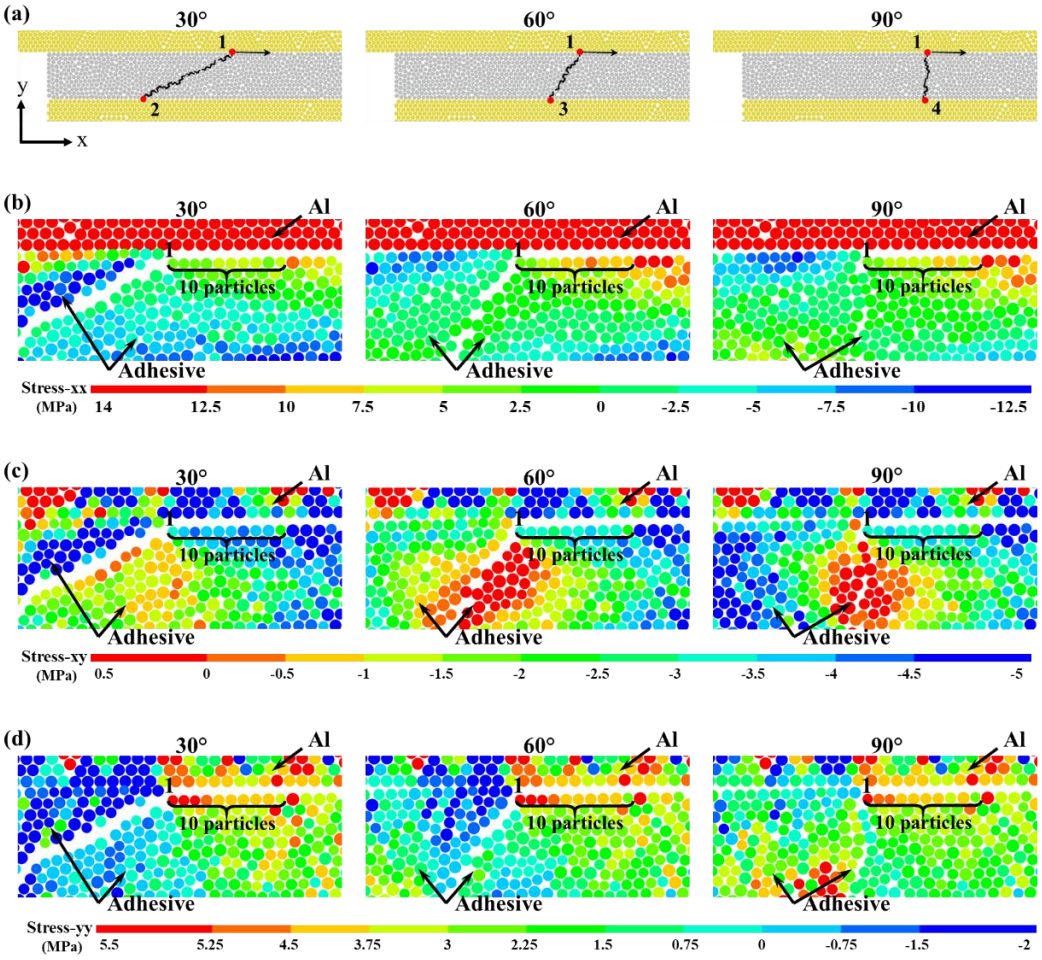

Figure 6-11. *Models with different pre-cracks and stress distributions around the pre-cracks. (a) Pre-crack type. (b) Stress-xx on particles. (c) Stress-xy on particles. (d) Stress-yy on particles.*

The different stress distributions caused by varying pre-crack conditions can affect the force conditions of the contact bond. Therefore, the force conditions of the ten interfacial bonds on the right side of point 1 are analyzed in the local coordinate system of each bond. As shown in Figure 6-12a, the absolute value of both the average tension and the average shear forces of the ten interfacial bonds decreases with the increase of the angle of the pre-cracks. Moreover, it is noted that the maximum failure load of the models increases with the increase of the angle of the pre-cracks (Figure 6-12b). Thus, a diagonal crack with a larger angle within the adhesive layer can significantly reduce the force at the interfaces near the crack tips, thereby mitigating the propagation of the diagonal crack toward the interfaces and enhancing the overall joint strength.

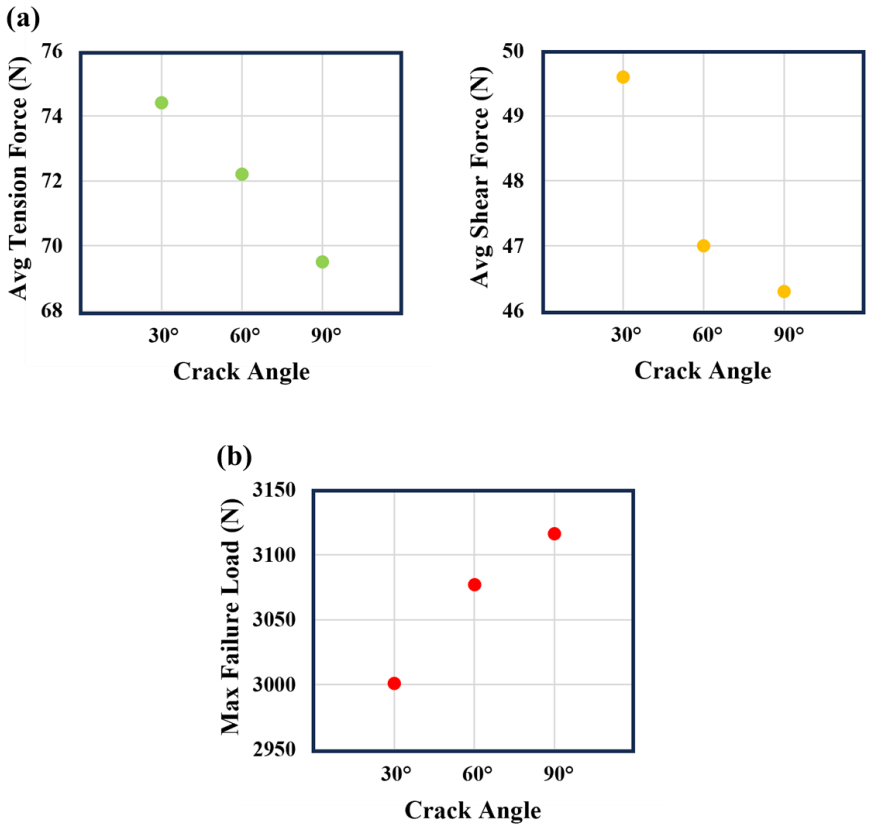

Figure 6-12. *Analysis of the interfacial bonds and joint strength. (a) Force condition of the analysed interfacial bonds. (b) Max failure load of the overall joints.*

Comparing the *Al-AM-3* with the *Al-AM-2*, the maximum failure load increases by 1.1% (Figure 6-9a). The number of the diagonal cracks within the adhesive at the two ends doubles in the *Al-AM-3*, resulting from the different defect distributions (Figure 6-9b). To investigate the effect of the additional diagonal cracks on the joint performance, the forces acting on the interfacial bonds around the diagonal cracks are investigated in the local coordinate system when the displacement of the models is 0.055mm, as illustrated in Figure 6-13.

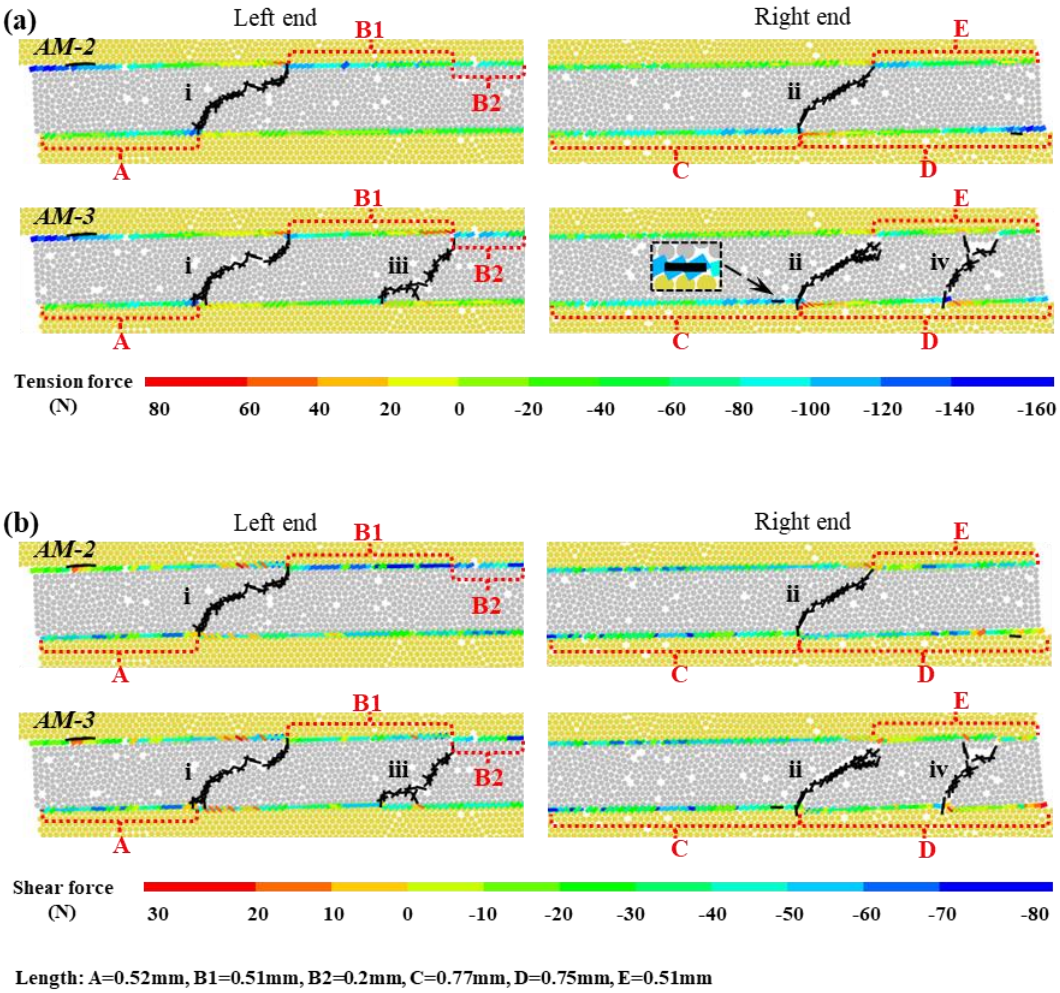

Figure 6-13. *Force distributions on the interfacial bonds. (a) Distribution of tension force. (b) Distribution of shear force.*

It is observed that, due to the effect of the additional diagonal cracks (cracks iii and crack iv) within the adhesive layer, the stresses in tension and shear for the

interfacial bonds of the *Al-AM-3* are altered and redistributed, compared to those of the *Al-AM-2*. As shown in Figure 6-13a, at the left end, all the interfacial bonds in section B1 of the *Al-AM-2* are subjected to tension. In contrast, some interfacial bonds in section B1 of the *Al-AM-3* are under compression, and tensile stress on the other interfacial bonds decreases by 36%. The tensile stress on the interfacial bonds in section B2 of the *Al-AM-3* increases by 33%. As shown in Figure 6-13b, the shear stress on the interfacial bonds in sections B1 and B2 decreases by 26% and 22% for the *Al-AM-3*, respectively. Due to the alleviation and transfer of the stresses on the interfacial bonds in section B1 of the *Al-AM-3*, the initial coalescence of the interfacial cracks in section B1 is mitigated and transferred to section B2, thereby contributing to the increased joint strength.

At the right end, an interfacial crack emerges in section C of the *Al-AM-3* (Figure 6-13a). This is attributed to the slightly elevated stresses on the interfacial bonds in section C, induced by the minor variation in the angle of crack ii (Table 6-3). The smaller angle of crack ii contributes to a slight decrease in joint strength. The effect of crack iv at the right end is generally similar to that of crack iii at the left end. The variations in the stress distributions on the interfacial bonds can alter the crack path at the right end of the *Al-AM-3*, which can further contribute to the increased strength of the *Al-AM-3*.

The maximum failure loads of the *Al-CM-1* and *Al-DF* are nearly identical, although their macroscale and microscale fractures at the two ends demonstrate differences induced by the presence of defects in the *Al-CM-1* (Figure 6-9 and Table 6-3). In the *Al-CM-1*, the larger angle of the diagonal crack within the adhesive layer at the left end enhances joint strength, while the presence of the interfacial defects and the absence of the diagonal crack within the adhesive at the right end decrease the joint strength. Additionally, the maximum failure load of the *Al-IS-1* is decreased by 1.9%

compared to that of the *Al-CM-1* (Figure 6-9), resulting from the smaller angle of the diagonal crack within the adhesive at the left end (Table 6-3), as well as the increased presence of the interfacial defects. Among all the models in Figure 6-9, the *Al-CS-1* exhibits the lowest strength, decreased by 4.7% compared to the *Al-DF*. This is attributed to the smallest angle of the diagonal cracks within the adhesive layer at both ends, as well as the highest presence of the interfacial defects.

6.4 Conclusion

Based on the experimental results, this chapter conducts numerical investigations into the overall mechanical performance and fracture mechanisms of Al-Al, PPA-PPA, and hybrid SLJs affected by microstructural defects at microscale. The developed DEM models can describe the overall mechanical performance and capture the microscale fracture mechanisms of multi-type SLJs with different interfacial adhesion and failure modes, through realistically incorporating different types and densities of microstructural defects. Based on the analysis of the results, the key conclusions are summarized as follows:

- In all the SLJs, the adhesive defects can contribute to the increased microcracks within the adhesive and cohesive failures towards the end of the fracture process. This is because once the interfacial crack has propagated to a certain extent, the adhesive layer can experience higher stress concentrations due to the rotation of the SLJs and the effect of the adhesive defects. However, these differences in fractures do not significantly affect the joint strength, as the joints reach their maximum failure loads prior to the occurrence of these differences.

- In all the SLJs, the stiffness is minimally affected by microstructural defects. This can be because stiffness is primarily governed by the global elastic response of the joint, which is relatively insensitive to the localized effects of microstructural defects during the early stages of loading.
- In the SLJs with weaker interfacial adhesion, the distribution of microstructural defects has a minimal effect on the joint strength, as the failure is dominated by the integrity of the interfacial bonds. In contrast, in the SLJs with stronger interfacial adhesion, the distribution of microstructural defects, particularly at the overlap end, affects the joint strength.
- In the SLJs with weaker interfacial adhesion that exhibit predominantly adhesive failure or pure adhesive failure, the interfacial defects are the sole factor dominantly influencing the joint strength when the interface coincides with the primary fracture path. These interfacial defects reduce the area of the intact interfacial bonds and create localized stress concentrations, leading to a decrease in overall interfacial strength. With the increase of these interfacial defects, the joint strength decreases.
- In the SLJs with stronger interfacial adhesion that exhibit mixed-mode failure, both the interfacial defects and the adhesive defects can affect the initiation and coalescence of the primary cracks at the two ends of the overlap. Denser interfacial defects at the two ends tend to induce interfacial cracks, whereas denser adhesive defects at the two ends can influence the angles and numbers of the diagonal cracks within the adhesive. A larger angle and greater number of the diagonal cracks within the adhesive at the

two ends can mitigate and alter the crack propagation along the interfaces, respectively, thereby enhancing the strength of the joints.

Chapter 7

7 Conclusions and Future Works

7.1 Conclusions

This study aims to experimentally and numerically investigate the effect of the microstructural features of adhesive joints on their performance and fracture mechanisms at microscale. The key conclusions drawn from this study are summarized as follows:

Two adherend materials：6082-T6 aluminum and PPA reinforced with 50 % glass fiber (Grivory HTV-5H1) and one epoxy adhesive： Loctite EA 9497 are employed in this study. The mechanical properties of the Al adherend, PPA adherend adhesive, and three types of SLJ specimens (Al-AL SLJ, PPA-PPA SLJ, and hybrid SLJ) with three roughness grades are obtained through experimental investigations, according to relevant international standards. Additionally, through the SEM and microCT scanning, the microstructural surface roughness and internal defects are investigated on different adherend interfaces and specific regions within the adhesive layer, respectively. The microscale adhesion interfaces between the adhesive and adherend, featuring the three roughness grades, which highlights the robust bonding between the adhesive and adherend. Rougher surfaces of the adherend exhibit more pits and protrusions, which enlarge the contact area between the adherend and adhesive, and facilitate the penetration of adhesive. The volume ratios of the interfacial and adhesive defects across the four regions and the average equivalent radius of microstructural defects are statistically examined. Microstructural defects are more likely to occur within the adhesive layer than at the interface. The higher density of the interfacial

defects on the PPA adherend, compared to the Al adherend, can be attributed to the poorer wettability of the epoxy adhesive on the PPA material.

Numerical uniaxial tensile tests are conducted on the Al adherend, PPA adherend, and adhesive using the DEM models implemented in PFC software. The microparameters of the contact models for the adherends and adhesive particles in DEM models are calibrated. The numerical-experimental comparisons of the bulk properties of adherends and adhesive validate the accuracy of the calibrated microparameters and the determined contact models. The DEM models of the Al and PPA adherends can be divided into two regions with distinct particle sizes to enable the microstructure representation and reduce the computational cost. The minimum number of the adhesive particle layers along the smallest dimension of the adhesive is determined to be five. The microparameters of the contact model for the thin adhesive layer are refined, which can accurately replicate the cohesive properties of the thin adhesive layer in adhesive joints, including normal and tangential fracture strength, as well as normal and tangential fracture energy. Furthermore, the DEM DCB model, DEM ENF model, and DEM SLJ model are developed to demonstrate the accuracy and reliability of the refined microparameters in simulating mode I, mode II, and mixed-mode cohesive failures of the thin adhesive layer, through comparison with the experimental results.

This study conducts systematic experimental and numerical investigations into the performance of Al-Al, PPA-PPA, and hybrid SLJs affected by surface roughness, focusing on the analysis of fracture mechanisms at microscale. Based on the experimental results, the microparameters of the contact models for the Al-Al and PPA-PPA SLJ models with minimum roughness grades are calibrated respectively, which are assumed to be close to zero roughness. Then, the calibrated microparameters are applied to other DEM SLJ models with higher roughness grades by introducing real

microstructural roughness profiles measured by experiments. The developed DEM models demonstrate efficacy and precision in predicting the strength and stiffness of multi-type SLJs with distinct microstructural roughness profiles, as well as in forecasting and capturing the failure modes at microscale, including the crack initiation, coalescence, and propagation within the adhesive and interfaces. Based on the analysis of the experimental and numerical results of multi-type SLJs with different roughness grades, the following conclusions can be summarized.

- Both the experimental and predicted numerical results indicate that higher roughness grades of the adherends increase the strength and stiffness of the same type SLJs, exhibiting a greater presence of residual adhesives attached to the surface of the debonded adherend. Compared to the same roughness grade, the Al-Al SLJs manifest the highest strength and the hybrid SLJs show the second-highest strength. Furthermore, the PPA-PPA SLJs exhibit the largest deformation at failure, while the Hybrid SLJs experience the second-largest deformation.
- Higher roughness grades of the joints induce more interfacial bonds at microscale, which are equivalent to the increased contact area between the adhesive and the adherend, thereby enhancing the strength of the SLJs. Furthermore, higher roughness grades of the joints also demonstrate more enhanced and effective microscale mechanical interlocking, consequently contributing to the improvement in both strength and stiffness of the SLJs.
- Microstructural roughness of the SLJs possesses the capability to influence the initiation, location, and quantity of the discontinuous microcracks along the adhesion interfaces and within the adhesive in the immediate vicinity of

the interfaces, and further influence the coalescence, morphology, location, and quantity of the diagonal continuous cracks within the adhesive layer.

- Microstructural roughness of the SLJs also demonstrates the ability to mitigate the coalescence of the initial primary cracks, influence the morphology and location of the primary cracks as well as the propagation of the primary crack within the adhesive and interface, consequently resulting in the differences of the failure modes at microscale.

This study conducts both experimental and numerical investigations into the overall mechanical performance and fracture mechanisms of Al-Al, PPA-PPA and hybrid SLJs affected by microstructural defects at microscale. Initially, the microparameters of the contact models for the Al-Al, PPA-PPA, and hybrid SLJ models, which incorporate the measured mean volume ratios of the interfacial defects and the adhesive defects, are calibrated based on the experimental results. Subsequently, the calibrated microparameters are employed in other DEM SLJ models incorporating different types and densities of microstructural defects. The developed DEM models can predict the overall mechanical performance and capture the microscale fracture mechanisms of multi-type SLJs with different interfacial adhesion and failure modes, through realistically incorporating different types of microstructural defects. Based on the analysis of the relevant results, the key conclusions are summarized as follows:

- In all the SLJs, the adhesive defects can contribute to the increased microcracks within the adhesive and cohesive failures towards the end of the fracture process. This is because once the interfacial crack has propagated to a certain extent, the adhesive layer can experience higher stress concentrations due to the rotation of the SLJs and the effect of the adhesive defects. However, these differences in fractures do not significantly affect

the joint strength, as the joints reach their maximum failure loads prior to the occurrence of these differences.

- In all the SLJs, the stiffness is minimally affected by microstructural defects. This can be because stiffness is primarily governed by the global elastic response of the joint, which is relatively insensitive to the localized effects of microstructural defects during the early stages of loading.
- In the SLJs with weaker interfacial adhesion, the distribution of microstructural defects has a minimal effect on the joint strength, as the failure is dominated by the integrity of the interfacial bonds. In contrast, in the SLJs with stronger interfacial adhesion, the distribution of microstructural defects, particularly at the overlap end, affect the joint strength.
- In the SLJs with weaker interfacial adhesion that exhibit predominantly adhesive failure or pure adhesive failure, the interfacial defects are the sole factor dominantly influencing the joint strength when the interface coincides with the primary fracture path. These interfacial defects reduce the area of the intact interfacial bonds and create localized stress concentrations, leading to a decrease in overall interfacial strength. With the increase of these interfacial defects, the joint strength decreases.
- In the SLJs with stronger interfacial adhesion that exhibit mixed-mode failure, both the interfacial defects and the adhesive defects can affect the initiation and coalescence of the primary cracks at the two ends of the overlap. Denser interfacial defects at the two ends tend to induce interfacial cracks, whereas denser adhesive defects at the two ends can influence the angles and numbers of the diagonal cracks within the adhesive. A larger

angle and greater number of the diagonal cracks within the adhesive at the two ends can mitigate and alter the crack propagation along the interfaces, respectively, thereby enhancing the strength of the joints.

7.2 Future Works

Based on the work presented in this thesis, the developed 2D DEM models have demonstrated a strong capability in predicting the performance and capturing the fracture behavior of adhesive joints with the microstructures. It would be beneficial to extend the developed 2D DEM models to 3D, as this would allow for a more comprehensive and accurate investigation of the mechanical behaviour and failure mechanisms of adhesive joints.

The investigation of adhesive joints affected by the microstructures can incorporate data-driven approaches, which have seen rapid development in the field of fracture mechanics and offer promising tools for improving prediction accuracy and design efficiency.

Further numerical and experimental investigations can be carried out on SLJs with a wider range of surface roughness grades and appropriate roughness intervals, in order to determine the optimal roughness for the joint performance. Further numerical and experimental investigations can be carried out on adhesive joints with both controlled and randomly varying angles, positions, and numbers of pre-cracks to gain a better understanding of the effects of diagonal cracks (including their propagation and paths) on the joint performance.

More comprehensive studies can be conducted to explore the interaction effects among a broader set of design variables in SLJs and to systematically assess their sensitivity to the fracture process and overall mechanical performance.

Building upon the microscale experimental and numerical investigations presented in this study, the developed DEM-based simulation framework and the calibrated microparameters can be further extended to serve as a predictive tool for the design and optimization of adhesive joints in engineering structures. In future work, the DEM models and microstructural characterization methods will be refined and integrated into user-friendly simulation strategies or software modules that can assist engineers in selecting suitable joining parameters for adhesive joints.

References

[1] E. Star, Energy efficiency reduces industrial carbon emissions. https://www.energystar.gov/industrial_plants/decarbonizing_industry/energy_efficiency_reduces_industrial_carbon_emissions#:~:text=Most%20industrial%20greenhouse%20gas%20emissions,associated%20emissions%2C%20and%20energy%20costs. (Accessed May 21 2025).

[2] L.G. Anderson, Effects of using renewable fuels on vehicle emissions, Renewable and Sustainable Energy Reviews 47 (2015) 162-172.

[3] E. Parliament, Reducing car emissions: new CO2 targets for cars and vans explained, 2018. https://www.europarl.europa.eu/topics/en/article/20180920STO14027/reducing-car-emissions-new-co2-targets-for-cars-and-vans-explained#:~:text=The%20new%20legislation%20sets%20the,Council%2C%20before%20coming%20into%20force. (Accessed May 21 2025).

[4] L. Zhu, N. Li, P. Childs, Light-weighting in aerospace component and system design, Propulsion and Power Research 7(2) (2018) 103-119.

[5] E. Commission, Reducing emissions from the shipping sector. https://climate.ec.europa.eu/eu-action/transport/reducing-emissions-shipping-sector_en#:~:text=2023%20IMO%20greenhouse%20gas%20strategy&text=A%20trajectory%20has%20also%20been,transition%20leaving%20no%20one%20behind. (Accessed May 21 2025).

[6] H.C. Kim, T.J. Wallington, Life-cycle energy and greenhouse gas emission benefits of lightweighting in automobiles: review and harmonization, Environmental science & technology 47(12) (2013) 6089-6097.

[7] G. Ma, J. Wu, H. Yuan, Interfacial shear stress analysis in single-lap adhesive joints with similar and dissimilar adherends under dynamic loading, International Journal of Adhesion and Adhesives 111 (2021) 102953.

[8] J.M. Arenas, C. Alía, J.J. Narbón, R. Ocaña, C. González, Considerations for the industrial application of structural adhesive joints in the aluminium–composite material bonding, Composites Part B: Engineering 44(1) (2013) 417-423.

[9] F. Youd, Talking sealants with sunstar engineering: securing success, 2024. https://www.just-auto.com/interview/talking-sealants-with-sunstar-engineering-securing-success/. (Accessed May 21 2025).

[10] I. Aspin, Paste adhesives for bonding in aerospace applications, 2024. https://www.adhesivesmag.com/articles/101211-paste-adhesives-for-bonding-in-aerospace-applications. (Accessed May 21 2025).

[11] A. Pramanik, A. Basak, Y. Dong, P. Sarker, M. Uddin, G. Littlefair, A. Dixit, S. Chattopadhyaya, Joining of carbon fibre reinforced polymer (CFRP) composites and aluminium alloys–A review, Composites Part A: Applied Science and Manufacturing 101 (2017) 1-29.

[12] J. Ferreira, P. Reis, J. Costa, M. Richardson, Fatigue behaviour of composite adhesive lap joints, Composites science and technology 62(10-11) (2002) 1373-1379.

[13] C.V. Katsiropoulos, A. Chamos, K. Tserpes, S.G. Pantelakis, Fracture toughness and shear behavior of composite bonded joints based on a novel aerospace adhesive, Composites Part B: Engineering 43(2) (2012) 240-248.

[14] L.F. Da Silva, A. Öchsner, R.D. Adams, Handbook of adhesion technology, Springer Science & Business Media2011.

[15] R.a. Markets, Automotive adhesive market: trends, forecast and competitive analysis 2024. https://uk.finance.yahoo.com/news/automotive-adhesive-market-report-

2024-
140700621.html?guccounter=1&guce_referrer=aHR0cHM6Ly93d3cuZ29vZ2xlLmNvbS8&guce_referrer_sig=AQAAAKcA0E8ZIFYrXpApmf52o2_HLG4Lu3S74YVLynId6RPi_HefoaP. (Accessed May 21 2025).

[16] R. Nester, Aerospace adhesives. https://www.researchnester.com/blog/aerospace-marine-and-defense/aerospace-adhesives-bonding-aircraft-structures. (Accessed May 21 2025).

[17] O. Sayman, Elasto-plastic stress analysis in an adhesively bonded single-lap joint, Composites Part B: Engineering 43(2) (2012) 204-209.

[18] B. Zhao, Z.-H. Lu, A two-dimensional approach of single-lap adhesive bonded joints, Mechanics of Advanced Materials and Structures 16(2) (2009) 130-159.

[19] K. Shahin, G. Kember, F. Taheri, An asymptotic solution for evaluation of stresses in balanced and unbalanced adhesively bonded joints, Mechanics of Advanced Materials and Structures 15(2) (2008) 88-103.

[20] H. Ejaz, M.A. Awan, H. Muzzammil, M. Ullah, A. Akhavan-Safar, L. daSilva, A. Tanveer, Strength improvement/optimization methods in adhesively bonded joints: A comprehensive review of past and present techniques, Mechanics of Advanced Materials and Structures (2024) 1-29.

[21] N.M. Chowdhury, J. Wang, W.K. Chiu, P. Chang, Experimental and finite element studies of thin bonded and hybrid carbon fibre double lap joints used in aircraft structures, Composites Part B: Engineering 85 (2016) 233-242.

[22] J. Kupski, S.T. De Freitas, Design of adhesively bonded lap joints with laminated CFRP adherends: Review, challenges and new opportunities for aerospace structures, Composite Structures 268 (2021) 113923.

[23] A. Siddique, Z. Iqbal, Y. Nawab, K. Shaker, A review of joining techniques for thermoplastic composite materials, Journal of Thermoplastic Composite Materials 36(8) (2023) 3417-3454.

[24] F. Nakagawa, T. Sawa, Photoelastic thermal stress measurements in scarf adhesive joints under uniform temperature changes, Journal of adhesion science and technology 15(1) (2001) 119-135.

[25] L.F. Da Silva, R. Adams, Techniques to reduce the peel stresses in adhesive joints with composites, International Journal of Adhesion and Adhesives 27(3) (2007) 227-235.

[26] C. Wu, C. Chen, L. He, W. Yan, Comparison on damage tolerance of scarf and stepped-lap bonded composite joints under quasi-static loading, Composites Part B: Engineering 155 (2018) 19-30.

[27] L.F.M. da Silva, R.J.C. Carbas, G.W. Critchlow, M.A.V. Figueiredo, K. Brown, Effect of material, geometry, surface treatment and environment on the shear strength of single lap joints, International Journal of Adhesion and Adhesives 29(6) (2009) 621-632.

[28] A. Gacoin, P. Lestriez, J. Assih, A. Objois, Y. Delmas, Comparison between experimental and numerical study of the adhesively bonded scarf joint and double scarf joint: Influence of internal singularity created by geometry of the double scarf joint on the damage evolution, International journal of adhesion and adhesives 29(5) (2009) 572-579.

[29] P.N. Reis, J. Ferreira, F. Antunes, Effect of adherend's rigidity on the shear strength of single lap adhesive joints, International Journal of Adhesion and Adhesives 31(4) (2011) 193-201.

[30] F.A. Stuparu, D.A. Apostol, D.M. Constantinescu, C.R. Picu, M. Sandu, S. Sorohan, Cohesive and XFEM evaluation of adhesive failure for dissimilar single-lap joints, Procedia Structural Integrity 2 (2016) 316-325.

[31] R. Hazimeh, G. Challita, K. Khalil, R. Othman, Influence of dissimilar adherends on the stress distribution in adhesively bonded composite joints subjected to impact loadings, Mechanics of Composite Materials 50 (2015) 717-724.

[32] G. Sun, X. Liu, G. Zheng, Z. Gong, Q. Li, On fracture characteristics of adhesive joints with dissimilar materials–An experimental study using digital image correlation (DIC) technique, Composite structures 201 (2018) 1056-1075.

[33] L. Liao, T. Sawa, C. Huang, Experimental and FEM studies on mechanical properties of single-lap adhesive joint with dissimilar adherends subjected to impact tensile loadings, International Journal of Adhesion and Adhesives 44 (2013) 91-98.

[34] X. Zhang, Y. Ju, A. Zhu, T. Zou, Fatigue behavior of single-lap adhesive joints with similar and dissimilar adherends under cyclic loading: A combined experimental and simulation study, Materials Today Communications 37 (2023) 107215.

[35] P. Parkes, R. Butler, J. Meyer, A. De Oliveira, Static strength of metal-composite joints with penetrative reinforcement, Composite Structures 118 (2014) 250-256.

[36] W. Tu, P. Wen, P. Hogg, F. Guild, Optimisation of the protrusion geometry in Comeld™ joints, Composites Science and Technology 71(6) (2011) 868-876.

[37] E. Paroissien, F. Lachaud, S. Schwartz, A. Da Veiga, P. Barrière, Simplified stress analysis of hybrid (bolted/bonded) joints, International Journal of Adhesion and Adhesives 77 (2017) 183-197.

[38] F. Gamdani, R. Boukhili, A. Vadean, Tensile behavior of hybrid multi-bolted/bonded joints in composite laminates, International Journal of Adhesion and Adhesives 95 (2019) 102426.

[39] K. Yokozeki, K. Hisazumi, T. Vallée, T. Evers, T. Ummenhofer, J. Boretzki, M. Albiez, Hybrid joints consisting of pre-tensioned bolts and a bonded connection, Part II: Large-scale experiments, International Journal of Adhesion and Adhesives 128 (2024) 103523.

[40] P. Lopez-Cruz, J. Laliberté, L. Lessard, Investigation of bolted/bonded composite joint behaviour using design of experiments, Composite Structures 170 (2017) 192-201.

[41] Y. Chen, X. Yang, M. Li, K. Wei, S. Li, Mechanical behavior and progressive failure analysis of riveted, bonded and hybrid joints with CFRP-aluminum dissimilar materials, Thin-Walled Structures 139 (2019) 271-280.

[42] T. Sadowski, P. Golewski, E. Zarzeka-Raczkowska, Damage and failure processes of hybrid joints: Adhesive bonded aluminium plates reinforced by rivets, Computational Materials Science 50(4) (2011) 1256-1262.

[43] P. Chang, A. Mouritz, B. Cox, Properties and failure mechanisms of pinned composite lap joints in monotonic and cyclic tension, Composites Science and Technology 66(13) (2006) 2163-2176.

[44] S. Ucsnik, S. Stelzer, H. Sehrschön, G. Sieglhuber, Composite to composite joint with lightweight metal reinforcement for enhanced damage tolerance, ECCM16—16th European Conference on Composite Materials, Seville, Spain, 2014.

[45] W. Li, S. Guo, I.K. Giannopoulos, S. He, Y. Liu, Strength enhancement of bonded composite laminate joints reinforced by composite Pins, Composite Structures 236 (2020) 111916.

[46] A. Yousefi Kanani, S. Green, X. Hou, J. Ye, Hybrid and adhesively bonded joints with dissimilar adherends: a critical review, Journal of Adhesion Science and Technology 35(17) (2021) 1821-1859.

[47] S. Darwish, A. Ghanya, Critical assessment of weld-bonded technologies, Journal of Materials Processing Technology 105(3) (2000) 221-229.

[48] G. Marques, R. Campilho, F. Da Silva, R. Moreira, Adhesive selection for hybrid spot-welded/bonded single-lap joints: Experimentation and numerical analysis, Composites Part B: Engineering 84 (2016) 248-257.

[49] V.C. Beber, B. Schneider, Fatigue of structural adhesives under stress concentrations: Notch effect on fatigue strength, crack initiation and damage evolution, International Journal of Fatigue 140 (2020) 105824.

[50] T.S. Methfessel, C. El Yaakoubi-Mesbah, W. Becker, Failure analysis of crack-prone joints with Finite Fracture Mechanics using an advanced modeling approach for the adhesive layer, International Journal of Adhesion and Adhesives 130 (2024) 103608.

[51] J.A. Pascoe, N. Zavatta, E. Troiani, R. Alderliesten, The effect of bond-line thickness on fatigue crack growth rate in adhesively bonded joints, Engineering Fracture Mechanics 229 (2020) 106959.

[52] A. Qureshi, T. Guan, M. Alfano, Finite element analysis of crack propagation in adhesive joints with notched adherends, Materials 16(1) (2022) 391.

[53] Matt, An introduction to MS polymer sealants, 2022. (Accessed May 21 2025).

[54] S. Omairey, N. Jayasree, M. Kazilas, Defects and uncertainties of adhesively bonded composite joints, SN Applied Sciences 3(9) (2021) 769.

[55] H. Ren, X. Chen, Y. Chen, Aircraft reliability and maintainability analysis and design, Reliability Based Aircraft Maintenance Optimization and Applications (2017) 39-41.

[56] M.J. Davis, A. McGregor, Assessing adhesive bond failures: mixed-mode bond failures explained, ISASI Australian Safety Seminar, Canberra, 2010, pp. 4-6.

[57] S.M. Hasheminia, B.C. Park, H.-J. Chun, J.-C. Park, H.S. Chang, Failure mechanism of bonded joints with similar and dissimilar material, Composites Part B: Engineering 161 (2019) 702-709.

[58] X. Shang, E.A.S. Marques, J.J.M. Machado, R.J.C. Carbas, D. Jiang, L.F.M. da Silva, Review on techniques to improve the strength of adhesive joints with composite adherends, Composites Part B: Engineering 177 (2019) 107363.

[59] J. de Castro, T. Keller, Ductile double-lap joints from brittle GFRP laminates and ductile adhesives, Part I: Experimental investigation, Composites Part B: Engineering 39(2) (2008) 271-281.

[60] M.D. Banea, L.F.M. and da Silva, Mechanical Characterization of Flexible Adhesives, The Journal of Adhesion 85(4-5) (2009) 261-285.

[61] T. Yu, D. Fernando, J.G. Teng, X.L. Zhao, Experimental study on CFRP-to-steel bonded interfaces, Composites Part B: Engineering 43(5) (2012) 2279-2289.

[62] M.D. Banea, Influence of adherend properties on the strength of adhesively bonded joints, MRS Bulletin 44(8) (2019) 625-629.

[63] M.-G. Song, J.-H. Kweon, J.-H. Choi, J.-H. Byun, M.-H. Song, S.-J. Shin, T.-J. Lee, Effect of manufacturing methods on the shear strength of composite single-lap bonded joints, Composite Structures 92(9) (2010) 2194-2202.

[64] D. Gleich, M. Van Tooren, A. Beukers, Analysis and evaluation of bondline thickness effects on failure load in adhesively bonded structures, Journal of adhesion science and technology 15(9) (2001) 1091-1101.

[65] A. Biszczanik, K. Talaśka, D. Wilczyński, Analysis of the adhesive spread and the thickness of the adhesive bonded joint depending on the compressive force applied to bonded materials with different surface structure, International Journal of Adhesion and Adhesives 114 (2022) 103081.

[66] J.M. Arenas, J.J. Narbón, C. Alía, Optimum adhesive thickness in structural adhesives joints using statistical techniques based on Weibull distribution, International Journal of Adhesion and Adhesives 30(3) (2010) 160-165.

[67] R.D. Campilho, D. Moura, M.D. Banea, L.F.M. da Silva, Adhesive thickness effects of a ductile adhesive by optical measurement techniques, International journal of adhesion and adhesives 57 (2015) 125-132.

[68] X. Shang, E. Marques, J. Machado, R. Carbas, D. Jiang, L.F. Da Silva, Review on techniques to improve the strength of adhesive joints with composite adherends, Composites Part B: Engineering 177 (2019) 107363.

[69] M. Sandu, A. Sandu, D.M. Constantinescu, D.A. Apostol, Single-strap adhesively bonded joints with square or tapered adherends in tensile test conditions, International Journal of Adhesion and Adhesives 44 (2013) 105-114.

[70] M. You, Z.-M. Yan, X.-L. Zheng, H.-Z. Yu, Z. Li, A numerical and experimental study of adhesively bonded aluminium single lap joints with an inner chamfer on the adherends, International Journal of Adhesion and Adhesives 28(1-2) (2008) 71-76.

[71] R. Haghani, M. Al-Emrani, R. Kliger, Stress Distribution in Adhesive Joints with Tapered Laminates — Effect of Tapering Length and Material Properties, Journal of Composite Materials 44(3) (2009) 287-302.

[72] R.D. Adams, J.A. Harris, The influence of local geometry on the strength of adhesive joints, International Journal of Adhesion and Adhesives 7(2) (1987) 69-80.

[73] X. Zhao, R. Adams, L. Da Silva, Single lap joints with rounded adherend corners: experimental results and strength prediction, Journal of Adhesion Science and Technology 25(8) (2011) 837-856.

[74] X. Zhao, R. Adams, L. Da Silva, Single lap joints with rounded adherend corners: Stress and strain analysis, Journal of Adhesion Science and Technology 25(8) (2011) 819-836.

[75] A.R. Rispler, L. Tong, G.P. Steven, M.R. Wisnom, Shape optimisation of adhesive fillets, International Journal of Adhesion and Adhesives 20(3) (2000) 221-231.

[76] L. Dorn, W. Liu, The stress state and failure properties of adhesive-bonded plastic/metal joints, International Journal of Adhesion and Adhesives 13(1) (1993) 21-31.

[77] A.M.G. Pinto, A. Magalhães, R.D.S.G. Campilho, M. De Moura, A. Baptista, Single-lap joints of similar and dissimilar adherends bonded with an acrylic adhesive, The Journal of Adhesion 85(6) (2009) 351-376.

[78] V. Ganesh, T. Choo, Modulus graded composite adherends for single-lap bonded joints, Journal of composite materials 36(14) (2002) 1757-1767.

[79] W.E. Guin, J. Wang, Theoretical model of adhesively bonded single lap joints with functionally graded adherends, Engineering Structures 124 (2016) 316-332.

[80] L.F.M. da Silva, M.J.C.Q. Lopes, Joint strength optimization by the mixed-adhesive technique, International Journal of Adhesion and Adhesives 29(5) (2009) 509-514.

[81] Ö. Öz, H. and Özer, An experimental investigation on the failure loads of the mono and bi-adhesive joints, Journal of Adhesion Science and Technology 31(19-20) (2017) 2251-2270.

[82] H. Ejaz, A. Mubashar, E. Uddin, Z. Ali, N. Arif, Influence of MWCNTs on strength properties of high viscous epoxy adhesive and fracture behavior of adhesively bonded joints, Theoretical and Applied Fracture Mechanics 120 (2022) 103412.

[83] P. Pyzik, A. Ziaja-Sujdak, J. Spytek, M. O'Donnell, I. Pelivanov, L. Ambrozinski, Detection of disbonds in adhesively bonded aluminum plates using laser-generated shear acoustic waves, Photoacoustics 21 (2021) 100226.

[84] J. Spytek, L. Ambrozinski, L. Pieczonka, Evaluation of disbonds in adhesively bonded multilayer plates through local wavenumber estimation, Journal of Sound and Vibration 520 (2022) 116624.

[85] M. Elhannani, K. Madani, Z. Chama, E. Legrand, S. Touzain, X. Feaugas, Influence of the presence of defects on the adhesive layer for the single-lap bonded joint—Part II: Probabilistic assessment of the critical state, Aerospace Science and Technology 63 (2017) 372-386.

[86] A.B. Pereira, A.B. de Morais, Strength of adhesively bonded stainless steel joints, International Journal of Adhesion and Adhesives 23(4) (2003) 315-322.

[87] A. Chadegani, R.C. Batra, Analysis of adhesive-bonded single-lap joint with an interfacial crack and a void, International Journal of Adhesion and Adhesives 31(6) (2011) 455-465.

[88] C.L. Chow, C.W. Woo, On flaw size and distribution in lap joints, Theoretical and Applied Fracture Mechanics 4(1) (1985) 75-82.

[89] B. Liang, A. Nagarajan, H. Ahmadian, S. Soghrati, Analyzing effects of surface roughness, voids, and particle–matrix interfacial bonding on the failure response of a heterogeneous adhesive, Computer Methods in Applied Mechanics and Engineering 346 (2019) 410-439.

[90] F. Ribeiro, R. Campilho, R. Carbas, L. Da Silva, Strength and damage growth in composite bonded joints with defects, Composites Part B: Engineering 100 (2016) 91-100.

[91] R. Larson, A. Bergan, F. Leone, O.G. Kravchenko, Influence of stochastic adhesive porosity and material variability on failure behavior of adhesively bonded composite sandwich joints, Composite Structures 306 (2023) 116608.

[92] V. Dumont, C. Badulescu, G. Stamoulis, J. Adrien, E. Maire, A. Lefèvre, D. Thévenet, On the influence of mechanical loadings on the porosities of structural epoxy adhesives joints by means of in-situ X-ray microtomography, International Journal of Adhesion and Adhesives 99 (2020) 102568.

[93] A. Sengab, R. Talreja, A numerical study of failure of an adhesive joint influenced by a void in the adhesive, Composite Structures 156 (2016) 165-170.

[94] C. Yildirim, H. Ulus, B. Beylergil, A. Al-Nadhari, S. Topal, M. Yildiz, Tailoring adherend surfaces for enhanced bonding in CF/PEKK composites: Comparative analysis of atmospheric plasma activation and conventional treatments, Composites Part A: Applied Science and Manufacturing 180 (2024) 108101.

[95] D.S. Kwon, S.H. Yoon, H.Y. Hwang, Effects of residual oils on the adhesion characteristics of metal-CFRP adhesive joints, Composite Structures 207 (2019) 240-254.

[96] Y. Li, S. Meng, Q. Gong, Y. Huang, J. Gan, M. Zhao, B. Liu, L. Liu, G. Zou, D. Zhuang, Experimental and Theoretical Investigation of Laser Pretreatment on Strengthening the Heterojunction between Carbon Fiber-Reinforced Plastic and Aluminum Alloy, ACS Applied Materials & Interfaces 11(24) (2019) 22005-22014.

[97] V. Reitz, D. Meinhard, S. Ruck, H. Riegel, V. Knoblauch, A comparison of IR- and UV-laser pretreatment to increase the bonding strength of adhesively joined aluminum/CFRP components, Composites Part A: Applied Science and Manufacturing 96 (2017) 18-27.

[98] M.R. Gude, S.G. Prolongo, A. Ureña, Adhesive bonding of carbon fibre/epoxy laminates: Correlation between surface and mechanical properties, Surface and Coatings Technology 207 (2012) 602-607.

[99] S.-M. Park, R. Roy, J.-H. Kweon, Y. Nam, Strength and failure modes of surface treated CFRP secondary bonded single-lap joints in static and fatigue tensile loading regimes, Composites Part A: Applied Science and Manufacturing 134 (2020) 105897.

[100] W. Zielecfei, P. Pawlus, R. Perłowski, A. Dzierwa, Surface topography effect on strength of lap adhesive joints after mechanical pre-treatment, Archives of Civil and Mechanical Engineering 13(2) (2013) 175-185.

[101] P. Blais, D.J. Carlsson, G.W. Csullog, D.M. Wiles, The chromic acid etching of polyolefin surfaces, and adhesive bonding, Journal of Colloid and Interface Science 47(3) (1974) 636-649.

[102] A. Nasreen, M.K. Bangash, K. Shaker, Y. Nawab, Effect of surface treatment on the performance of composite-composite and composite-metal adhesive joints, Polymer Composites 43(9) (2022) 6320-6331.

[103] S. Ebnesajjad, Handbook of adhesives and surface preparation: technology, applications and manufacturing, William Andrew2010.

[104] G. Yang, T. Yang, W. Yuan, Y. Du, The influence of surface treatment on the tensile properties of carbon fiber-reinforced epoxy composites-bonded joints, Composites Part B: Engineering 160 (2019) 446-456.

[105] Y. Boutar, S. Naïmi, S. Mezlini, R.J.C. Carbas, L.F.M. da Silva, M. Ben Sik Ali, Fatigue resistance of an aluminium one-component polyurethane adhesive joint for the automotive industry: Effect of surface roughness and adhesive thickness, International Journal of Adhesion and Adhesives 83 (2018) 143-152.

[106] J. Cui, S. Wang, S. Wang, S. Chen, G. Li, Strength and failure analysis of adhesive single-lap joints under shear loading: Effects of surface morphologies and overlap zone parameters, Journal of Manufacturing Processes 56 (2020) 238-247.

[107] S. Azari, P. M., J.K. and Spelt, Effect of Surface Roughness on the Performance of Adhesive Joints Under Static and Cyclic Loading, The Journal of Adhesion 86(7) (2010) 742-764.

[108] A. Baldan, Adhesion phenomena in bonded joints, International Journal of Adhesion and Adhesives 38 (2012) 95-116.

[109] J.D. Lim, Y.S.Y. Susan, R.M. Daniel, K.C. Leong, C.C. Wong, Surface roughness effect on copper–alumina adhesion, Microelectronics Reliability 53(9) (2013) 1548-1552.

[110] X. Zhan, Y. Li, C. Gao, H. Wang, Y. Yang, Effect of infrared laser surface treatment on the microstructure and properties of adhesively CFRP bonded joints, Optics & Laser Technology 106 (2018) 398-409.

[111] D. Zhang, Y. Huang, Influence of surface roughness and bondline thickness on the bonding performance of epoxy adhesive joints on mild steel substrates, Progress in Organic Coatings 153 (2021) 106135.

[112] D.-J. Kwon, J.-H. Kim, Y.-J. Kim, J.-J. Kim, S.-M. Park, I.-J. Kwon, P.-S. Shin, L.K. DeVries, J.-M. Park, Comparison of interfacial adhesion of hybrid materials of aluminum/carbon fiber reinforced epoxy composites with different surface roughness, Composites Part B: Engineering 170 (2019) 11-18.

[113] Walkerrubber, How do you make rubber adhesive? https://www.walker-rubber.co.uk/knowledge-hub/how-do-you-make-rubber-adhesive-368. (Accessed May 21 2025).

[114] V.M. Marinosci, W.J.B. Grouve, M.B. de Rooij, S. Wijskamp, R. Akkerman, Effect of grit-blasting on the fracture toughness of hybrid titanium-thermoplastic composite joints, International Journal of Adhesion and Adhesives 109 (2021) 102893.

[115] M.D. Shokrian, K. Shelesh-Nezhad, R. Najjar, The effects of Al surface treatment, adhesive thickness and microcapsule inclusion on the shear strength of bonded joints, International Journal of Adhesion and Adhesives 89 (2019) 139-147.

[116] A. Badami, M.L. Raffa, O. Klinkova, R. Rizzoni, T. Da Silva Botelho, G. Zambelis, Surface roughness influence on the behaviour of biocomposite adhesive joints, International Journal of Mechanical Sciences 283 (2024) 109624.

[117] D. Dachev, M. Kazilas, G. Alfano, S. Omairey, Towards Reliable Adhesive Bonding: A Comprehensive Review of Mechanisms, Defects, and Design Considerations, Materials, 2025.

[118] M. Tahani, S.A. Yousefsani, On thermomechanical stress analysis of adhesively bonded composite joints in presence of an interfacial void, Composite Structures 130 (2015) 116-123.

[119] R.B. Heslehurst, Observations in the structural response of adhesive bondline defects, International Journal of Adhesion and Adhesives 19(2) (1999) 133-154.

[120] J.Y. Goh, S. Georgiadis, A.C. Orifici, C.H. Wang, Effects of bondline flaws on the damage tolerance of composite scarf joints, Composites Part A: Applied Science and Manufacturing 55 (2013) 110-119.

[121] C.M. Fame, C. Wu, P. Feng, L.-h. Tam, Numerical investigations on the damage tolerance of adhesively bonded pultruded GFRP joints with adhesion defects, Composite Structures 301 (2022) 116223.

[122] S. Budhe, M.D. Banea, S. de Barros, L.F.M. da Silva, An updated review of adhesively bonded joints in composite materials, International Journal of Adhesion and Adhesives 72 (2017) 30-42.

[123] A. Mubashar, A.I. A., C.G. W., A.D. and Crocombe, A Method of Predicting the Stresses in Adhesive Joints after Cyclic Moisture Conditioning, The Journal of Adhesion 87(9) (2011) 926-950.

[124] J. Mohan, A. Ivanković, N. Murphy, Effect of prepreg storage humidity on the mixed-mode fracture toughness of a co-cured composite joint, Composites Part A: Applied Science and Manufacturing 45 (2013) 23-34.

[125] S. Budhe, A. Rodríguez-Bellido, J. Renart, J.A. Mayugo, J. Costa, Influence of pre-bond moisture in the adherents on the fracture toughness of bonded joints for composite repairs, International Journal of Adhesion and Adhesives 49 (2014) 80-89.

[126] M.D. Banea, d.S.L.F. M., R.D.S.G. and Campilho, Effect of temperature on the shear strength of aluminium single lap bonded joints for high temperature applications, Journal of Adhesion Science and Technology 28(14-15) (2014) 1367-1381.

[127] L.D.R. Grant, R.D. Adams, L.F.M. da Silva, Effect of the temperature on the strength of adhesively bonded single lap and T joints for the automotive industry, International Journal of Adhesion and Adhesives 29(5) (2009) 535-542.

[128] M.D. Banea, d.S.F.S. M., d.S.L.F. M., C.R.D.S. G., A.M.B. and de Pereira, Effects of Temperature and Loading Rate on the Mechanical Properties of a High Temperature Epoxy Adhesive, Journal of Adhesion Science and Technology 25(18) (2011) 2461-2474.

[129] L.D.C. Ramalho, R.D.S.G. Campilho, J. Belinha, L.F.M. da Silva, Static strength prediction of adhesive joints: A review, International Journal of Adhesion and Adhesives 96 (2020) 102451.

[130] K. Tserpes, B.-C. Alberto, C.P. Andrea, B.V. Carrillo, F. Ioannis, G. Wojciech, K. Marcin, S. Fabio, S. Moslem, S. Davor, B. Chiara, V. and Rajčić, A review on failure theories and simulation models for adhesive joints, The Journal of Adhesion 98(12) (2022) 1855-1915.

[131] O. Volkersen, Die Nietkraftverteilung in zugbeanspruchten Nietverbindungen mit Konstanten Laschenquerschnitten, Luftfahrtfor schung 15 (1938) 41-47.

[132] M. Goland, E. Reissner, The Stresses in Cemented Joints, Journal of Applied Mechanics 11(1) (2021) A17-A27.

[133] S.A. Yousefsani, M. Tahani, Analytical solutions for adhesively bonded composite single-lap joints under mechanical loadings using full layerwise theory, International Journal of Adhesion and Adhesives 43 (2013) 32-41.

[134] T. Wah, Stress Distribution in a Bonded Anisotropic Lap Joint, Journal of Engineering Materials and Technology 95(3) (1973) 174-181.

[135] C. Yang, S.-S. Pang, Stress-Strain Analysis of Single-Lap Composite Joints Under Tension, Journal of Engineering Materials and Technology 118(2) (1996) 247-255.

[136] F. Mortensen, O.T. Thomsen, Analysis of adhesive bonded joints: a unified approach, Composites Science and Technology 62(7) (2002) 1011-1031.

[137] J. Zhang, B.A. Bednarcyk, C. Collier, P. Yarrington, Y. Bansal, M.-J. Pindera, Analysis Tools for Adhesively Bonded Composite Joints, Part 2: Unified Analytical Theory, AIAA Journal 44(8) (2006) 1709-1719.

[138] S.A. Yousefsani, M. Tahani, E. Selahi, Analytical Solution of Stress Field in Adhesively Bonded Composite Single-Lap Joints Under Mechanical Loadings, International Journal of Engineering 27(3) (2014) 475-486.

[139] X.-F. Wu, Y. Zhao, Stress-function variational method for interfacial stress analysis of adhesively bonded joints, International Journal of Solids and Structures 50(25) (2013) 4305-4319.

[140] J. Wang, C. Zhang, Three-parameter, elastic foundation model for analysis of adhesively bonded joints, International Journal of Adhesion and Adhesives 29(5) (2009) 495-502.

[141] M.R. Ayatollahi, A. Akhavan-Safar, Failure load prediction of single lap adhesive joints based on a new linear elastic criterion, Theoretical and Applied Fracture Mechanics 80 (2015) 210-217.

[142] N. Razavi, M.R. Ayatollahi, H.R. Majidi, F. Berto, A strain-based criterion for failure load prediction of steel/CFRP double strap joints, Composite Structures 206 (2018) 116-123.

[143] J.A. García, A. Chiminelli, B. García, M. Lizaranzu, M.A. Jiménez, Characterization and material model definition of toughened adhesives for finite element analysis, International Journal of Adhesion and Adhesives 31(4) (2011) 182-192.

[144] Q. Zhang, X. Cheng, Y. Cheng, W. Li, R. Hu, Investigation of tensile behavior and influence factors of composite-to-metal 2D-scarf bonded joint, Engineering Structures 180 (2019) 284-294.

[145] S. Li, M.D. Thouless, A.M. Waas, J.A. Schroeder, P.D. Zavattieri, Use of a cohesive-zone model to analyze the fracture of a fiber-reinforced polymer–matrix composite, Composites Science and Technology 65(3) (2005) 537-549.

[146] D.C. O'Mahoney, K.B. Katnam, N.P. O'Dowd, C.T. McCarthy, T.M. Young, Taguchi analysis of bonded composite single-lap joints using a combined interface–

adhesive damage model, International Journal of Adhesion and Adhesives 40 (2013) 168-178.

[147] R.D.S.G. Campilho, M.D. Banea, J.A.B.P. Neto, L.F.M. da Silva, Modelling adhesive joints with cohesive zone models: effect of the cohesive law shape of the adhesive layer, International Journal of Adhesion and Adhesives 44 (2013) 48-56.

[148] S.L.S. Nunes, C.R.D.S. G., d.S.F.J. G., d.S.C.C.R. G., F.T.A. B., B.M. D., L.F.M. and da Silva, Comparative Failure Assessment of Single and Double Lap Joints with Varying Adhesive Systems, The Journal of Adhesion 92(7-9) (2016) 610-634.

[149] E.M. Moya-Sanz, I. Ivañez, S.K. Garcia-Castillo, Effect of the geometry in the strength of single-lap adhesive joints of composite laminates under uniaxial tensile load, International Journal of Adhesion and Adhesives 72 (2017) 23-29.

[150] J.P.J.R. Santos, D.S. Correia, E.A.S. Marques, R.J.C. Carbas, F. Gilbert, L.F.M. da Silva, Extended Finite Element Method (XFEM) Model for the Damage Mechanisms Present in Joints Bonded Using Adhesives Doped with Inorganic Fillers, Materials, 2023.

[151] T.F. Santos, R.D.S.G. Campilho, Numerical modelling of adhesively-bonded double-lap joints by the eXtended Finite Element Method, Finite Elements in Analysis and Design 133 (2017) 1-9.

[152] A. Mubashar, A.I. A., A.D. and Crocombe, Modelling Damage and Failure in Adhesive Joints Using A Combined XFEM-Cohesive Element Methodology, The Journal of Adhesion 90(8) (2014) 682-697.

[153] A. Cundall P, A Computer Model for Simulating Progressive, Large-scale Movement in Blocky Rock System, Proceedings of the International Symposium on Rock Mechanics 8 (1971) 129-136.

[154] A. Mohebkhah, A.A. Tasnimi, H.A. Moghadam, Nonlinear analysis of masonry-infilled steel frames with openings using discrete element method, Journal of Constructional Steel Research 64(12) (2008) 1463-1472.

[155] L. Maheo, F. Dau, D. André, J.L. Charles, I. Iordanoff, A promising way to model cracks in composite using Discrete Element Method, Composites Part B: Engineering 71 (2015) 193-202.

[156] M. Yu, B. Yang, Y. Chi, J. Xie, J. Ye, Experimental study and DEM modelling of bolted composite lap joints subjected to tension, Composites Part B: Engineering 190 (2020) 107951.

[157] M. Marigo, E.H. Stitt, Discrete Element Method (DEM) for Industrial Applications: Comments on Calibration and Validation for the Modelling of Cylindrical Pellets, KONA Powder and Particle Journal 32 (2015) 236-252.

[158] C.J. Coetzee, Review: Calibration of the discrete element method, Powder Technology 310 (2017) 104-142.

[159] Z. Gu, X. Ding, X. Hou, J. Ye, A genetic evolved machine learning approach for 3D DEM modelling of anisotropic materials with full consideration of particulate interactions, Composites Part B: Engineering 250 (2023) 110432.

[160] J. Shentu, B. Lin, A novel machine learning framework for efficient calibration of complex DEM model: A case study of a conglomerate sample, Engineering Fracture Mechanics 279 (2023) 109044.

[161] X.-e. Wang, A.Y. Kanani, Z. Gu, J. Yang, J. Ye, X. Hou, Estimating microscale DE parameters of brittle adhesive joints using genetic expression programming, International Journal of Adhesion and Adhesives 118 (2022) 103230.

[162] X.-e. Wang, A.Y. Kanani, K. Pang, J. Yang, J. Ye, X. Hou, A novel genetic expression programming assisted calibration strategy for discrete element models of composite joints with ductile adhesives, Thin-Walled Structures 180 (2022) 109985.

[163] X.-e. Wang, A. Yousefi Kanani, Z. Gu, J. Yang, J. Ye, X. Hou, Investigation on the transitional micromechanical response of hybrid composite adhesive joints by a novel adaptive DEM model, Theoretical and Applied Fracture Mechanics 124 (2023) 103760.

[164] C. Xue, M. Yu, B. Yang, T. Wang, M. Saafi, J. Ye, Experimental and numerical study on tensile properties of bolted GFRP joints at high and low temperatures, Composite Structures 293 (2022) 115743.

[165] A.Y. Kanani, X.-E. Wang, X. Hou, A.E. Rennie, J. Ye, Analysis of failure mechanisms of adhesive joints modified by a novel additive manufacturing-assisted method, Engineering Structures 277 (2023) 115428.

[166] X.-e. Wang, J. Yang, X. Huang, F. Wang, Y. Zhu, Voronoi-FDEM concept for modelling post-fracture response of progressively damaged structural glass, Engineering with Computers 38(4) (2022) 3025-3038.

[167] Z. Yang, Z. Zhu, Y. Xia, F. Yang, Y. Sun, H. Jiang, Modified cohesive zone model for soft adhesive layer considering rate dependence of intrinsic fracture energy, Engineering Fracture Mechanics 258 (2021) 108089.

[168] N. Razavi, F. Berto, M. Peron, J. Torgersen, Parametric study of adhesive joints with non-flat sinusoid interfaces, Theoretical and Applied Fracture Mechanics 93 (2018) 44-55.

[169] T. Dai, Y. Yang, H.-L. Dai, Z. Hu, Interfacial stress analysis of a CFRR-metal adhesively bonded joint with/without defect under hygrothermal environment, Applied Mathematical Modelling 67 (2019) 357-377.

[170] F. Stuparu, C.D. M., A.D. A., M. and Sandu, A Combined Cohesive Elements—XFEM Approach for Analyzing Crack Propagation in Bonded Joints, The Journal of Adhesion 92(7-9) (2016) 535-552.

[171] A.Y. Kanani, X.-E. Wang, X. Hou, A.E.W. Rennie, J. Ye, Analysis of failure mechanisms of adhesive joints modified by a novel additive manufacturing-assisted method, Engineering Structures 277 (2023) 115428.

[172] S. Mukhopadhyay, S.R. Hallett, A directed continuum damage mechanics method for modelling composite matrix cracks, Composites Science and Technology 176 (2019) 1-8.

[173] Y.C. Chung, Z.H. Yang, C.K. Lin, Modelling micro-crack initiation and propagation of crystal structures with microscopic defects under uni-axial tension by discrete element method, Powder Technology 315 (2017) 445-476.

[174] A.Y. Kanani, Development of Novel Multi-Material Adhesive Joints, Lancaster University (United Kingdom), England, 2021, p. 211.

[175] Y. Ismail, Y. Sheng, D. Yang, J. Ye, Discrete element modelling of unidirectional fibre-reinforced polymers under transverse tension, Composites Part B: Engineering 73 (2015) 118-125.

[176] I.C. Group, PFC documentation. https://docs.itascacg.com/pfc700/contents.html. (Accessed September 29 2025).

[177] K. Katnam, J. Stevenson, W. Stanley, M. Buggy, T. Young, Tensile strength of two-part epoxy paste adhesives: Influence of mixing technique and micro-void formation, International journal of adhesion and adhesives 31(7) (2011) 666-673.

[178] M. Ren, L. Wu, B. Yu, W. Wu, B. Liu, S. Xiao, Influence of adhesive types on bonding defects and adhesion performance of glass substrates, Progress in Organic Coatings 193 (2024) 108533.

[179] M. De Moura, R. Daniaud, A. Magalhães, Simulation of mechanical behaviour of composite bonded joints containing strip defects, International journal of adhesion and adhesives 26(6) (2006) 464-473.

[180] M. You, Z.-M. Yan, X.-L. Zheng, H.-Z. Yu, Z. Li, A numerical and experimental study of gap length on adhesively bonded aluminum double-lap joint, International Journal of Adhesion and Adhesives 27(8) (2007) 696-702.

[181] Y. Chu, L. Sun, B. Zhan, X. Yang, C. Zhang, W. Huang, Static and dynamic behavior of unbalanced bonded joints with adhesion defects in automotive structures, Composite Structures 226 (2019) 111234.

[182] M. Elhannani, K. Madani, E. Legrand, S. Touzain, X. Feaugas, Numerical analysis of the effect of the presence, number and shape of bonding defect on the shear stresses distribution in an adhesive layer for the single-lap bonded joint; Part 1, Aerospace Science and Technology 62 (2017) 122-135.

[183] L. Ponson, Mechanics and Physics of Fracture: Multiscale Modeling of the Failure Behavior of Solids, Springer Nature2023.

[184] E.E. Gdoutos, Fracture mechanics: an introduction, Springer Nature2020.

[185] S.K. Maiti, Fracture mechanics, Cambridge University Press2015.

[186] D. Salimi-Majd, F. Shahabi, B. Mohammadi, Effective local stress intensity factor criterion for prediction of crack growth trajectory under mixed mode fracture conditions, Theoretical and Applied Fracture Mechanics 85 (2016) 207-216.